Three dimensional MEMS supercapacitors

A Thesis

Submitted to the Department of Physics

at University of Oslo

in partial fulfillment of the requirements

for the degree of Doctor of

Science in Physics

By

Wei Sun

B.E., Xi'an Jiaotong University, 2003

M.E., Xi'an Jiaotong University, 2006

October 2010

Series of dissertations submitted to the
Faculty of Mathematics and Natural Sciences, University of Oslo
No. 1042

ISSN 1501-7710

Cover: Inger Sandved Anfinsen.
Printed in Norway: AIT Oslo AS.

Produced in co-operation with Unipub.
The thesis is produced by Unipub merely in connection with the
thesis defence. Kindly direct all inquiries regarding the thesis to the copyright
holder or the unit which grants the doctorate.

Contents

Appendix 4 Symmetric Redox Supercapacitor Based on microfabrication with Three Dimensional Polypyrrole Electrodes

Abstract

The overall objective of this research is to achieve compact supercapacitors with high capacitance, large power density, and long cycle life for using as micropower sources to drive low power devices and sensors. The main shortcoming of supercapacitors as a power source is that its energy density typically is about 1/10 of that of batteries. To achieve compact supercapacitors of large energy density, supercapacitors must be developed with high capacitance and power density which are mainly depended on the effective surface area of the electrodes of the supercapacitors. Many studies have been done to increase the effective surface area by modifying the electrode materials, however, much less investigations are focus on machining the electrodes. In my thesis work, micro- and nano-technologies are applied as technology approaches for machining the electrodes with three dimensional (3D) microstructures. More specific, Micro-electro-mechanical system (MEMS) fabrication process flow, which integrates the key process such as LIGA-like (German acronym for Lithographie, Galvanoformung, Abformung, which mean Lithography, Electroplating and Molding) technology or DRIE (deep reactive ion etching), has been developed to enable innovative designs of 3D MEMS supercapacitors which own the electrodes of significantly increased geometric area. Two types of 3D MEMS supercapcitors, based on LIGA-like and DRIE technology respectively, were designed and successfully created.

The LIGA-like based 3D MEMS supercapacitor is with an interdigital 3D structure, and consists of silicon substrate, two electroplated nickel current collectors, two PPy (polypyrrole) electrodes, and solid state electrolyte. The fabrication process flow developed includes the flowing key processes, SU-8 lithography, nickel electroplating, PPy polymerization and solid state electrolyte coating. Electrochemical tests showed that the single electrode of the supercapacitor has the specific capacitance of 0.058 Fcm^{-2} and the specific power of 0.58 $mWcm^{-2}$ at 20mVs^{-1} scan rate. The 3D MEMS supercapacitor fabricated in this project has the specific capacitance and the specific power of 0.029 Fcm^{-2} and 2.2 $mWcm^{-2}$ respectively at a relative large discharge rate of 5 $mAcm^{-2}$. It is also found

that the supercapacitors have the performance of broad frequency range up to 300Hz.

For DRIE based 3D MEMS supercapacitor, the innovative designs were developed based on silicon micromachining process flow which includes the key processes such as thermal oxidation, RF sputtering, wet etching, DRIE, electroless plating and PPy polymerization. The optimized PPy electrode doping with TOS^- performed ideal supercapacitor properties in NaCl electrolyte. The single PPy electrode of the 3D MEMS supercapacitors can provide 0.128 Fcm^{-2} specific capacitance and 1.28 $mWcm^{-2}$ specific power at 20 mVs^{-1} scan rate. The specific capacitance of the 3D MEMS supercapacitors equals 0.056 Fcm^{-2}, and the specific power at 20 mVs^{-1} scan rate equals 0.56 $mWcm^{-2}$.

In addition, novel supercapacitors based on wafer level process are designed for flexible integration in applications such as high temperature electronics and hybrid power system for electric vehicles. Experimental work on TiO_2 anodic oxidation, which enables the fabrication of the one of these designs, has been carried out. Dense TiO_2 nanoholes with diameters ranged from about 90 to 270 nm were obtained in 0.05 wt% HF aqueous solutions with two-step anodic oxidation method.

Comparing to the published specific capacitance (about 2 $mFcm^{-2}$) for microsupercapacitors [33], I have achieved much larger specific capacitance (typically 0.029 to 0.056 Fcm^{-2}) for 3D MEMS supercapacitors. The above results have been presented in 3 international conferences. Total 4 journal articles have been published, and one has been submitted. The article in the Journal of Power Source (appendix 3) has been cited 9 times after published in April 2009, and the article in Microelectronic Engineering (appendix 1) has been cited 4 times after published in December 2008, which shows the originality and the importance of the work.

Keywords: MEMS, supercapacitors, three dimensional, specific capacitance, specific power.

Chapter 1 Introduction

In this chapter, I will introduce the background of supercapacitors, the MEMS (Micro-Electro-Mechanical System) energy storage devices, and the research objectives of this thesis.

1.1 Supercapacitors as power sources

For energy storage devices, energy density and power density are the two key parameters for characterizing the performance of the devices. The energy density defines the amount of energy that can be stored in a given volume or weight of the material. The power density defines the total energy per second which can be stored into the device. The higher the power density is, the faster the loading and unloading the amount of energy will be. The ideal storage device should be characterized by both high energy density and high power density. This is unfortunately not the case for most of the energy storage devices. Batteries normally have high energy density, but poor power density. In contrary, capacitors have low power density, but high power density. However, supercapacitors of today's innovation could have high power density and significant increased high energy density. Fig. 1.1 shows the Ragnone plot of various energy storage devices [1].

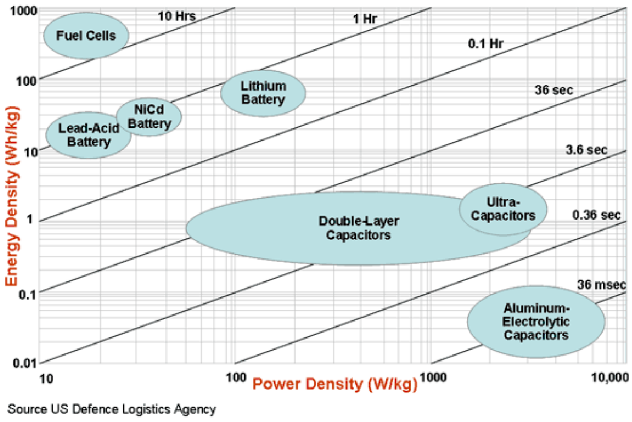

Fig. 1.1 Ragnone plot of various energy storage devices [1].

In comparison with batteries, supercapacitors have the following advantages, high power density, very shot charge and discharge time, more than 500,000 times cycle life, and high operating temperature. Table 1 presents the comparison of supercapacitors and

lithium-ion batteries[2].

Applications of the supercapacitors cover from electronic circuits to large power systems. Lux Research [3] reported that consumer electronics and large energy storage applications will power significant growth through 2014 for supercapacitors, and that the overall market is expected to expand from $208 million 2008, to an $877 million market in 2014. One main application of supercapacitors is to build hybrid power system consisting of supercapacitors and batteries for improving the current handling of batteries. In the hybrid power system, supercapacitors can enhance battery efficiency and cycle life. For electrical vehicles, the hybrid power system can meet the challenges such as long interzone driving and fast acceleration. The supercapacitor will also find a ready market for portable fuel cells to enhance peak-load performance. Because of its ability of rapidly charging and discharging, large supercapacitors can also be used for energy recovery in braking vehicles and seaport cranes.

Table 1. Comparison of some important characteristics of state-of-the-art supercapacitors and lithium ion batteries [2].

Characteristic	State of the Art Lithium Ion Battery	Electrochemical Capacitor
*Charge time	~3-5 minutes	~1 second
*Discharge Time	~3-5 minutes	~1 second
Cycle life	<5,000 @ 1C rate	>500,000
Specific Energy (Wh/kg)	70-100	5
Specific power (kW/kg)	**0.5 -1	5-10
Cycle efficiency (%)	<50% to >90%	<75 to >95%
Cost/Wh	$1-2/Wh	$10-20/Wh
Cost/kW	$75-150/kW	$25-50/kW

** Time for discharge and charge of the useable total energy stored in the devices.*
*** Power capability of the battery for short duration partial discharge at 90% efficiency.*

1.2 Why MEMS supercapacitors?

In consuming electronics supercapacitors are widely applied as backup power sources for memories, microcomputers, system boards, and clocks. Supercapacitors can supply the critical power in case of power outages due to disconnection or turn-off of the primary source, contact problems due to vibration or shocks, or a drop of the system voltage due to switching-in of other heavy loads. Another application of supercapacitors is in energy

harvesting systems, where the supercapacitors is used for collecting the energy from the harvesters which harvest energy from ambient environment sources, such as solar [4], thermal [5], and mechanical vibrations [6,7]. Fig. 1.2 lists power outputs of different energy harvesters [8]. It can be found that the output power densities of almost all the energy harvesters are less than 1000 μWcm^{-3} except that of solar energy harvester (outside situation). The power density of common vibration sources is less than 100 μWcm^{-3} which is too small to match the demands for most of consuming electronics as shown in Fig. 1.3.

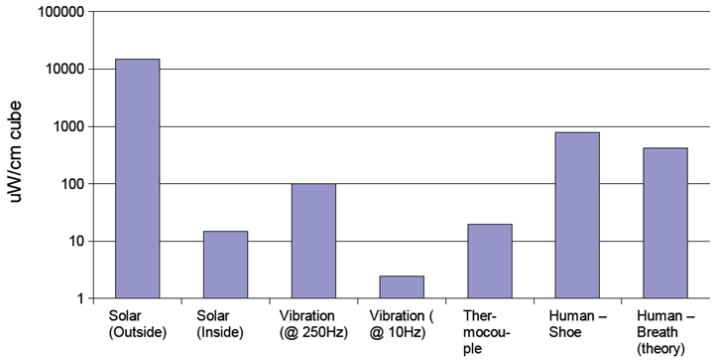

Fig. 1.2 Comparison of power sources [8].

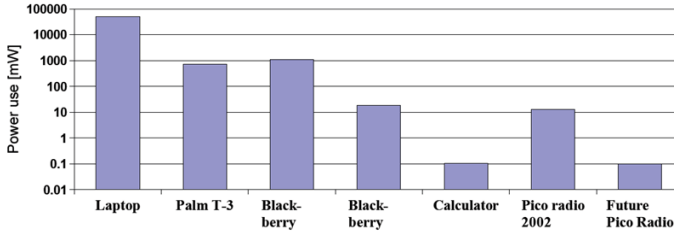

Fig. 1.3 Power usages of consuming electronics [8]

In general applications, the power demand from power sources is intermittent, while the energy harvesters work continuously. Therefore, in a harvesting system an energy storage device is needed to store the scavenged energy and manage the system for high power application. Due to their fast charging/discharging ability, high power density and long cycle lifetime, supercapacitors are widely used in the energy harvesting systems. To list a few, Fig. 1.4(a) [9] depicts the integration of a RF energy harvester with a supercapacitor to create a perpetual, battery-free power source for the wireless sensors commonly used in security, environmental and condition monitoring systems. Fig. 1.4(b) [9] presents the integration of a vibration energy harvester together with a supercapacitor,

which allows wireless sensor system manufacturers to design battery-free condition monitoring systems which collect and report data on machinery for improved asset management.

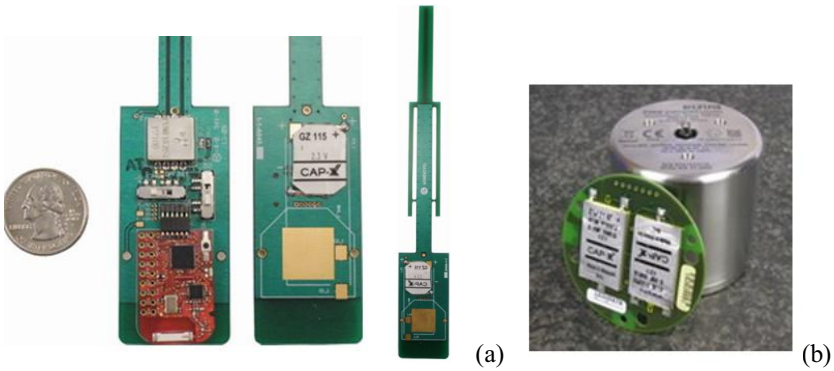

Fig. 1.4 Hybrid supercapacitor/ energy harvester systems [9], (a) Powercast RF energy harvester, (b) vibration energy harvester.

Fig. 1.5 shows some commercial available supercapacitors [10]. They are commonly three types classified by packaging method: button supercapacitors, spiral wound supercapacitors and stacked multilayer supercapacitors [11,12]. All the commercial products are big and difficult for flexible integration in above described applications. Especially, miniaturizations of systems require compact capacitors of high specific capacitance and miniaturized power sources of high energy and power density. Integration of supercapacitors with the devices in micro scale and flexible system integration are also the developing targets. Therefore, miniaturization of supercapacitors by MEMS technology is required.

Fig. 1.5 Commercial products of supercapacitors [10].

1.3 State-of-art of MEMS energy storage devices

In the field of MEMS energy storage, lithium ion thin film batteries have been extensively investigated. A typical structure of lithium ion thin film batteries is shown in Fig. 1.6 [13]. Because the thicknesses of the thin films are always at the level of micrometers or few tens of micrometers, relatively large footprints of at least a few cm^2 are required in order to provide reasonable capacity and energy. Generally, the performance of batteries depends strongly on the cathode materials, $LiCoO_2$ [14,15], $LiMn_2O_4$ [16,17] and other metal oxide or sulfide or oxysulfide [18,19].

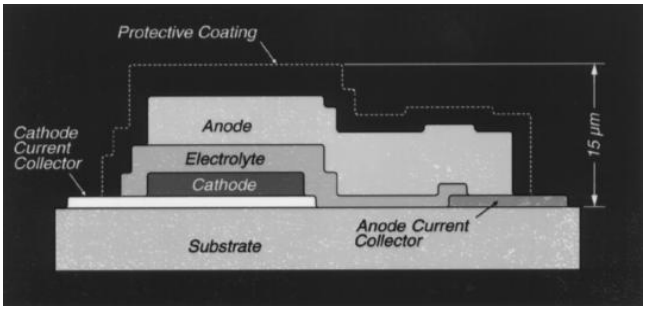

Fig. 1.6 Schematic cross-section of MEMS Li-ion battery [13].

To enhance the capacity of the thin film batteries, 3D architectures, such as vertical "posts" [20,21], graphite mesh [22] and micro-holes in silicon wafer [23,24,25], were proposed. Among these, a 3D MCP (Microchannel plates)-based micro battery (shown in Fig. 1.7) was developed by Tel Aviv University [25], which comprises a nickel cathode current collector, a nominally MoS_2 cathode, a lithiated graphite anode that also serves as anode current collector, and Hybrid Polymer Electrolyte (HPE). The MCP substrate was machined by DRIE (deep reactive ion etching) with through-holes to fabricate the perforated silicon plate which has diameter of 13 mm and thickness of 0.5 mm, and 50 um diameter microchannels separated by 10 μm walls. The MCP substrate provides more than an order of magnitude increase of geometrical area per given substrate footprint. The capacity of the 3D MCP based micro batter is 20 to 30 times higher than that of a planar 2D thin-film batter of the same footprint.

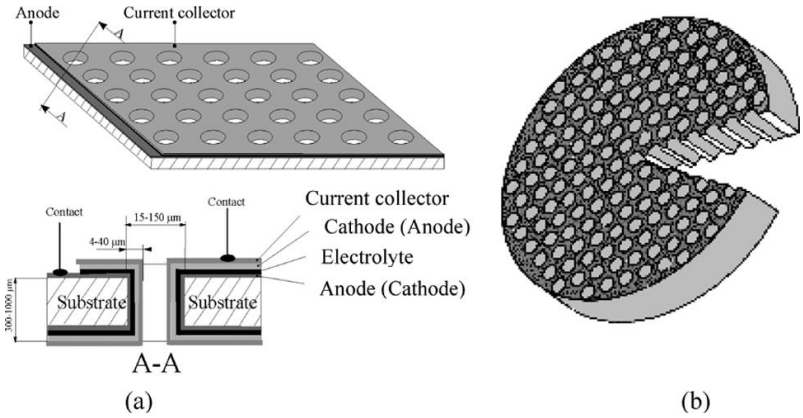

Fig. 1.7 (a), Schematic structure of a 3-D thin-film battery on a perforated silicon substrate. (b) Schematic structure of an MCP substrate.[25]

MEMS supercapacitors as energy storage devices were less investigated in the past. According to the working principles shown in Fig. 1.8, supercapacitors can be classified into double-layer capacitor (EDLC) and electrochemical pseudo capacitor (EPC). For EDLC, the capacitance comes from physical polarizing process. Typically, carbon based materials, such as activated carbon [26] or carbon nanotubes [27,28], and materials with large surface area [29] are used for the electrode. For EPC, the capacitance is produced by electrochemical reaction. The electrode materials are commonly metal oxides and conducting polymers, for instance, RuO_2 [30] and PPy [31,32].

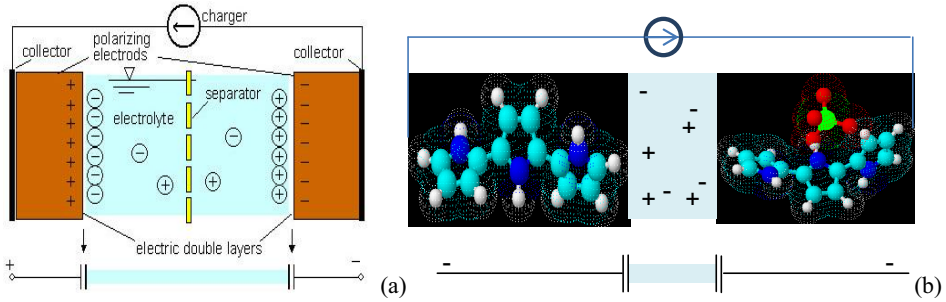

Fig. 1.8 Working principles of supercapacitors, (a) EDLC, (b) EPC.

Joo-Hwan Sung et al. [33,34] have fabricated all-solid-state electrochemical micro supercapacitors by using photolithography, electrochemical polymerization and solution casting techniques. Their process flow is briefly presented in Fig. 1.9. The gold microelectrode arrays as current collectors are fabricated by ultraviolet photolithography

and a wet-etching method. Polypyrrole (PPy) as electro active material are potentiostatically synthesized on these microelectrodes. Only about 2 $mFcm^{-2}$ specific capacitance was achieved from their work.

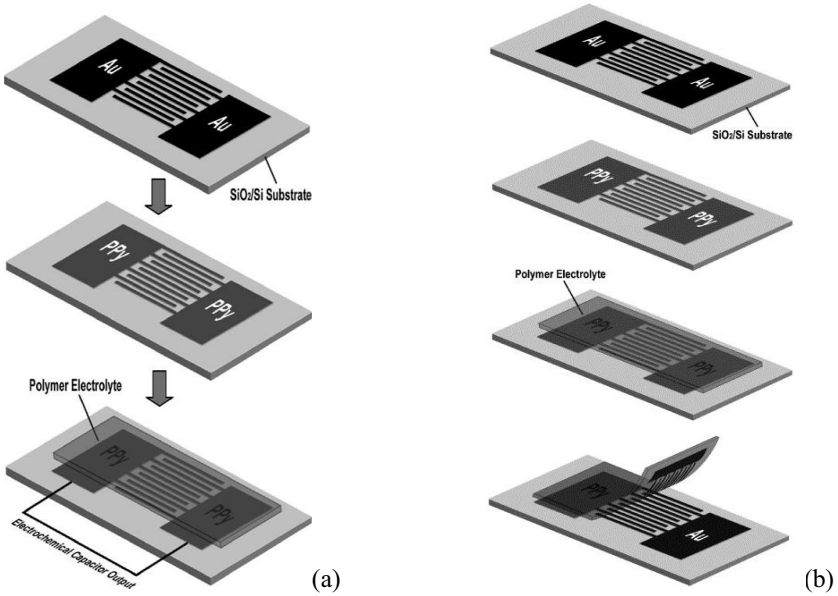

Fig. 1.9 Fabrication procedures for (a) microcapacitor on silicon substrate [33], and (b) flexible micro supercapacitors [34].

Y. Q. Jiang fabricated a double layer supercapacitor (shown in Fig. 1.10) utilizing vertically aligned carbon nanotube forests with 80 μm height on silicon wafer [35], which has capacitance density of 428 μFcm^{-2} and power density of 0.28 $mWcm^{-2}$. Y. Xie reported a NiO electrode for supercapacitor as shown in Fig. 1.11(a), which was conformal deposited on the inside walls of anodic oxidized TiO_2 nanotubes [36]. The electrochemical tests showed that specific capacitance of 40-70 $mFcm^{-2}$ at different testing conditions was achieved from the electrode, while the shape of CV (cyclic voltammetry) curve for the electrode is not the ideal rectangle-like [37] (see Fig. 1.11(b)). S. B. Lee and G. W. Rubloff fabricated a metal-insulator-metal electrostatic capacitor as shown in Fig. 1.12 [38]. Atomic layer deposition (ALD) [39] was used for the conformal deposition of dielectric layer Al_2O_3 of few nanometers thickness. They achieved the specific capacitance about 100 μFcm^{-2}. The supercapacitor is electrolyte free so that it can operate at high temperature.

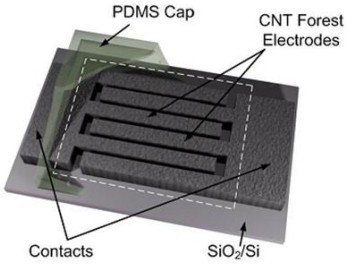

Fig. 1.10 Micro supercapacitor with 3D carbon nanotubes electrodes [35].

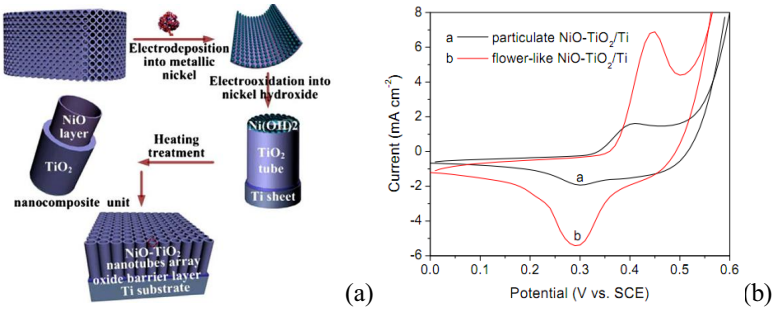

Fig. 1.11 (a) Supercapacitor electrode- NiO/TiO_2 nanocomposite, (b) CV curves.[36]

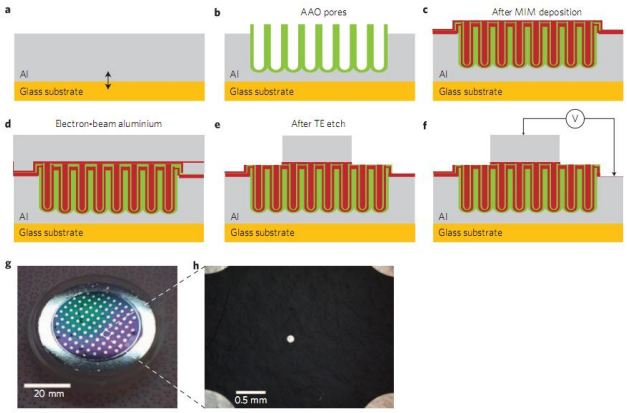

Fig. 1.12 Fabrication process flow for electrostatic supercapacitors [38].

Generally, the capacitance or energy density of EPC is larger than that of EDLC. Combining EPC with 3D microstructure, the research will bring the field beyond the state-of-the-art to create 3D MEMS supercapacitors with high energy density and power density.

1.4 Research objective and main work

The overall objective of this research is to achieve 3D MEMS supercapacitors with

high capacitance and power density. The main works are detailed as the following,

1) Design of MEMS supercapacitors.
2) Material development for MEMS supercapacitors
3) Microfabrication processes development, such as RF (radio frequency) sputtering, electroless plating, electroplating, wet etch, DRIE, and electrochemical polymerization.
4) Design optimization in terms of supercapacitor system configuration (electrolyte, electrodes).
5) Process integration and device fabrication
6) Characterization.

1.5 Thesis organization

The thesis is organized in 6 chapters. The project background is presented in chapter 1. In chapter 2, theory and principles for design the high performance supercapacitors are described. The fabrication and characterization of the LIGA-like 3D MEMS supercapacitor are discussed in chapter 3. In chapter 4, the design, fabrication, optimizations and tests of the DRIE based 3D MEMS supercapacitors are represented. Several novel approaches for manufacturing supercapacitors based on wafer level process are given in chapter 5. Finally, the conclusions and outlook of this research are summarized in chapter 6.

Chapter 2 Design of MEMS supercapacitors

In this chapter, design principle for MEMS supercapacitors of high performance will be discussed and developed. 3D MEMS structure will be the design approach to realize large effective surface area per unit device footprint. Configurations and material systems for different 3D MEMS supercapacitors will be designed based on LIGA-like and DRIE MEMS technology respectively.

2.1 Requirements for achieving high performance supercapacitors

A MEMS supercapacitor consists of a substrate, two current collectors, an anode, a cathode, and electrolyte. As mentioned in chapter 1, supercapacitors can be classified into EDLC and EPC by charge storage mechanisms. The energy E stored in a supercapacitor can be calculated as Eq. 2.1.

$$E = \frac{1}{2} C V^2 \tag{2.1}$$

where C is the capacitance, and V is the operating voltage. By increasing C and V, the energy stored in the supercapacitor will increase.

For EDLC, for a given electrolyte the capacitance C depends mainly on the effective surface area of the electrodes A, which is given as Eq. 2.2.

$$C = \frac{\varepsilon_r \varepsilon_0 A}{d} \tag{2.2}$$

where ε_r is the dielectric constant of the electrolyte, ε_0 is the dielectric constant of vacuum, and d is the effective thickness of double layer.

For EPC, the capacitance depends on both the preparation conditions and the effective surface area A.

The operating voltage V of supercapacitors depends on both material of the electrodes and electrolyte.

The power P delivered from a supercapacitor can be calculated by Eq. 2.3,

$$P = E/t - I^2R \tag{2.3}$$

where t is the discharging time, I is the discharge current, and R is the equivalent series resistance of the supercapacitor. To improve the power property, the supercapacitors must have small equivalent series resistance to be discharge fast. The equivalent series resistance depends on the current collectors, the electrolyte and the material of electrodes.

As a summary of above basic discussion, to obtain supercapacitors of high energy and power density, the electrodes must have large surface area and small resistance; the current collectors must have good conductivity; electrolytes must be developed for achieving high ionic conductivity. Among these, the increase of the effective surface area of electrodes becomes the first priority for the design of supercapacitors.

2.2 Design of 3D MEMS supercapacitors

In MEMS technology, silicon and polymer are mostly used as structure materials. The thickness of the structure layer reaches several hundred micrometers. To achieve the large effective surface area, 3D microstructure downward to wafer of high aspect ratio for the electrodes is certainly the best design approach. Methods to fabricate 3D structures in MEMS technology depend on the structure material. Ultraviolet LIGA (LIGA-like) process is utilized in polymer based MEMS technology, which fabricates 3D structures in thick resist polymer layers.

Fig. 2.1(a) shows a 517 μm tall copper coplanar waveguide fabricated by LIGA-like technology [40]. Fig. 2.1(b) shows a 3D microbatteries fabricated by combining LIGA-like and high temperature pyrolysis technology [41,42]. DRIE of silicon is employed for silicon based MEMS technology, where 3D microstructure is machined in silicon wafer by DRIE. Fig. 2.1(c) presents a micro 3D structure of polysilicon fabricated by DRIE [43].

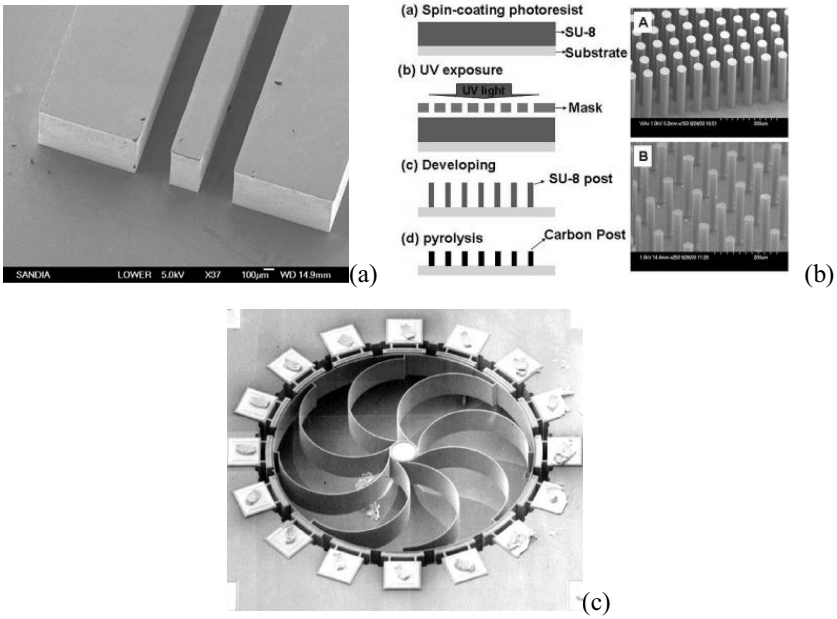

Fig. 2.1 (a), A 517 µm tall copper coplanar waveguide fabricated by LIGA technology [40], (b), A schematic drawing of carbon-MEMS fabrication process and typical SEM (A) before pyrolysis and (B) after pyrolysis [42], (c), SEM view of an 80-µm-thick 1.1-mm diameter HARPSS polysilicon ring gyroscope fabricated by DRIE [43].

2.2.1 3D MEMS supercapacitors design based on LIGA-like technology

LIGA-like technology utilizes an inexpensive ultraviolet light source to expose a polymer photoresist, typically SU-8, wet chemical etching process will be carried out subsequently. By process optimization, 3D polymer micorstructure can have the aspect ratio of 100:1.

In this design, silicon wafer will be used as the process substrate. Thick negative photoresist SU-8 will be used as structuring material and fabricated into comb-like structures as the mold for nickel electroforming. The electroformed nickel with 3D structures will be the current collectors for the deposition of PPy electrodes, which will be polymerized by electrochemical method. Solid state electrolyte will be used in such configuration of 3D MEMS supercapacitors. The design of the 3D MEMS supercapacitors

is schematically shown in Fig 2.2. On a silicon substrate, the 3D MEMS supercapacitor consists of two nickel current collectors with interdigital structure which are coated with polypyrrole (PPy) film, and a solid state electrolyte filling-in all the interdigital space. The interdigital anode and cathode provide short path for ions transfer in solid state electrolyte.

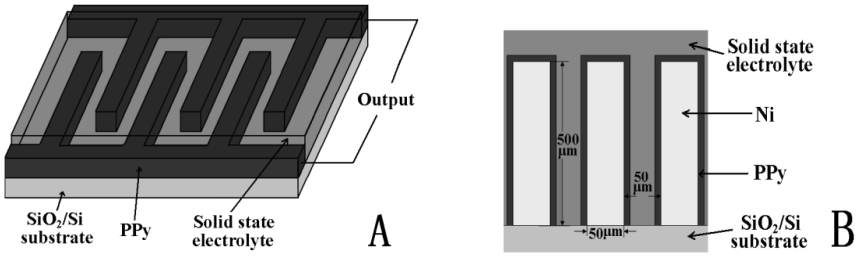

Fig. 2.2. (A) Schematic drawing of 3D MEMS supercapacitor; (B) Cross-section.

2.2.2 3D MEMS supercapacitors design based on DRIE technology

DRIE is a highly anisotropic etching process used to create deep, steep-sided holes and trenches in silicon wafers, with aspect ratios of 20:1 or more.

In this design, silicon wafer is used both as the process substrate and structuring material. The 3D microstructure is machined as the structure of the MEMS supercapacitors. Metallic layer will be deposited on the 3D structure for forming current collectors. Then continuous PPy films will be polymerized on anode and cathode current collectors respectively. The design of the 3D MEMS supercapacitor is shown in Fig.2.3. The supercapacitor has 3D “through-wafer structure”. The 3D “through-wafer structure” consists of two disconnected periodic beams coated with PPy film, which serve as anodes and cathodes. For the silicon substrate with thickness of 525 μm, the 3D “through-wafer structure” with the width of 100 μm will provide an effective surface area 10 times more than its planar structure.

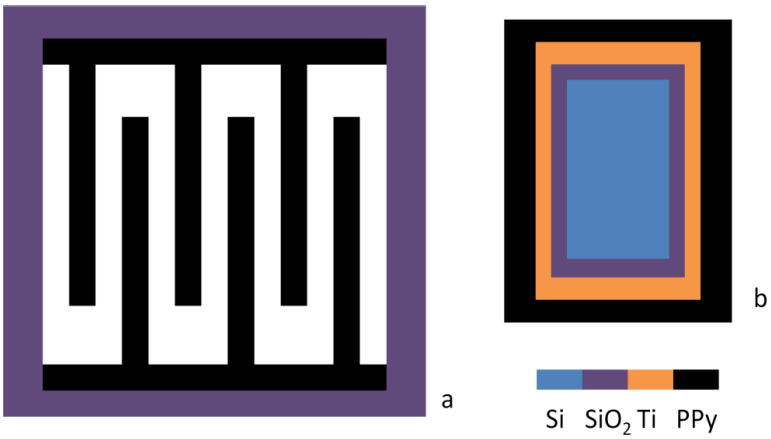

Fig.2.3 (a) Schematic drawing of designed supercapacitor, (b) cross-section.

2.3 The current collectors of the 3D MEMS supercapacitors

The current collectors of the 3D MEMS supercapacitors determine the series resistance and the specific capacitance of the supercapacitors. Without reducing the effective surface area, the current collectors have to perfectly contact with the 3D micro structures.

For the designed 3D MEMS supercapacitors based on LIGA-like technology, the electroforming can be employed for realize the conformal 3D current collectors. Electroforming is a metal forming process through the electroplating. The metal part is produced by plating a metal skin onto a base form, known as a mandrel, which is removed after plating. Nickel electroforming [44] is the most mature technology.

For the designed 3D MEMS supercapacitors based on DRIE technology, electroless plating [45] and RF sputtering [46] can be used to deposit the metallic layers onto all the effective surface of the 3D microstructures. In the electroless plating process, the driving force for the reduction of metal ions is supplied by a chemical reducing agent in solution. This driving potential is essentially constant at all points of the surface of the component, provided the agitation is sufficient to ensure a uniform concentration of metal ions and reducing agents. Electroless deposits are therefore conformal and very uniform in thickness. This process offers distinct advantages when plating irregularly shaped objects, holes,

recesses, internal surfaces, valves or threaded parts. Generally, it is not easy to obtained continuous coating on high aspect ratio structures by RF sputtering. In this design, I use two-step RF sputtering with rotation of the 3D microstructures to deposit metal continuously even onto the sidewalls.

2.4 The electrodes of the 3D MEMS supercapacitors

Conducting polymer Polypyrrole (PPy) is chosen as the electrode material of supercapacitors due to its cheap price, high conductivity, and good electrochemical performance. As shown in Fig. 2.4(a), the molecular structure of pyrrole (Py) monomer is a ring containing four carbon atoms and one nitrogen atom. When the Py monomers connect to each other and form a PPy segment, as can be seen in Fig. 2.4(b), the "electron cloud" of each monomer will overlap and form a conjugated π bond. The π electron of intrinsic PPy is not able to move freely in the whole polymer chain because the energy gap between the bonding orbital and antibonding orbital of the π electrons is about 1.5 eV. However, because PPy always exists with doping state, the conductivity of PPy is generally large as conductors, such as 100 scm^{-1} [47].It is well known the conductivity depends on the concentration of carrier and the mobility of carrier. In polymer, the mobility of carrier is much less than that in inorganic semiconductors because large energy is required to remove carrier between two polymer chains. So, the conductivity improvement of PPy depends mainly on the increasing concentration of carriers.

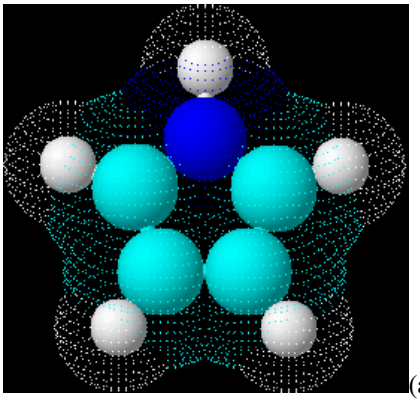
(a)
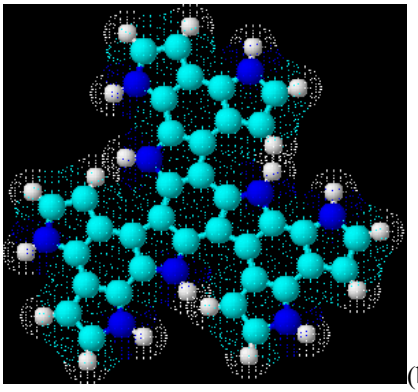
(b)

Fig. 2.4 (a), Structure of Py monomer, (b), structure of PPy segment.

According to the band theory, reducing the electron in valence band (p type doping) and injecting electron to conducting band (n type doping) will increase the conductivity of semiconductors. For PPy with doping state, polaron and bipolaron are regarded as the carriers [48]. The polymerization of PPy is accompanied with p type doping, so that the doping states of PPy can be easily changed by chemical and electrochemical polymerization. For MEMS supercapacitors, electrochemical method will be applied for PPy polymerization. The polymerization mechanism [49,50] can be explained in Fig. 2.5. At first, the Py monomer will lose one electron and be oxidized as a cation radical. Then, the polymerization of cation radicals will occur accompanying with p type doping, which is actually further oxidation process of intrinsic PPy. To control the doping level, polymerization parameters such as pH value has been optimized. As an example, Eq. 2.4 and Eq. 2.5 express the reaction on the working electrode and counter electrode if the doping ratio of 1/3 is achieved, i.e. a structure contain three Py monomers must contain one doping ion.

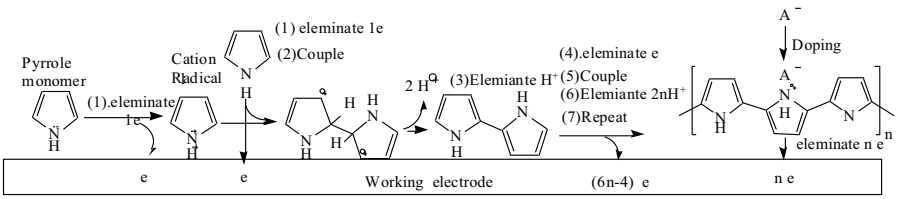

Fig. 2.5 Electrochemical polymerization mechanism of PPy.

$$3n\ Py + n\ A^- - (7n-2)\ e \xrightarrow[\text{On working electrode}]{\text{Electropolymerization}} [(Py)_3^+(A^-)]_n + (6n-2)\ H^+ \quad (2.4)$$

$$(7n-2)\ H^+ + (7n-2)\ e \xrightarrow[\text{On counter electrode}]{\text{Eleminate } H_2} \frac{7n-2}{2} H_2\uparrow \quad (2.5)$$

2.5 Electrolyte in 3D MEMS supercapacitors

The electrolyte for a supercapacitor can be aqueous or organic solutions. The aqueous electrolyte offers low internal resistance but limits the operating voltage to 1 V. In contrast, the organic electrolyte allows 2.5 V of working voltage, but the internal resistance is higher. Generally, the potential window of a PPy electrode will not be larger than 1 V. Therefore, the cheaper aqueous electrolytes with proper ions [51] are selected to be used together with PPy electrodes for supercapacitors. Solid state electrolyte [52,53] is another choice because of its advantages of safety and easy package, although the ions diffusion in solid state

electrolyte cannot be as fast as in liquid electrolyte.

2.6 Electrochemical test methods

For characterizing the electrochemical properties of a supercapacitor, cyclic voltammetry (CV) [54], electrochemical impedance spectroscopy (EIS) [55] and gavanostatical charge/discharge (GCD) [56] are commonly used. All the electrochemical tests will be performed on electrochemical workstation (Solartron 1260) with three-electrode system and two-electrode system. The software CorrWare (for CV and GCD) and Zplot (for EIS) will be used to setup experimental conditions and capture the response data. The hardware connection is shown in Fig. 2.6 [57]. The GPIB communication bus is designed to allow several instruments to be controlled by a computer over a single cable. The current flowing (I) between the working electrode (WE) and counter electrode (CE), as well as the potential (V) between WE and a reference electrode (RE) are monitored.

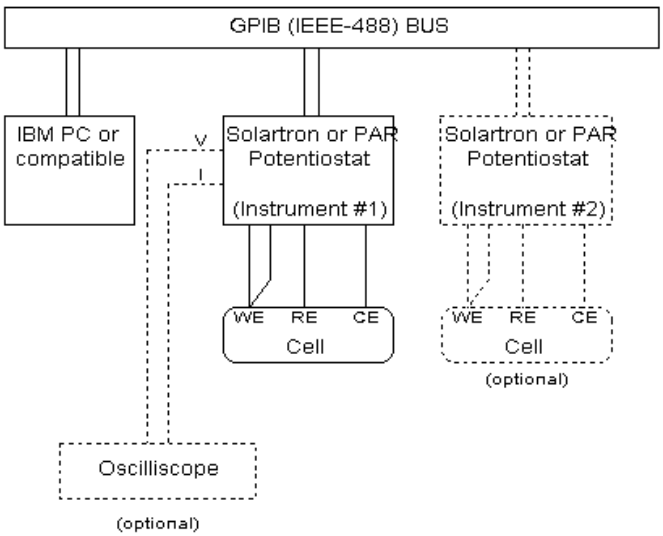

Fig. 2.6 Hardware connection of electrochemical workstation [57].

CV is a type of potentiodynamic electrochemical measurements. The potential of working electrode is ramped linearly versus time like linear sweep voltammetry. CV takes the experiment a step further than linear sweep voltammetry which ends when it reaches a set potential. When CV reaches a set potential, the working electrode's potential ramp is

inverted (Fig. 2.7. (a)). This inversion can happen multiple times during a single experiment. The current at the working electrode is plotted versus the applied voltage to give the CV trace, as shown in Fig. 2.7 (b). The positive current peak and negative current peak imply the oxidation and reduction processes of working electrode respectively. For an ideal supercapacitor, the shape of CV curve should be a rectangle [58]. Different with the potential sweep of CV, GCD is a current linearly sweep methods as shown in Fig. 2.8 (a). The relationship of potential and time imply the reaction of working electrode, the slope of the linear part of discharge curve represents the value of the capacitance of a supercapacitor or an electrode of a supercapacitor, which can be seen in Fig. 2.8 (b).

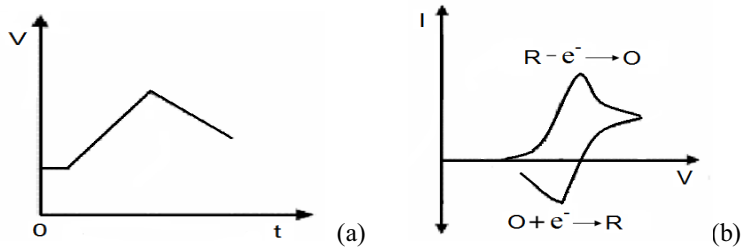

Fig. 2.7 (a) signal of CV, (b) response of CV.

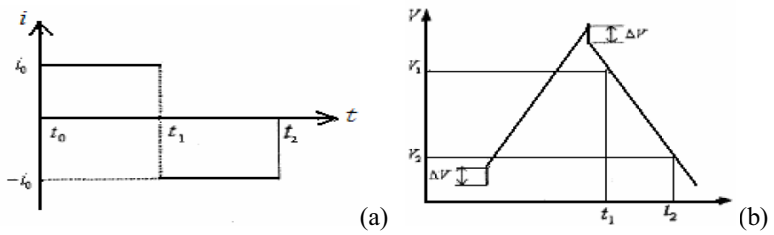

Fig. 2.8 (a) signal of GCD, (b) response of GCD.

EIS is another commonly used method for supercapacitor characterization. When a very small sinusoidal signal with frequency of ω is added on a stable electrode system (Fig. 2.9 (a)), there must be an output of the potential between WE and RE with frequency ω. The frequency response function of the electrode system at a series of frequencies is the EIS of the electrode system. From EIS data, Nyquist plot (Fig. 2.9 (b)), Bode plot and Cole-Cole plot can be achieved, and then the detailed dynamics of electrode reactions can

be obtained, such as the equivalent circuits, time constant, and apparent diffusion coefficient. [59,60]

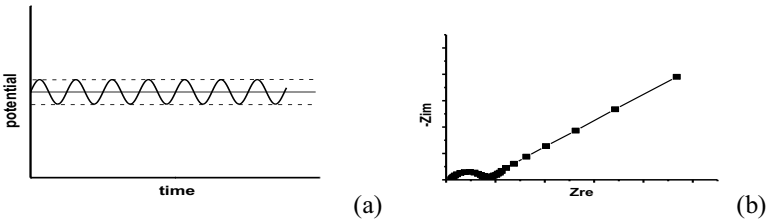

(a) (b)

Fig. 2.9 (a) signal of EIS, (b) Nyquist plot obtained from EIS data.

2.7 Chapter conclusions

In this chapter, from the basic energy and power equations of supercapacitors, I have discussed the design rules for supercapacitors with high capacitance and power density. Two types of 3D MEMS supercapacitors are systematically designed. Finally, electrochemical characterization methods are introduced for better understanding of text in latter chapters.

Chapter 3 3D MEMS supercapacitor based on LIGA-like technology

In this chapter, fabrication of the 3D MEMS supercapacitor based on LIGA-like technology is presented. Both capacitance and power densities of the supercapacitors are characterized by electrochemical methods. The work in this chapter has been published in Microelectronic Engineering [61].

3.1 Design of process flow for fabrication

As designed in chapter 2, on a silicon substrate, the 3D MEMS supercapacitor includes two nickel current collectors with interdigital structure which is coated with conformal polypyrrole (PPy) film, and state electrolyte filling-in all the interdigital spacing. The processes flow for fabricating the supercapacitor was designed as shown in Fig. 3.1. At first, a thin nickel layer will be deposited on a SiO_2/Si substrate by using RF magnetron sputtering, which will be the seed lay for electroforming. As the second step, thick SU-8 photoresist will be applied on the top of nickel layer by spin coating, which will be used as structuring material. Thereafter, the interdigital pattern will be transferred by UV lithography which will be the mold for forming current collectors. For the fourth step, nickel current collectors will be deposited by using electroforming, and the SU-8 mold will be removed. Then, PPy films will be electrochemically polymerized on the current collectors. Finally, solid state electrolyte will be filled in all the interdigital spacing.

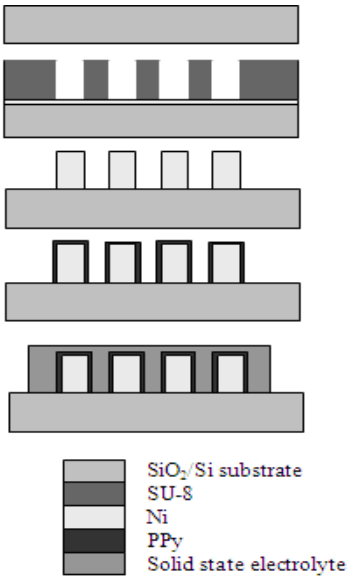

Fig. 3.1. Design of fabrication processes for fabricating 3D MEMS supercapacitor.

3.2 Processes development

All the fabrication processes of the 3D MEMS supercapacitor, including SU-8 lithography, nickel electroforming, PPy polymerization and solid state electrolyte filling-in, were investigated with various conditions and successfully optimized.

3.2.1 Oxidation and nickel seed layer deposition

As received 4 inch silicon wafers were cleaned in H_2SO_4/H_2O_2 solution, $NH_3/H_2O_2/H_2O$ solution and $HCl/H_2O_2/H_2O$ solution in sequence to remove grease, silicon dioxide and metallic impurity on the surface of silicon wafer. Hot de-ionized (DI) water was used to wash the residual solution after each cleaning step. Then, a dry thermal oxidation/wet thermal oxidation/dry thermal oxidation process was carried out to grow about a 1.5 μm silicon oxide layer on the surface of silicon wafer as insulation layer, the total oxidation time was about 10 hours. At last, a ~300 nm thick nickel layer as the seed layer for electroforming was deposited by RF sputtering on the wafer covered with silicon oxide.

3.2.2 SU-8 lithography

SU-8 is a negative, epoxy-type, near-UV photoresist based on EPON SU-8 epoxy resin (from Shell Chemical) that has been originally developed and patented by IBM [62]. This photoresist can be fabricated into structure as thick as 2 mm with aspect ratio >20. SU-8 2150 [63] from microchem was adapted in this experimental work, which was used to SU-8 layer ranging from 200 μm to 650 μm in thickness. A typical SU-8 process flow can be seen in Fig. 3.2 [63]. Prior to use, the SU-8 is taken from the refrigerator and warmed up to ambient temperature, the substrate is cleaned and activated by plasma cleaning. SU-8 photoresist is coated by using spin coating or other coating methods. By removing the edge bead appeared on during the spin coating, better contact lithography can be achieved, resulting in proved resolution and aspect ratio. Following that, the pre-bake of SU-8, takes place on a hot plate rather than an oven. This is because that the photo resist hardening benefits from the temperature gradient enabled by the "bottom to top" heating scheme of hot plate. After pre-bake and cooling of the wafer, exposure is carried out. Followed by post-exposure-bake (bard bake) done on a hot plate to cure the exposed structures. Development of SU-8 is done by soaking the wafer in SU-8 developer with agitation. Finally, Isopropyl Alcohol (IPA), acetone and ethanol bath are used several times to remove the residual SU-8 and developer, and nitrogen gas is applied to blow the wafer and cured SU-8 structures.

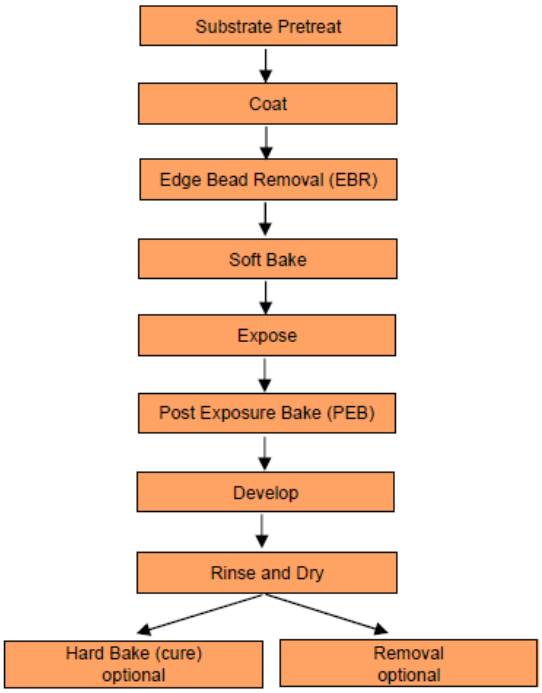

Fig.3.2 Typical SU-8 process flow [63].

The SU-8 processing looks more like an art than an exact science, because there are a lot of types of SU-8 photoresist and every single parameter during SU-8 processing, including spin rate, spin time, pre-bake temperature and time, exposure dose, post-exposure-bake temperature and time, can affect the ultimate results. So, a series of orthogonal experiments were designed and carried out to optimize the SU-8 lithography, as can be seen in Table 3.1. There are 7 factors and each factor has 2 levels in this experimental design including spin rate (SR) of 1500/1800 rpm, spin time (ST) of 25/35 s, pre-bake temperature (PB temp) of 90/100 ℃, pre-bake time (PBT) of 2/4 hours, exposure time (ET) of 280/320 s, post-exposure-bake temperature (PEB temp) of 95/105 ℃, post-exposure-bake time (PEBT) of 2/4 hours.

Fig. 3.3 shows the mask for SU-8 lithography, which contains five groups of 20 single cells. By using this mask, interdigital SU-8 molds with various spacing sizesfrom 20 μm to 100 μm will be fabricated. The mask was designed by software L-Edit and produced by Supermask Com Co. Ltd. [64].

Table 3.1 Orthogonal experiments of SU-8 lithography

Factors	SR	PB temp.	PBT	ET	PEB temp.	PEBT	ST	Results
Exp.1	1500	90	2	280	95	2	25	2.5
Exp.2	1500	90	2	320	105	4	35	1
Exp.3	1500	100	4	280	95	4	35	3.5
Exp.4	1500	100	4	320	105	2	25	1.5
Exp.5	1800	90	4	280	105	2	35	1.5
Exp.6	1800	90	4	320	95	4	25	4
Exp.7	1800	100	2	280	105	4	25	1
Exp.8	1800	100	2	320	95	2	35	3
Mean 1	2.125	2. 25	1.875	2.125	3.25	2.125	2.25	
Mean 2	2.375	2.25	2.625	2.375	1.25	2.375	2.25	
Range	0.25	0	0.75	0.25	2	0.25	0	

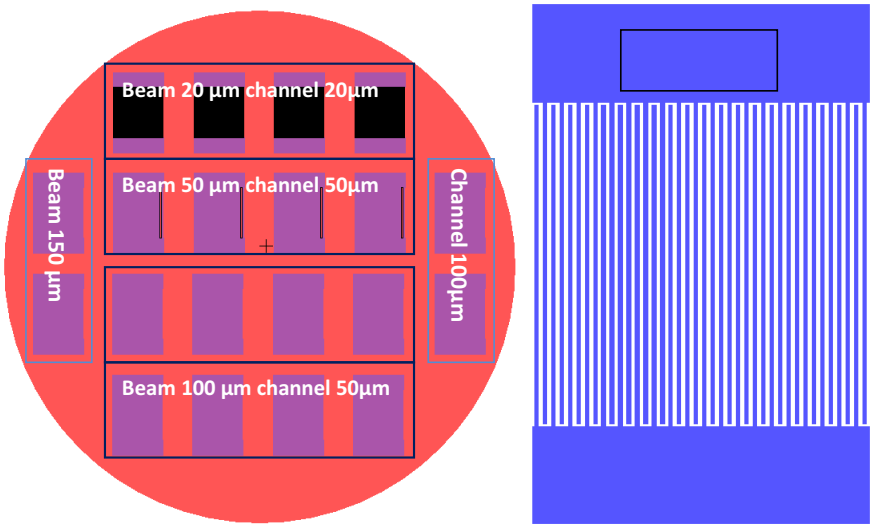

Fig. 3.3 Mask for SU-8 lithography

After performing the 8 orthogonal experiments, the results were evaluated by grading the uniformity of the SU-8 molds after development from 0 to 5 with optical microscope. As shown in Fig. 3.4 the grade of (a), (b), (c) was set as 0, 2, and 4, respectively. It was

very difficult to develop the unexposed SU-8 photoresist for cells with channel size of 20 μm even very long time was used. However, the uniformity of SU-8 molds with spacing of 50 μm and 100 μm can be graded up to 3 or 4. This is because:

1) At the spin rate of 1500 to 1800 rpm, the thickness of the SU-8 layer is generally from 500 to 350 μm. For single cells with channel size of 20 μm, the aspect ratio will be up to 25, which is too high to achieve.
2) The photomask is based on film material, so the precision (about 2 μm) is not good enough.

Fig. 3.4 Three different level of SU-8 lithography results from orthogonal experiments. (a) level 0, (b) level 2, (c) level 4.

The evaluation grades of the orthogonal experiments are shown in Table 3.1 (the cells with channel size of 20 μm are not considered). Then, the mean values and the range of two levels for the seven factors were calculated. As shown in Table 3.1, row "mean 1" of each factor represents the average value of grades related to the first level of this factor. For example, the first level of spin rate of 1500 rpm, have been used 4 times together with other factors, so the mean 1 of spin rate is (2.5+1+3.5+1.5)/4=2.125. The mean 2 of spin rate of 1800 rpm is 2.375. The two levels of spin rate were used together with the levels of other factors evenly. The range of the two levels of a factor means how important of this factor is, the bigger the range, the more important the factor is. In the orthogonal experiments, the post-exposure-temperature is found to be the most important factor, with the range of 2. Meanwhile, the ranges as 0 for the pre-bake temperature and spin time, which means the pre-bake temperature at 90 or 100 ℃ and the spin time of 25 or 35 s don't affect the results very much. From the orthogonal experiments, it has been found the optimized conditions for SU-8 processing are: SU-8 spin rate of 1800 rpm for 25 s,

pre-bake at 95 ℃ for 4 hours, exposure for 320 s, and post-exposure-bake at 95 ℃ for 4 hours.

By using the optimized conditions, the detailed SU-8 photolithography process is as follow. The SU-8 spinning and heating treatments were performed by Dominus coater OPTI coat 22i from SSE sister Semiconductor Equipment GmbH, Germany. At first, about 5 ml SU-8 resist was slowly dispensed manually on the center of the wafer, and the spin profile was programmed as shown in Fig. 3.5 (a). Two steps at 250 rpm and 500 rpm spinning was conducted before a step of 1800 rpm as buffering, and one step of 500 rpm after the step of 1800 rpm was performed for edge bead removal. The edge bead removal step was carried out by injecting acetone on the edge of the substrate for few seconds, with the cover of spinner opening. In this sequence, improved uniformity of the SU-8 was obtained, thus result in a better photolithography quality. The pre-bake profiles can be seen in Fig. 3.5 (b). After spin coating, the wafer with SU-8 was placed on well–leveled hotplate at room temperature for 2 hours for bubbles escape, then two steps at 50℃ and 70℃ for 0.5 hours were set as temperature buffering. It is very important to control the heat flow especially when the temperature is at around 70℃, otherwise, bubble or “islands” will show up in Fig. 3.6. A 5 inch culture dish was used to cover the wafer to decrease the evaporation rate of the solvent in SU-8 photoresist. The small space between the culture dish and the hotplate enables solvent vapor reflowing. SU-8 exposure process was performed on Karlsuss MA6/BA6 for 320 s in hard contact mode. In order to obtain vertical sidewalls in the SU-8 photoresist, a light filter was used to eliminate UV radiation below 350 nm. Post-exposure bake was employed right after exposure with the same profile as pre-bake. The development process was carried out in a culture dish with 20 ml developer. Agitation was applied to accelerate the developing speed. Fresh developer was added into the dish at regular intervals. Finally, the wafer was rinsed by organic solvent and dryed by nitrogen gas. Fig. 3.7 shows the single cell with beam size of 50 um and channel size of 50 um, with uniform height of about 450 μm.

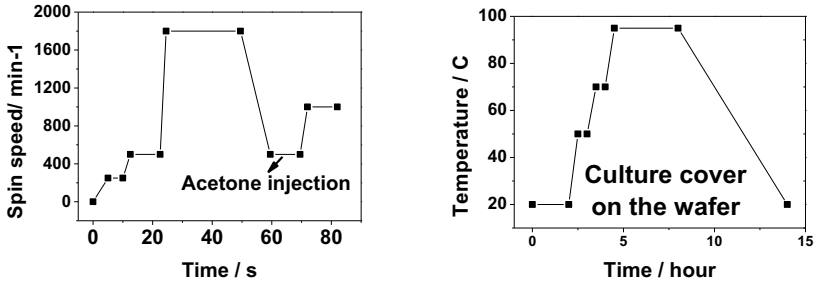

a b

Fig. 3.5 (a), SU-8 spin profile, (b) Pre-bake and post-exposure-bake profile.

Fig.3.6 SU-8 with twist-look after pre-bake without culture dish covering.

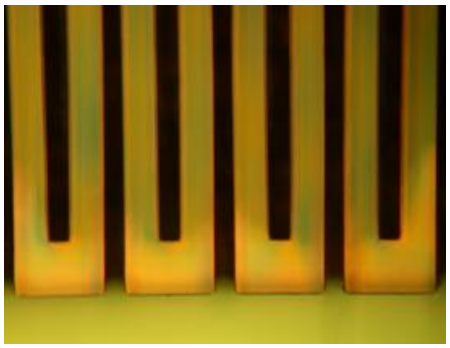

Fig. 3.7 Single SU-8 mold, beam width 50 um, channel width50 um, and height 450 μm.

3.2.3 Nickel electroforming

In an ordinary electroforming process, an electrolytic bath is used to deposit nickel or other electroplatable metal onto a conductive patterned surface. This process allows high quality duplication and therefore permits quality production at low unit costs with high

repeatability and easy process control. Electroforming is a metal forming process that deposits thin parts through an electroplating process. The plating is much thicker and can exist as a self-supporting structure when the mold is removed. Fig. 3.8 [65] shows the schematic drawing of nickel electroforming process.

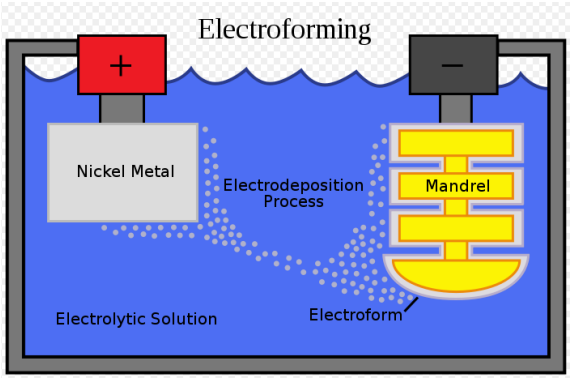

Fig. 3.8 Schematic drawing of electroforming process [65].

Nowadays, the metal electroplating technologies for copper, nickel and zinc are mature and being used widely in industrial production. For nickel electroplating or electroforming, the electrolyte is very important which affects the electroplating quality significantly. There are three kinds of mature electrolyte baths, watts bath [66], all-chloride bath [67] and sulfamate bath [68]. Among these methods, the nickel electroplated in all-chloride bath have much larger inner stress, the chemicals in sulfamate bath is relatively expensive, Thus the watts bath system was chosen in our experiment. The typical components of watts bath are nickel sulfate, nickel chloride and boric acid.

Instead of $NiCl_2$, NaCl was used in the electroforming experiments for its low price. The components/concentrations are $NiSO_4$/240 gl^{-1}, NaCl/15 gl^{-1}, H_3BO_3/45 gl^{-1}. Each component in the watts bath performs an indispensable role in electroforming process. The inexpensive nickel salt $NiSO_4$ is the major source of the nickel ions and is generally maintained in a constant concentration. NaCl is enhancing anode corrosion and improves the conductivity of the watts bath. H_3BO_3 buffers the hydrogen ion concentration (pH) around the cathode region. Without this buffering reaction, the pH value in the higher current density region of the cathode would increase very quickly. Nickel hydroxide would be precipitated and co-deposited along with hydrogen, resulting in a green nodulation or

burned deposit. In addition, 80 gl^{-1} $MgSO_4$ was used as second cathodic salt to increase the conductivity of nickel, two organic chemicals saccharine (0.5-1gl^{-1}) and sodium dodecylsulphate (0.05-0.1gl^{-1}) were added to reduce the interface and the roughness of nickel. The pH value of this electrolyte was about 4.00 and well controlled with the tolerance less than 0.30. The operating temperature was 40±5 ℃.

Because the depth of prepared SU-8 mold is about 450 μm, it will take very long time while small current density is applied. Assuming the electroforming efficiency is 100% and the current density is 1 $mAcm^{-2}$, the electroforming time will be more than 360 hours according to the Faraday's law. The operating current density is needed to keep at small value to get better quality of electroforming. So, it is needed to find out a balance of current density considering the both the operating time and electroforming quality. Experiments of electroplating were carried out with the constant current densities from 1 to 100 $mAcm^{-2}$. Agilent E3631A was used to provide constant current supply for electroplating. Agitation by magnetron stirring was employed to keep the uniformity of the electrolyte bath and take the bubble away from the surface of cathode. It was found that the plated nickel has good uniformity when the current density is less than 50 $mAcm^{-2}$ (Fig.3.9(a)). While applied with current density larger than 50 $mAcm^{-2}$, there are bubbles on the plated surfaces resulting from fast reaction, which can be seen from Fig. 3.9(b).


(a)

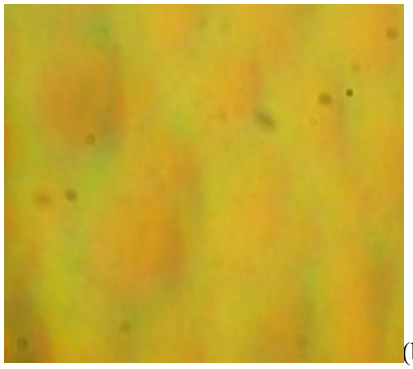
(b)

Fig. 3.9. Nickel electroplating at different current densities, (a) 20 $mAcm^{-2}$, (b) 100 $mAcm^{-2}$.

The current density of 20 $mAcm^{-2}$ was adapted for nickel electroforming, the corresponding electroforming time can be estimated as about 18 hours. The prepared SU-8

mold was cut into single cells, and then pretreatment was done before electroforming. The pretreatment procedure is performed by soaking the single cells in hot NaOH solution for 5 minutes to remove grease then in 30% HCl solution for 10 seconds to activate the surface of sputtered nickel on the Si/SiO_2 substrate. The electroforming was carried out at 20 $mAcm^{-2}$ current density in small electrolytic bath containing above mentioned components on a magnetron stirring machine with constant temperature control. After about 20 hours, the electroformed nickel reached the thickness of 450 μm. Then the SU-8 mold was removed. There are several methods for SU-8 removal. One of the methods is using O_2 and CF_4 plasma [69], which is ineffective for very thick SU-8 removing. Another method is using molten salt bath such as sodium nitrate mixed with a hydroxide salt and potentially other additive [70]. The easiest and most overlooked process for removing SU-8 is to simply burn it off, but there will be significant damage on the resultant metal because about 600 ℃ temperature for several hours is required [71]. In this research, wet etching method (H_2O_2:H_2SO_4=1:4) was used to remove the SU-8 mold. By using wet etching method, the SU-8 was oxidized and dissolved, but the nickel was also oxidized. Then HCl solution was used to etch the nickel oxide. The designed interdigital nickel structures were obtained as shown in Fig. 3.10.

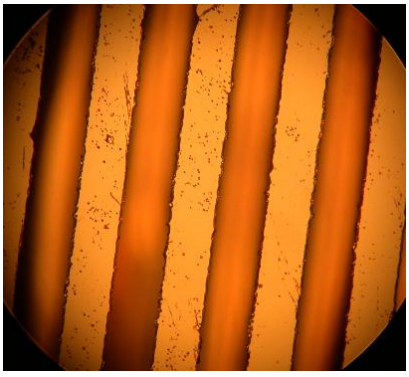

Fig. 3.10 Nickel current collectors achieved by electroforming, 50 μm of width for each beam and channel.

Besides single cell electroforming, wafer level electroforming system was set up. As shown in Fig. 3. 11, it contains an electrolytic bath with the volume of 30*30*30 cm^3, a temperature control system with heating and detecting functions, a cycling pump to filter

the solid powder and keep the concentration of electrolyte, a power source, an anode target and a rotating motor connected to wafer through wafer holder. The holder is made up of polytetrafluorethylene with embedded copper wire, which can be seen in Fig. 3.12.

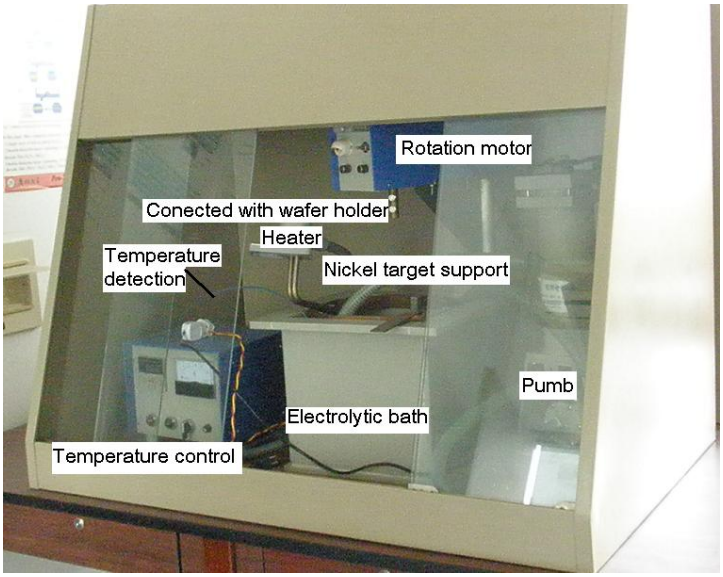

Fig. 3.11 Schematic drawing of wafer level electroforming system

Fig. 3.12 Picture of wafer holder for wafer level electroforming.

3.2.4 PPy polymerization

PPy, as the electroactive material of supercapacitor, has good stability in aqueous solution and air, as well as high conductivity. The capacitance properties of PPy which as the electrode of supercapacitors, is determined by the preparation conditions, such as synthesis method, temperature, current density or potential, pH and doping ions [72]. Song et al. [73] reported that the PPy doping with ClO_4^- had large specific capacitance than that of

NO_3^-. Ingram et al. [74] prepared 'Ladder-doped' PPy doping with polysulfonated aromatic anions which had very fast charge/discharge ability but lower specific capacitance. PPy film doping with Cl^- prepared by Hu etal, [75] at 0 ℃ presented ideal supercapacitor properties with specific capacitance of 260 Fg^{-1}, however, the specific capacitance decreased with increasing polymerization charge. Compare to chemical polymerization method, electrochemical polymerization of PPy is suitable for the 3D interdigital $Si/SiO_2/Ni$ structures. Generally, there are constant current, constant voltage and potential dynamic methods for electrochemical polymerization. Constant current method was used in this research for PPy polymerization because that it can be carried out with simple two-electrode-system and the charge can be easily controlled by current density and time. As shown in Fig. 3.13, the experiment facility makes up of a power supply, a simple beaker as electrolytic bath, a pH meter, a magnetron stirring machine to provide agitation, an iron pedestals to hold the $Si/SiO_2/Ni$ anode, a Pt cathode, a pH meter and a drop funnel which is used for pH value adjusting at all the time of PPy polymerization. In addition, water/ice baths can be added into this system to control the temperature ranging from 0 ℃ to room temperature.

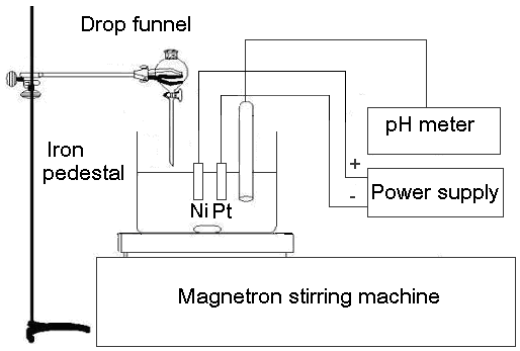

Fig. 3.13 Schematic drawing of PPy electropolymerization system.

Before PPy polymerization, sodium *p*-toluenesulfonate (TOSNa, AR) was first dissolved in DI water in electrolytic bath. Then *p*-toluenesulfonate acid (TOSH, AR) was added into the bath to adjust desired pH value. After sufficient agitation by magnetron stirring, Py (Fluka, 99%) purified by vacuum distillation was added into the bath by burette while keeping stirring. When the Py was totally mixed with other components in the bath,

$Si/SiO_2/Ni$ anode and Pt cathode were put into the bath after washing. At last, turned on the power supply, and adjusted the current density.

There are some parameters affect the PPy polymerization including the concentrations of Py and TOS^-, pH value of the electrolyte, temperature and current density. It was very difficult to grow continues PPy on $Si/SiO_2/Ni$ structures when the current densities was less than 5 $mAcm^{-2}$, despite changing other variables. This is because the subsidiary reactions of $Ni\text{-}2e\text{->}Ni^{2+}$. When the current density is small, the slowly polymerized PPy cannot coat on the dissolving nickel. While under high current density, the PPy polymerization rate is fast so that PPy can deposit quickly on the surface of nickel and separate the nickel and electrolyte, thus PPy polymerization can be continued. But the uniformity and capacitance properties of PPy polymerized at high current density are not satisfying. So, two-step polymerization method were used for PPy polymerizaiton on the nickel current collectors, with high current density polymerization of PPy for only several seconds as surface modification to separate nickel and electrolyte, and then small current density polymerization of PPy for longer time. The optimized PPy deposition conditions are: concentration of Py 0.1 M, concentration of TOSNa 0.3 M, constant pH 4.00, temperature 20℃ and current density $1mAcm^{-2}$. After 30 min polymerization, the continuous 3D micro PPy electrodes were formed as shown in Fig. 3.14. The surface area of each 3D PPy electrode was about 5 cm^2, the value that is 20 times more than the plane structure of same area. Before solid state electrolyte filling-in, undoping of both PPy electrodes were carried out.

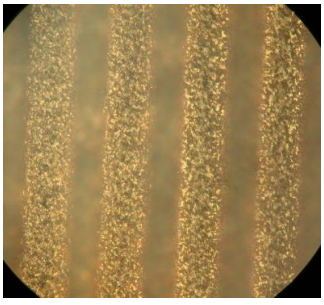

Fig. 3.14 3D micro PPy electrodes for supercapacitor, with 50 μm of width for each beam and channel.

3.2.5 Solid state electrolyte coating

Nowadays, the commercial supercapacitors are based on liquid electrolytes. But with development of solid state electrolyte of lithium batteries, there have been some investigations on solid state electrolytes for supercapacitors. Solid state electrolyte enables higher operating temperature and safety. At the very beginning, a limited number of solid state systems have been studied with polymer/gel electrolytes, such as poly(ethylene oxide) (PEO) based electrolytes [76], as well as poly(methyl methacrylate) PMMA based electrolyte [77]. Since studies by Bates et al. [78] and Jeon et al. [79] have demonstrated that the Lipon solid state electrolyte is suitable for thin film batteries, Yoon et al. [80] proved that this Lipon material is also suitable for solid state supercapacitors based on RuO_2 electrodes. Park et al. [81] fabricated an all solid state supercapacitor by using a Nafion membrane and an ionomer, which is commonly used in full cells. Lipon and Nafion material are always fabricated by sputtering, which is not suitable to fill in the 3D interdigital spacing. Wang and Zhang [82] fabricated a solid state supercapacitor with phosphotungstic acid as the proton conducting electrolyte. Sung et al. [33] reported a solid state electrolyte for PPy based planar micro supercapacitor, which is Polyvinyl Alcohol (PVA) based gel PVA/ H_3PO_4/H_2O. The PVA based gel should be suitable for the designed supercapacitor in this chapter. The valence of inions in the electrolyte will affect the ion exchange properties in PPy electrodes[83].It is expected that the solid state electrolyte will contain inions with negative valence of -1, because the valence of counter ions TOS^- is -1. Perchloride ion ClO_4^- was chosen as the diffusion charge in the designed supercapacitor.

The $LiClO_4$/ H_2O/PVA solid state electrolyte was prepared as following. At first, PVA powder was added into DI water in a beaker. Then the beaker was placed on magnetron stirring machine with vigorous stirring, and controlled at 95 ℃ for several hours. When the solution became transparent, stopped heating and let it cooled down to room temperature. $LiClO_4$ was first dissolved in perchloride acid and then the mixture was added into the cooled PVA solution. Then the aqueous solution containing PVA, $LiClO_4$ was mixed for more than 10 hours with stirring. The totally mixed homogeneous solution was heated at

40 ℃ to loss some water. When the solution became sticky, it was poured on the $Si/SiO_2/Ni/PPy$ structure to fill in all the channels and cover all the PPy as shown in Fig. 3.1. Finally, the 3D MEMS supercapacitor was heated at 40℃ for evaporation of the excess water until the electrolyte became totally solid state.

All the fabrication processes of the designed 3D MEMS supercapacitor based on LIGA-like technology are successfully developed. The electrochemical properties of the 3D MEMS supercapacitor will be investigated in next section.

3.3 Electrochemical tests

CV and EIS tests for single PPy electrode were carried out in a three-electrode system (as shown in Fig. 3.15a) with the Pt sheet as counter electrode and saturated calomel electrode (SCE) as reference electrode in 0.3M LiClO4 solution, the potentials in three-electrode system which will be mentioned later are versus SCE for single PPy electrode. GCD tests for the supercapacitor were carried out in a two-electrode system (as shown in Fig. 3.15b) with two PPy electrodes as cathode and anode, respectively. The electrochemical tests were performed on electrochemical workstation. The capacitance density and power density are the most important parameters for supercapacitors, which can be defined as capacitance and power per weight or per footprint. For MEMS supercapacitors to be used in microelectronics or with other MEMS devices, the capacitance and power per footprint are more realistic. So the performances of the 3D MEMS supercapacitors were characterized with, specific capacitance (or geometric capacitance) and specific power (or geometric power).

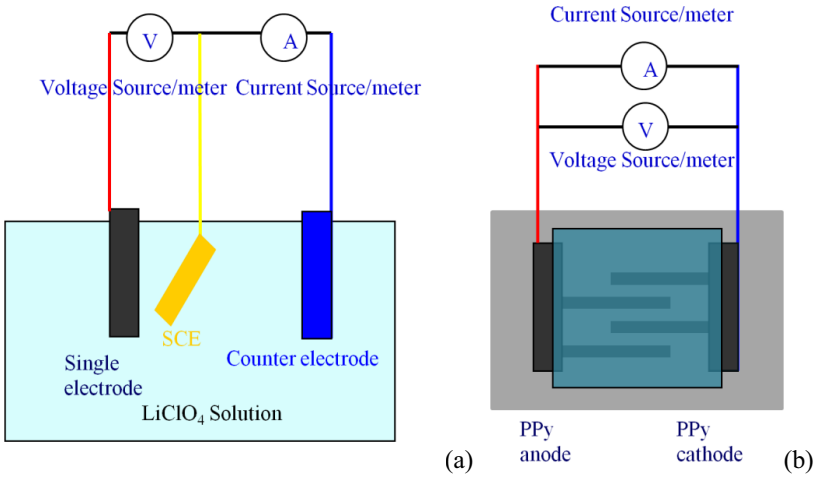

Fig. 3.15 Schematic drawing of electrochemical testing system, (a) Three-electrode system, (b) Two-electrode system.

3.3.1 CV tests

The CV test of single electrode was carried out at 20 mVs^{-1} with the potential ranged from -0.8 to 0.4 V, (as shown in Fig. 3.16. It is found that the anodic and cathodic Faradic currents are close to each other (-0.8 to -0.6 V), which means the specific capacitance is small in this range. The potential window U was set from -0.6 to 0.4 V (totally 1.0 V), and the CV curve at 20 mVs^{-1} in this potential window (as shown in Fig. 3.16). In which, the average currents of both cathodic and anodic cycle are about 0.001 A. The specific charge and discharge capacitances for each scan cycle can be obtained from the curve of electric quantity (Q) vs. time, (as shown in Fig. 3.17). The specific charge electric quantity (Q_c) and discharge electric quantity (Q_d) are 0.065 and 0.058 Ccm^{-2}, respectively. The specific charge and discharge capacitances (C_c and C_d) can be calculated by Eq. 3.1 and Eq. 3.2, which are 0.065 and 0.058 Fcm^{-2}, respectively. The coulombic efficiency η can be calculated as 89.23% by Eq. 3.3.

$$C_c = Q_c / U \tag{3.1}$$

$$C_d = Q_d / U \tag{3.2}$$

$$\eta = C_d / C_c \times 100\% \tag{3.3}$$

The specific power P can be obtained from Eq. 3.4,

$$P = \frac{E}{\Delta t} = \frac{C_d \times U^2}{2\Delta t} = \frac{C_d \times U \times S}{2} \tag{3.4}$$

where E is the specific energy, Δt is the discharge time, and S is the scan rate. Thus, the specific power of the single electrode is 0.58 $mWcm^{-2}$ at scan rate of 20 mVs^{-1}.

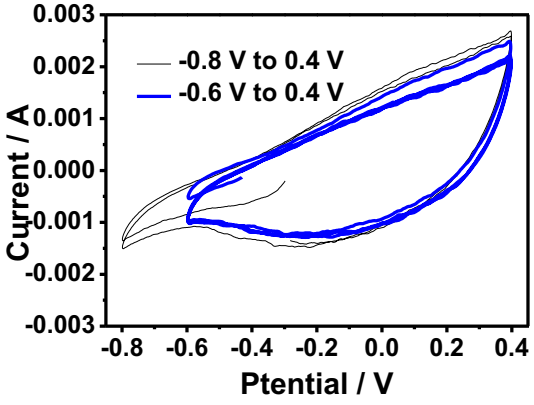

Fig. 3.16 CV of single PPy electrode at 20mVs^{-1} scan rate.

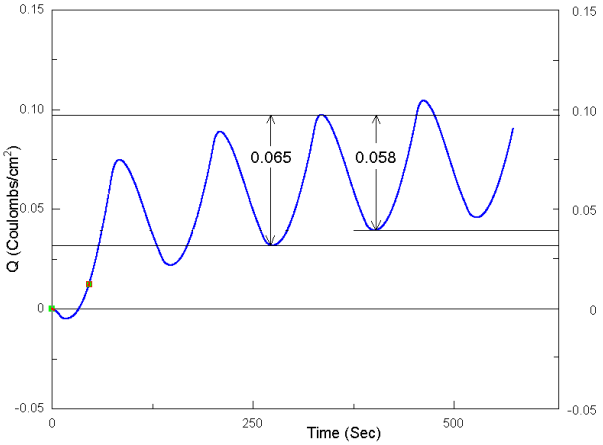

Fig. 3.17 Electric quantity vs. time at 20 mVs^{-1} scan rate.

CV tests at different scan rates of 1mVs^{-1}, 5mVs^{-1}, 50mVs^{-1}, and 100mVs^{-1} were also done with the potential range from -0.6 to 0.4 V. The specific capacitances, the specific powers and coulombic efficiencies at different scan rates were obtained from CV data. Fig.

3.18 presents the specific capacitances and specific powers at scan rates from 1 to 100 mVs^{-1}. It was found that specific capacitances drop very fast with scan rate ranging from 1mVs^{-1} to 20mVs^{-1}, and much slower when scan rate ranging from 20mVs^{-1} to 100mVs^{-1}. It means that rate of ion diffusion cannot follow the fast scan rate. From the dynamic point of view, there are two factors to determine the rate of ion diffusion, the first is the speed of ion diffusion inside PPy matrix (doping and unpoding), the second is the mobility of ion in the solid state electrolyte. These two limitations of ion diffusion may correspond to the two regions divided by 20 mVs^{-1} in Fig. 3.18. Fig. 3.18 also presents specific powers in the single electrode of the supercapacitor at various scan rates. Though the specific capacitance decreased with the increasing scan rates, the specific power increased significantly since the high discharge rate. The highest 1.75 $mWcm^{-2}$ specific power was obtained at 100 mVs^{-1} scan rate. Fig. 3.19 gives the relationship of coulombic efficiency with scan rate. It was found that the coulombic efficiency of the single electrode increase from 77.27% to 97.32% with increasing scan rate from 1 to 100 mVs^{-1}. Compare to the discharge capacitance, the charge capacitance decrease more.

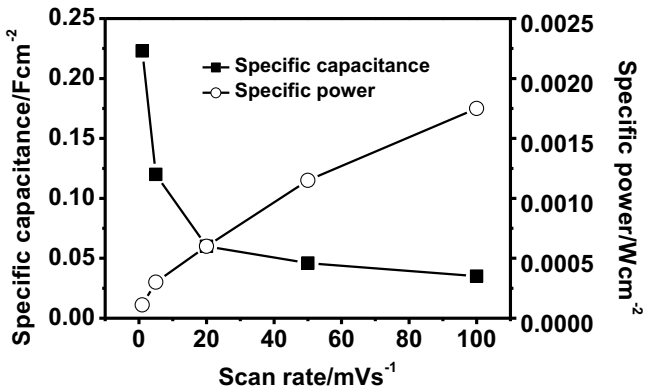

Fig.3.18 Specific capacitances and specific power at various scan rates 1mVs^{-1}, 5mVs^{-1}, 20mVs^{-1}, 50mVs^{-1}, and 100mVs^{-1}.

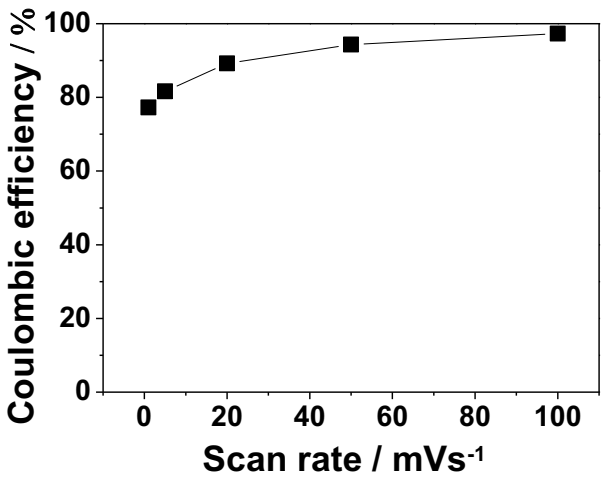

Fig. 3.19 Coulombic efficiencies of single electrode of supercapacitor at various scan rates.

3.3.2 EIS test

EIS test of the single PPy electrode was carried out at open circuit potential (OCP) before and after CV tests. The operating conditions are at a frequency range between 0.1 Hz and 100 kHz under potential amplitude of 10 mV. Fig.3.20 presents Nyquist plot obtained before CV tests form EIS data. It was found the Nyquist plot was typically divided into high and low frequency regions by "knee" frequency (316 Hz) [84]. The EIS data can be fitted by an equivalent circuit (with software ZView2) as shown in Fig. 3.20, where R_1 is the resistance of the electrolyte and connections, R_2 is the charge transfer resistance, instead of pure capacitors the two constant phase elements CPE_1 and CPE_2 were used to describe the capacitances at high and low frequencies, respectively. The Nyquist plot achieved after CV tests (as shown in Fig. 3.21), is very close to the result before CV tests. The fitted results for both EIS tests before and after CV tests are shown in Table 3.2. Equivalent circuits fitting provides error estimates for each variable as well as general accuracy of the fitting values. Error estimates are calculated by testing several solutions near the best fit. The Chi-Squared is the square of the standard deviation between the original data and the calculated spectrum. It can be found that the values of each modeling components before and after CV tests are close to each other, except the value of R_1 before

CV tests is larger than it after CV tests. Because the PPy electrode before CV tests is undoping state, which has larger resistance than the doping state PPy electrode after CV tests. It proves the single electrode has good stability of cycling. It can also be found that the magnitude of CPE_1 (0.0002 Fcm^{-2} double layer capacitance) is far less than CPE_2 (0.027 Fcm^{-2} pseudocapacitance), which means that the PPy single electrode can store more electric energy at low frequency less than 316 Hz. In applications of low frequencies, the specific capacitance of the single electrode of supercapacitor is 0.027 Fcm^{-2}.

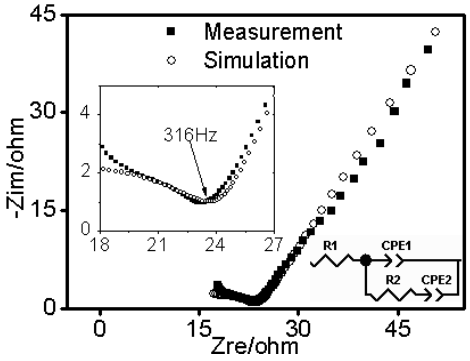

Fig. 3.20.Nyquist plot and simulation of single PPy electrode.

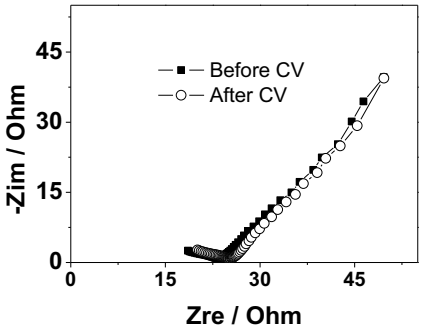

Fig. 3.21. Nyquist plot of single PPy electrode before and after CV test.

Table 3.2. Parameters of modeling equivalent circuit.

Element	Before CV		After CV	
	Value	Error%	Value	Error%
$R_1(ohmcm^{-2})$	9.087	23.9	4.433	82.7
$CPE_1(Fs^{1-\alpha 1}\ cm^{-2})$	0.0002	11.4	0.0002	18.1

α_1	0.40	5.81	0.37	6.76
R_2(ohm cm^{-2})	16.62	13.50	19.63	19.07
CPE_2($Fs^{1-\alpha 2}cm^{-2}$)	0.028	0.39	0.027	0.40
α_2	0.63	0.47	0.61	0.45

3.3.3 GCD test

The performances of the 3D MEMS supercapacitor were also tested by GCD technique with two-electrode system. Before GCD, CV was used to charge one electrode (anode) as fully doping state (CV scan to 0.4 V), and discharge the other electrode (cathode) as fully unpoding state (CV scan to -0.6 V). Then, the GCD data were obtained at various discharge rates with the potential from 1.0 V to 0.0 V. Fig 3.22 shows the charge/discharge curves at 1 $mAcm^{-2}$ with 10 cycles, the curves are almost linear in the whole potential range, which means good supercapacitor property. Fig. 3.23 shows the discharge curves at various discharge current densities. At the initial small discharge region near 1.0 V, the voltage dropped quickly due to the inner resistance of MEMS supercapacitor. The discharge capacitances were calculated from the linear part of discharge curve [85] by Eq. 3.5,

$$C_d = I \times \Delta t / U \tag{3.5}$$

where I is the discharge current density, Δt is the discharge time and U is the potential window. As shown in Fig. 3.24, the specific capacitance decreases while the specific power increases with the increasing current density from 0.5 $mAcm^{-2}$ to 5 $mAcm^{-2}$. The specific capacitance was 0.029 Fcm^{-2} and the specific power density was 2.2 $mWcm^{-2}$ at 5 $mAcm^{-2}$ current, which is a relative large discharge rate.

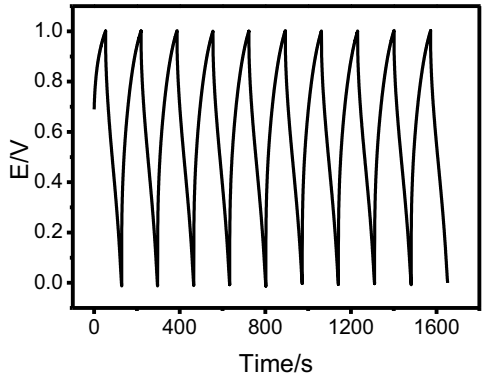

Fig. 3.22 Galvanostatical charge/discharge curve.

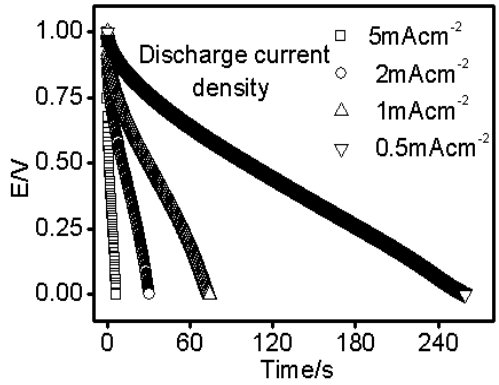

Fig. 3.23 Gavanostatical discharge curves at various discharge rates of 3D supercapacitor.

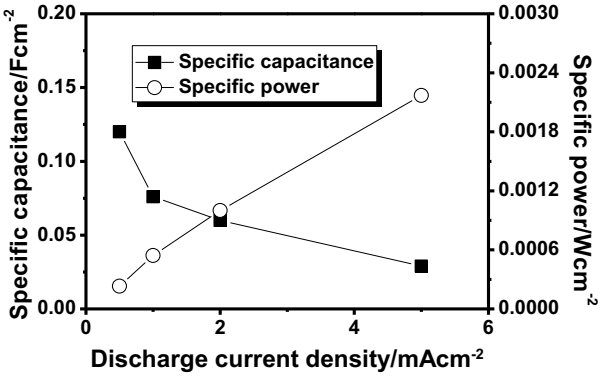

Fig. 3.24. Specific capacitance and specific power at various discharge current densities.

3. 4 Chapter conclusions

LIGA-like based 3D MEMS supercapacitor was designed with an interdigital structure which increases surface area by about 20 times compared to planar structure for the same footprint. The fabrication processes of the MEMS supercapacitor, including SU-8 lithography, nickel electroforming, PPy polymerization and solid sate electrolyte coating, were successfully developed. Electrochemical tests showed that the single electrode have 0.058 Fcm^{-2} specific capacitance and 0.58 $mWcm^{-2}$ specific power at 20mVs^{-1} scan rate with coulombic efficiency of 89.23%. The EIS results before and after CV tests exhibit almost the same performance which implied good stability of the electrode of the 3D MEMS supercapacitor. The supercapacitor can be used in applications of broad frequency range up to 300Hz. GCD tests showed that the specific capacitance and the specific power of the 3D MEMS supercapacitor were 0.029 Fcm^{-2} and 2.2 $mWcm^{-2}$, respectively, at a relative large discharge rate of 5 $mAcm^{-2}$. It is promising of this process flow for fabricating MEMS supercapacitors.

Chapter 4 3D MEMS Supercapacitors based on DRIE technology

In this chapter, comparison of the 3D electrode based on DRIE technology and a planar electrode is presented, the fabrication process for creating 3D MEMS supercapacitors are discussed, and a symmetric redox 3D MEMS supercapacitor based on DRIE technology is created. The fabricated 3D electrodes and the 3D MEMS supercapacitor are investigated by electrochemical methods. Part of the work in this chapter have been published in Journal of power sources and Advanced materials research [86,87,88].

4.1 Comparison of 3D electrode and planar electrode for MEMS supercapacitors

3D structure enables effective surface area magnification in comparison to planar structure. A novel 3D electrode based on DRIE technology is designed and fabricated, which has more surface area compare to the planar electrode for the same footprint. A planar electrode is also fabricated to be compared with 3D. The capacitance properties of the 3D and planar electrodes are investigated by means of CV, EIS and GCD.

4.1.1 Design of 3D electrode

The electrode of MEMS supercapacitor with 3D structure was designed as shown in Fig. 4.1. It contains a Si substrate with 3D structure, a layer of SiO_2, a conformal Ni layer of current collector and a layer of continuous PPy electro active material. The 3D structure has periodic channels resulting in significant increase of effective surface area for the 3D electrode. For a square Si substrate, according to the 3D design, the surface area gain (AG) can be calculated by Eq. 4.1:

$$AG = S_{3D} / S_{planar} = L((2H + W_c + W_w) / (W_c + W_w))L / L^2 = 1 + 2H / (W_c + W_w) \quad (4.1)$$

where S_{3D}, S_{planar}, L, H, W_c and W_w are the surface area of the 3D electrode, the surface area of the similarly planar electrode, the side length of the wafer, the depth of each channel, the width of each channel, and width of each inter-channel spacing, respectively. It is apparently that the AG depends on the aspect ratio, so the high-aspect-ratio DRIE is used to form 3D structure. In this study, L, H, W_c and W_w are 1 cm, 150 μm, 120 μm and 60 μm, respectively. Thus AG of 2.7 can be achieved.

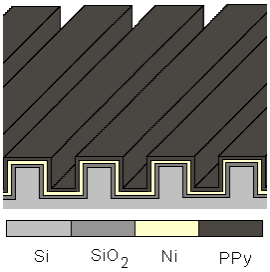

Fig. 4.1 Schematic drawing of 3D electrode based on DRIE technology

The fabrication process design for fabricating the 3D electrode is shown in Fig. 4.2A. Firstly, silicon substrate will be etched with integrated 3D structures by DRIE, and then thermal oxidation will be carried out for SiO_2 insulating layer growth. Secondly, conformal electroless plating of nickel will be coated on the surface of Si/SiO_2 substrate. Finally, conformal PPy electropolymerization will be performed on the surface of the metallic layer. Figure 4.2B shows the design of fabrication process of the corresponding planar electrode, with the same conditions of thermal oxidation, electroless plating and electropolymerization.

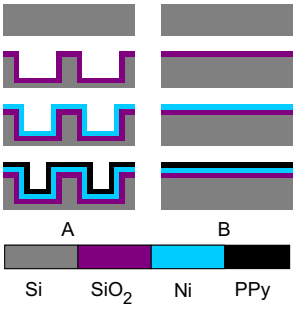

Fig. 4.2. Fabrication processes design, (A) 3D electrode, (B) planar electrode.

4.1.2 DRIE for 3D structures

DRIE is a highly anisotropic etching process to create deep, steep holes or trenches in wafers. During DRIE process, SiO_xF_y functional groups (which originate from sulphur hexafluoride and oxygen etching gases) condensate on the side walls, and protect them from lateral etching. As a combination of these processes deep vertical structures can be made. There are two technologies for DRIE, cryogenic and Bosch [89]. In this experiment, Bosch process was used. The detailed procedure for fabricating 3D structures is as follow.

At first, a silicon wafer was cleaned in H_2SO_4/H_2O_2 solution, $NH_3/H_2O_2/H_2O$ solution and $HCl/H_2O_2/H_2O$ solution in sequence to remove grease, silicon dioxide and metal impurity. Then a layer of Al with thickness of 400 nm was deposited on cleaned Si substrate by RF sputtering in 100% Ar atmosphere at room temperature. After dehydration treatment in vacuum chamber with 135 ℃ for 15 min, the Si/Al was spin coated with photoresist PB212 with the spin rate of 2000 rpm for 30s, and heated at 90 ℃ for 15 min to do soft bake in vacuum chamber. When the Si/Al/photoresist cooled down to temperature, desired pattern was transferred onto photoresist after UV exposure for 8 s, development for 40 s and hard bake at 135 ℃ for 15 min in vacuum chamber. And then, the pattern was transferred onto Al layer by etching the exposed Al in H_3PO_4/Ac(acetic acid)/HNO_3/H_2O solution, the residual Al/photoreisit layers with finger-like pattern served as the protection mask for DRIE (Al is the main layer, photoresist was etched out after few minutes). Finally, the high-aspect-ratio process DRIE was carried out by AMS200 (Alcatel, France) to form the 3D structure, by using SF_6 as etching gas and C_4F_8 as passivation gas. A 3.95 μm per minute etching speed was achieved with aspect ratio of 1.25. After removing Al mask, the 3D structure fabricated can be seen in Fig. 4.3.

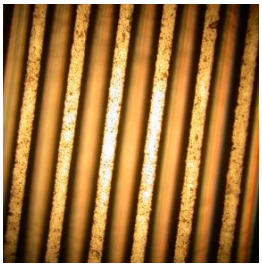

Fig. 4.3 Picture of 3D silicon structure fabricated by DRIE, 120 μm channels with 60 μm inter-channel spacing.

4.1.3 Nickel electroless plating

Electroless plating, also known as chemical or auto-catalytic plating, is a non-galvanic type of plating method that involves several simultaneous reactions in an aqueous solution, which occur without the use of external electrical power. The reaction is accomplished when hydrogen is released by a reducing agent, normally sodium hypophosphite (the hydrogen leaves as a hydride ion), and oxidized thus producing a negative charge on the surface of the part [90]. Electroless nickel plating is the most mature technology. In the electroless nickel plating process, the driving force for the reduction of nickel ions is supplied by a chemical reducing agent in solution. This driving potential is essentially constant at all points of the surface of the component, provided that the agitation is sufficient to ensure a uniform concentration of metal ions and reducing agents. Electroless deposits are therefore very uniform in thickness all over the part's shape and size. Therefore, it is very suitable for metallization of the above 3D structure.

Before nickel electroless plating, thermal oxidation was carried out for both of the above 3D structure and another as received wafer (substrate of planar electrode). Then the two wafers were cut into small pieces with 1*1 cm^2.

The electroless plating was carried out in a plating bath, with oil bath heating on a magnetron stirring machine. The experimental setup is shown in Fig. 4.4. Electric contact bimetallic thermometer was used to contact with magnetron stirring machine for temperature control of the electroless plating bath.

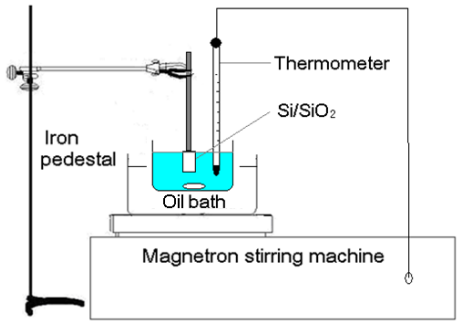

Fig. 4.4 Experiment set up for electroless plating

Because electroless nickel plating is a surface control process. So pretreatments of the Si/SiO_2 small pieces are very important, which can significantly affect the electroless

plating results, such as adhesion and uniformity of the metallic layer. The detailed procedure of electroless nickel plating is as following.

a) Removing grease: the 3D and planar Si/SiO_2 pieces were first immersed in ethanol for 10 min, then in 100 gl^{-1} NaOH solution for 10 min, and finally showered by distilled water to totally clean, ultrasonic was used to help to remove the grease on all the surfaces.

b) Coarsening: HF/NH_4F solution was used to increase the roughness of SiO_2 surface, which can enhance the adhesive force between SiO_2 and the metallic layer.

c) Heating treatment: 150 ℃ for 10 min to dry the sample and eliminate hydrogen bond on the surface of SiO_2.

d) Sensitization: the sensitization procedure is very important for electroless plating process, Sn^{2+} was absorbed at the surfaces of SiO_2 by soaking the Si/SiO_2 pieces in $SnCl_2$/HCl/H_2O (5 g : 20 m l: 500 ml) solution at room temperature for 10 min.

e) Activation: In $PdCl_2$/HCl/H_2O (125 mg : 1.25 ml : 500 ml) solution, Pd islands as the catalyst and the initial nuclear of electroless plating were deposited on the surface of Si/SiO_2, the reaction is shown in Eq. 4.2.

$$Sn^{2+} + Pd^{2+} \rightarrow Pd + Sn^{4+} \tag{4.2}$$

f) Electroless Plating: the electroless Ni plating of the Si/SiO_2 pieces were carried out in a electroless bath containing 240 gl^{-1} $NiSO_4$, 160 gl^{-1} sodium succinate, 110 gl^{-1} NaCl, 50 gl^{-1} $MgSO_4$, 50 gl^{-1} NaH_2PO_2, 30 gl^{-1} malic acid, at temperature of 90~100 ℃ (heating by oil bath) for 30 min, the reaction can be seen as Eq. 4.3.

$$3H_2O + 3H_2PO_2^{3-} + Ni^{2+} \rightarrow 3H_2PO_3^{3-} + Ni\downarrow + 2H^+ + 2H_2\uparrow \tag{4.3}$$

g) Heating treatment: the sample was dried at 150℃ for 10 mins and adhesion force between the metallic layer and substrate.

Bright, conformal and homogeneous metallic films on both 3D and planar Si/SiO_2 substrates were obtained. Fig. 4.5 presents the image of continuous metallic film deposited on the 3D Si/SiO_2 surface by Olympus OLS1200 laser scanning confocal microscope. It can be seen that the average depth of the channels is about 155 μm, the widths of channel and inter-channel are 102.50 μm and 53.75 μm. SEM and EDS were also used to

characterize the electroless plated metallic layer on the 3D Si/SiO_2 surface. As shown in Fig. 4.6, Ni and P peaks were clearly observed and there is no impurity peak except the absorption C and O, which proved that good quality Ni-P alloy films were obtained on SiO_2 surfaces. The weight ratio of P in Ni-P alloy 13.52%, so the electroless plated metallic layer belonged to high phosphorus nickel [91], which had the advantages of low porosity, excellent adhesion and uniform distribution [92].

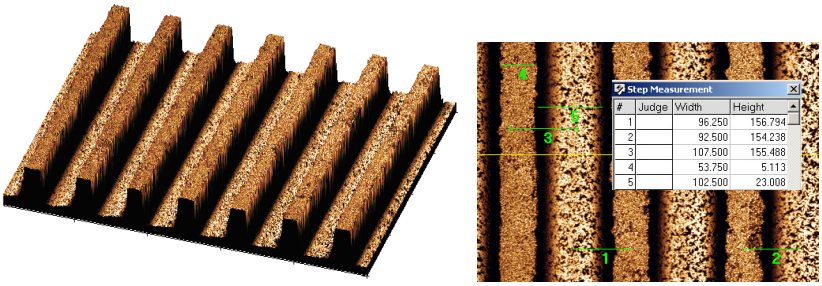

Fig.4.5 Image of nickel films on 3D Si/SiO_2 structure.

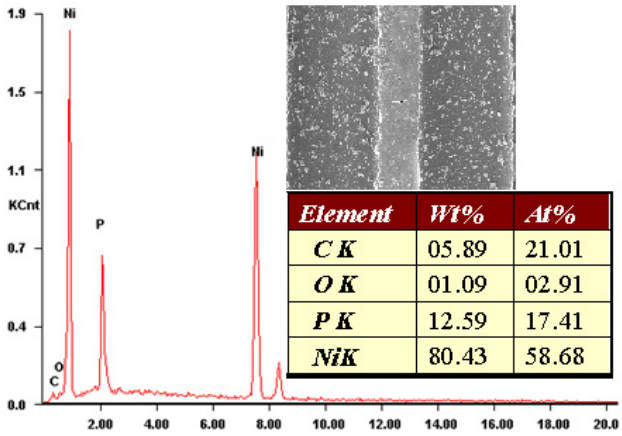

Fig.4.6 EDS of Ni-P films on 3D Si/SiO_2 structure.

Without pretreatment or the pretreatment is not good enough, continuous metallic layer cannot be obtained by electroless plating, such as that in Fig. 4.7.

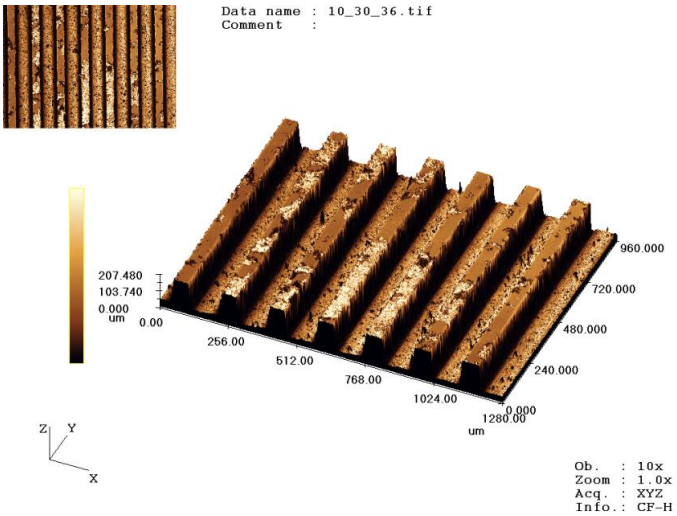

Fig. 4.7 Electroless plating result without enough sensitization and activation.

4.1.4 PPy electropolymerization

PPy electropolymerization on both the 3D and the planar Si/SiO_2/Ni samples were carried out. To reduce subsidiary reaction of nickel dissolving as discussed in chapter 3, two-step electropolymerizaiton method (8 $mAcm^{-2}$ current density for several seconds and then 0.5 $mAcm^{-2}$ current density for 30min) was used to deposit PPy films on both the 3D and planar Si/SiO_2/Ni samples. The preparation solution containing 0.3 M monomer Py and 0.3 M supporting TOSNa with pH values adjusted as 4.00 during polymerization by TOSH. Fig. 4.8 shows photograph of the 3D Si/SiO_2/Ni/PPy electrode. It can be seen that continuous PPy film are obtained. Fig. 4.9 presents the SEM microphotograph and EDS spectrum of the 3D Si/SiO_2/Ni/PPy electrode (after electrochemical testing). It was found that the ratio of Ni element in Ni-P alloy was reduced from 86.48 (100%-13.52%) to 78.29% (15.15/(15.15+4.20)). This may due to subsidiary reaction of nickel dissolving. It is also found that the morphology of PPy on the bottom surface of the 3D electrode is porous while relative flat PPy is observed on the top surface. This is because that inductively coupled plasma (ICP) made the bottom surface much rougher during DIRE the processing.

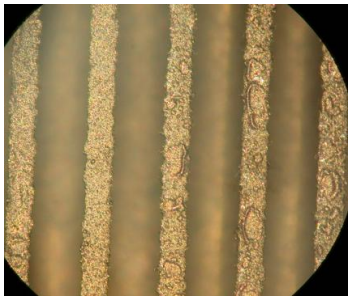

Fig. 4.8 Image of 3D Si/SiO_2/Ni/PPy electrode, 120 µm channels with 60 µm inter-channel spacing.

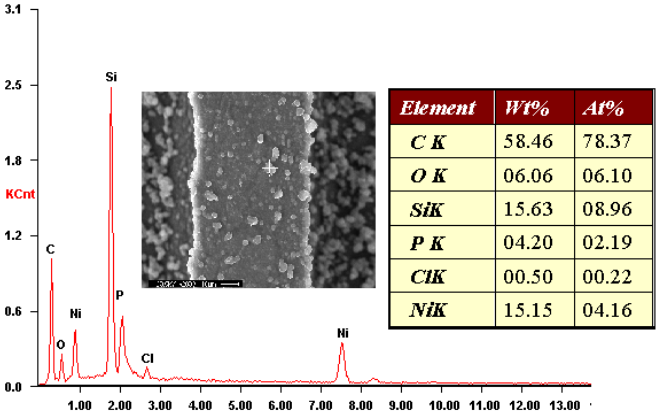

Element	Wt%	At%
C K	58.46	78.37
O K	06.06	06.10
SiK	15.63	08.96
P K	04.20	02.19
ClK	00.50	00.22
NiK	15.15	04.16

Fig. 4.9 SEM and EDS of 3D Si/SiO_2/Ni/PPy electrode after electrochemical testing.

4.1.5 Electrochemical characterizations

CV, EIS and GCD were used to investigate the supercapacitor properties of the 3D and planar electrodes. All the electrochemical tests were performed on Solartron 1260 in a three-electrode system with the Pt sheet as counter electrode and saturated calomel electrode (SCE) as reference electrode in 0.3 M $LiClO_4$ solution. All the potentials in the following text are referenced to SCE.

4.1.5.1 CV tests

The CV tests were carried out from -0.6 to 0.4 V with scan rates of 1, 5, 20, 50 and 100 mVs^{-1}. For clearly comparison, normalized current densities (i.e. faradic current divided by real surface area of the electrode) were used instead of currents as vertical axis in normalized CV plots. Fig. 4.10 presents the normalized CV curves of 3D and planar electrodes at 5 and 50 mVs^{-1}. It was found that the normalized CV curves for the 3D and

planar electrodes were almost overlapping at same scan rates. The capacitance could be calculated by integrating the current of a CV curve in discharge half cycle [37].As presented in Fig. 4.11, the normalized specific capacitances (i.e. capacitance divided by real surface area of electrode) of the 3D and planar electrodes are very close to each other at various scan rates, indicating homogeneous and continuous PPy film was deposited on 3D $Si/SiO_2/Ni$ structure. The degeneration of the capacitance is result from the decreasing quantity of active counter ions which caused by the increasing scan rate. At scan rate of 100 mVs^{-1}, the normalized specific capacitances of 0.014 and 0.013 Fcm^{-2} were obtained for the 3D and planar electrodes, respectively.

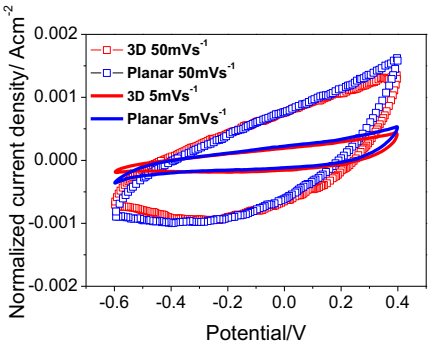

Fig. 4.10 Normalized CV curves of 3D and planar electrodes at 5 and 50 mVs^{-1}.

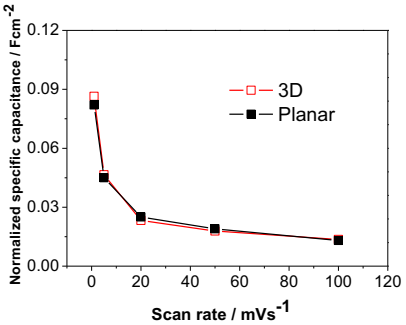

Fig. 4.11 Normalized specific capacitances at various scan rates for 3D and planar electrodes.

4.1.5.2 EIS tests

EIS data were acquired at open circuit potential over a frequency range between 0.01

Hz and 100 kHz and with potential amplitude of 10 mV. Fig. 4.12 presents Nyquist plots of the 3D and planar electrodes, which were well fitted by the equivalent circuit as shown in Fig. 4.13. In where, the R_s describes the resistance of solution and all the wires, R_{dl} refers to the resistance of charge transfer between electrolyte and PPy film. The constant phase element Q_{dl} represents the capacitance of double layer capacitor, produced by electrostatic attraction at the interface of electrolyte and electrode. The constant phase element Q_t is used to describe the diffusion process of counter ions in PPy films. According to the equivalent circuit, the depressed semi-circles at high frequencies in Fig. 4.11 correspond to the $R_{dl}Q_{dl}$ parallel combination, while Q_t performed as resister indicating that the ion diffusion cannot follow the electric field change at high frequencies. At low frequencies, the diffusion of charge in the PPy will dominate, resulting in the Warburg-like line. The magnitude of Q_t is considered as the capacitance of PPy. From the modeling results, the normalized specific capacitances of the 3D and planar electrodes were computed to be 0.011 and 0.0094 Fcm^{-2}, respectively.

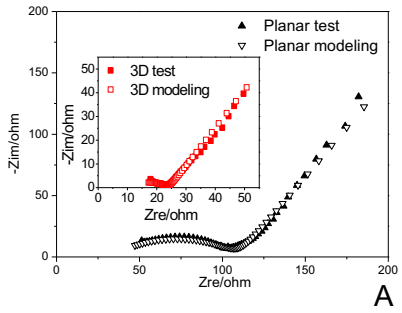

Fig. 4.12 Nyquist plots for the 3D and planar electrodes.

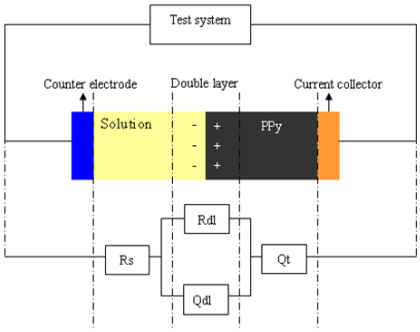

Fig. 4.13 Schematic drawing of EIS equivalent circuit and corresponding physical elements.

4.1.5.3 GCD tests

GCD curves of the 3D and planar electrodes were obtained under the potential from -0.6 V to 0.4 V at the normalized current densities of 0.2 - 7.75 mA/cm^2. Fig. 4.14 depicts the GCD curves of the 3D and planar electrodes at current density of 2 mAcm^{-2}. It is observed that the potential drops fast at range of 0.4 to 0.0 V, but the discharge curves keep linear with a small slope from 0.0 V to -0.6 V. The discharge capacitances of the 3D and planar electrodes can be calculated from the linear part of discharge curves. The normalized specific capacitances of the 3D and planar electrodes are shown in Fig. 4.15. The curves of the normalized specific capacitance versus the discharge current density are almost overlapping. At the discharge rate of 2 mAcm^{-2}, the specific capacitances of the 3D and planar electrodes are 0.011 and 0.010 Fcm^{-2}, respectively. It is also found that the normalized specific capacitance decrease with increasing current load, which is because the counter ions cannot be extracted from PPy film completely at large discharge rate.

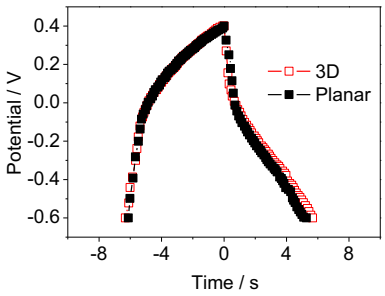

Fig. 4.14 GCD curves of the 3D and planar electrodes at 2 mAcm^{-2} normalized current density.

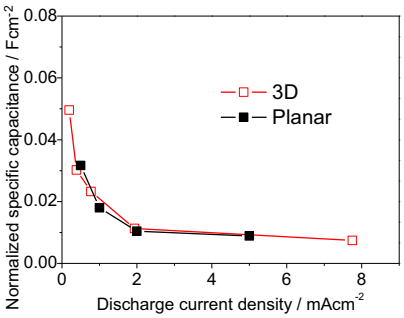

Fig. 4.15 Normalized specific capacitances at various current densities.

All the electrochemical tests proved that the 3D electrode performed like a planar electrode with 2.7 times footprint, which means the conformal depositions of nickel current collector and PPy film on 3D structures were successfully achieved without decreasing the capacitance properties of the PPy electroactive material.

Finishing the electrochemical tests, the 3D electrode was charged to doping state (0.4 V) and tested by SEM and EDS, as shown in Fig. 4.9. It is found that there is a weak peak for Cl element in the EDS spectrum. There is no Cl element in the as prepared $Si/SiO_2/Ni/PPy$ electrode. But due to the size of ClO_4^- is smaller than TOS^-, so ClO_4^- ions instead of TOS^- ions can take part in doping/undoping of PPy. Although larger capacitance of the 3D electrode by effective surface magnification is obtained, the electrochemical properties of the 3D electrode is also need to be improved. For instance, the CV curves should be improved with rectangle-like shape, which is ideal property of supercapacitor [38].

4.2 Optimization of 3D electrode for MEMS supercapacitors

As discussed above, the sizes of doping ions in as prepared PPy electrode and the ions in testing solution can affect the capacitance properties of 3D $Si/SiO_2/Ni/PPy$ electrode. The 3D electrode fabricated above presented non-ideal supercapacitor properties, this may be due to the size of ClO_4^- ion in testing solution is not small enough compare with TOS^- ions in as prepared PPy film. So, the properties of the 3D $Si/SiO_2/Ni/PPy$ electrode should

be improved by modifying the electropolymerizaiton, and developing proper electrolyte containing smaller inions, such as Cl^- inions.

4.2.1 Polymerization of PPy films

The PPy films were galvanostaticly prepared on the $Si/SiO_2/Ni$ 3D structures in aqueous solutions containing 0.1 M Py monomer and 0.5 M supporting salts ($LiClO_4$, NaCl, TOSNa), as well as organic solution (99% acetonitrile (AC) + 1%H_2O) containing 0.1 M Py and 0.1 M TOSH. The pH of each aqueous solution was adjusted at 4.00 by corresponding acid and alkaline (i.e. for supporting salts NaCl, HCl and NaOH were used to control the pH). A platinum sheet was used as cathode. The polymerizations were carried out at 20 ℃ and 1 $mAcm^{-2}$ current density for 30 min (after several seconds polymerization at 8 $mAcm^{-2}$ current density).

4.2.2. Electrochemical tests of 3D electrodes with different preparation conditions

3D $Si/SiO_2/Ni/PPy$ doping with Cl^-, ClO_4^- and TOS^- anions prepared in aqueous solutions (PPy_{Cl}, PPy_{ClO4} and PPy_{TOSAQ}), as well as PPy_{TOSAC} prepared in organic solution were successfully achieved as electrodes for supercapacitor. All the electrochemical tests were carried out in a three-electrode system 1M NaCl solution.

4.2.2.1 CV tests

The scan rates of CV tests ranged from 5mVs^{-1} to 500 mVs^{-1}, in which, 5 mVs^{-1}, 20 mVs^{-1}, 50 mVs^{-1}, and 100 mVs^{-1} was used to investigated the capacitance properties while 500 mVs^{-1} for cyclic performance testing. The potential windows for the four 3D electrodes were determined by the linear part of GCD curves, ranged from -1.0 V to -0.5 V for PPy_{ClO4}, from -0.7 V to -0.2 V for PPy_{Cl}, and from -0.6 V to 0.4 V for PPy_{TOSAQ} and PPy_{TOSAC}. Fig. 4.16 presents the CV curves at various scan rates from 5 mVs^{-1} to 100 mVs^{-1} for PPy_{Cl}, PPy_{ClO4}, PPy_{TOSAQ} and PPy_{TOSAC}, respectively. All the curves were obtained between the 5^{th} and the 20^{th} cycle to make sure the PPy films were activated but not degenerate. It is found that:

(a) The potential windows for PPy_{TOSAQ} and PPy_{TOSAC} are 1.0 V which is larger than that of PPy_{Cl} and PPy_{ClO4}. It is important to have higher potential window

U for supercapacitors because the energy and power can stored in the electrode are proportional with U^2.

(b) The Faradic currents for PPy_{TOSAC} are much smaller compare with PPy_{TOSAQ} at the same scan rate of CV tests. This is because PPy_{TOSAC} has much less porous structure compare with PPy_{TOSAQ} [93], the porous structure will result in higher capacitance properties. So, the PPy_{TOSAC} prepared in organic solution is not suitable for supercapacitors. The CV shapes of PPy_{TOSAQ} are better than PPy_{Cl} but not as good as PPy_{ClO4}.

(c) The maximum current value for PPy_{Cl} is larger in relative narrow range compare to PPy_{ClO4} at the same scan rate, but the shape of CV curves for PPy_{Cl} is non-ideal, while the CV curves for PPy_{ClO4} were rectangle-like, which is the characteristic of electrochemical capacitors. The size of Cl^- is smaller than ClO_4^-, so Cl^- in testing solution can easily replace ClO_4^- to insert into and eject from the PPy matrix during cycling. Therefore PPy_{ClO4} present batter supercapacitor properties than PPy_{Cl} in NaCl solution.

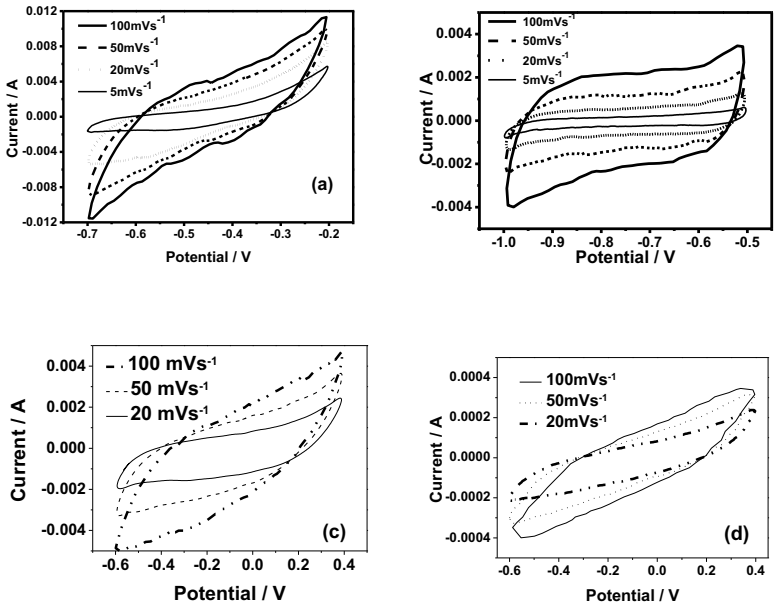

Fig.4.16 CV curves of 3D $Si/SiO_2/Ni/PPy$ electrode prepared with different conditions and test in NaCl solutions, (a) PPy_{Cl}, (b) PPy_{ClO4}, (c) PPy_{TOSAQ} and (d) PPy_{TOSAC}.

The quantitative capacitance can be calculated by integrating the current of a CV curve in discharge half cycle. For an electrode of supercapacitor with rectangle-like CV shape (current is almost a constant), it can also be approximately calculated by Eq. 4.4,

$$C = Q/U = I \times \Delta t / U = I/(U/t) = I/S \tag{4.4}$$

where I is the average current for each half cycle, S is the scan rate of each CV curve, C is specific capacitance and Δt is the discharge time. Fig. 4.17 presents the specific capacitances and specific powers for PPy_{ClO4} and PPy_{TOSAQ} at various scan rates of from 5 mVs^{-1} to 500 mVs^{-1}. With increasing scan rate, the specific capacitance dropped quickly for PPy_{TOSAQ} than that of PPy_{ClO4}. But the PPy_{TOSAQ} provide larger specific power due to its larger potential window.

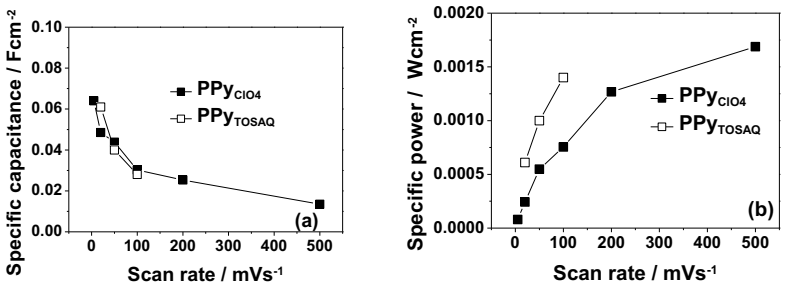

Fig. 4.17 Specific capacitances (a) and specific powers (b) for PPy_{ClO4} and PPy_{TOSAQ} at various scan rates.

CV method was also used to characterize the cyclic behavior of PPy_{ClO4}. The reactive current as a function of cycle number is given in Fig. 4.18. It is observed that the reactive current didn't decrease apparently even increase cycle number to more than 800 times with the CV scan rate 500 mVs^{-1}. CV curves at scan rate of 50 mVs^{-1} before and after long time cycling are present in Fig. 4.19. It is found that the two CV curves are almost overlapping, which implied that there is no specific capacitance degenerated after 800 cycles. The PPy_{ClO4} presented quite stable cyclic behavior.

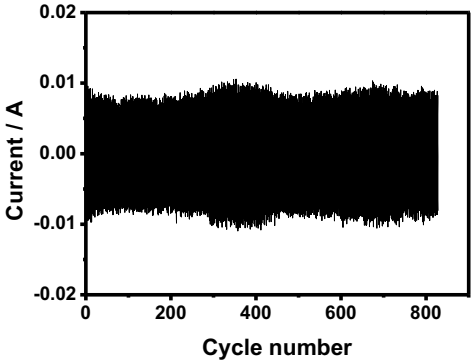

Fig. 4.18 Reactive current versus cycle number.

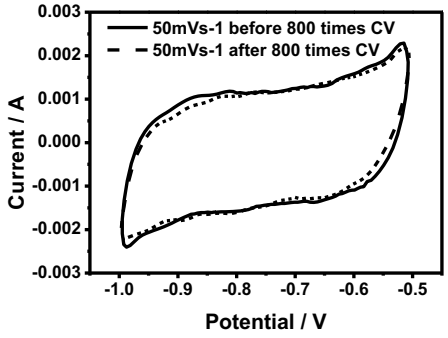

Fig. 4.19 CV curves of PPy_{ClO4} before and after 800 cycles at 50mVs^{-1} scan rate.

4.2.2.2 EIS tests

The 3D electrodes PPy_{Cl}, PPy_{ClO4}, PPy_{TOSAQ} and PPy_{TOSAC}, were also investigated by EIS test over a frequency range from 0.01 Hz to 100 kHz and with potential amplitude of 10 mV. Fig. 4.20 presents the Nyquist plots of PPy_{Cl}, PPy_{ClO4}, PPy_{TOSAQ} and PPy_{TOSAC} (after cycling) at OCP. The EIS data can be well fitted by equivalent circuit as shown in Fig. 4.21. In which R_1 means the resistance of solution and wires, R_2 characterizes the charge transfer resistance between the interface of the test solution and electrodes, CPE_1 and CPE_2 instead of capacitors to describe the double layer capacitance at the interface, and the pseudo capacitance from ions transfer in the PPy matrix. It is found that R_1 for PPy_{TOSAC} is bigger than that of the others. I believe this is due to the bad contact at the interface of Ni and PPy, resulting from organic preparation solution. The fitting results

showed that the value of CPE_2 for each electrode is much larger than corresponding CPE_1, implying pseudocapacitance dominates the capacitance of the electrodes. The specific capacitances obtained from EIS fitting results are 0.006, 0.042, 0.023 and 0.018 Fcm^{-2} for PPy_{TOSAC}, PPy_{TOSAQ}, PPy_{ClO4}, and PPy_{Cl}, respectively. Fig. 4.22 presents the Bode plots [94] of PPy_{Cl}, PPy_{ClO4}, PPy_{TOSAQ} and PPy_{TOSAC}. It can be seen that the phase angle for each electrode is almost zero at high frequency region high than 1000 Hz, which means the electrodes behave like a resistor at that region. While with the frequency decreasing, the phase angles shift to negative 90 degree. Among them, PPy_{ClO4} presents the best supercapacitor properties with the phase angle about -60 degree at frequency of 0.01 Hz.

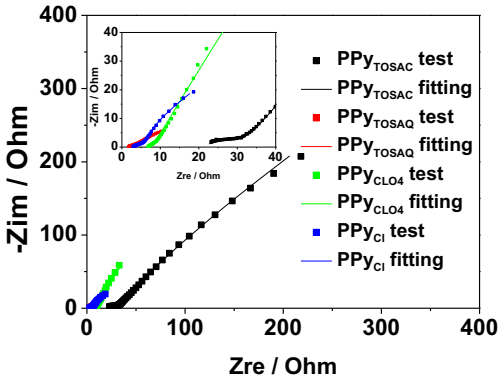

Fig. 4.20 Nyquist plots of PPy_{Cl}, PPy_{ClO4}, PPy_{TOSAQ} and PPy_{TOSAC} at OCP.

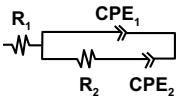

Fig. 4.21 Equivalent circuit for fitting EIS.

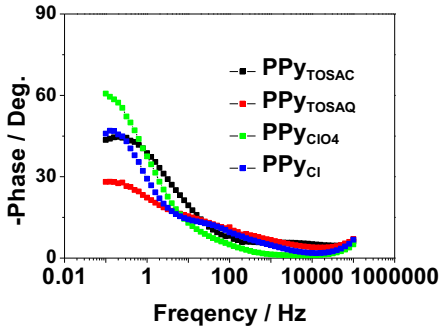

Fig. 4.22 Bode plots of PPy_{Cl}, PPy_{ClO4}, PPy_{TOSAQ} and PPy_{TOSAC}.

Because the 3D electrodes can have many states, such as, as prepared, doping, undoping and partly doping states, the different states may result in different properties of the electrodes. EIS tests were also used to investigate the properties of the PPy_{ClO4} electrode at different states. Before any CV tests, the Nyquist plot of PPy_{ClO4} at OCP is shown as insert in Fig. 4.23, a decline line were observed at low frequency area. The angles between the decline lines and the real axes are large than 45^{o} and lower than 90^{o}, corresponding the ion diffusion mechanism between Warburg diffusion and ideal capacitive ion diffusion. Fig. 4.23 also presents the Nyquist plots of PPy_{ClO4} electrode at OCP, -1.0 V (undoping state) and -0.5 V (doping state) after 800 times cycling. It is found the decline lines at low frequencies for OCP, doping and undoping states are close, implying all the three states of the PPy_{ClO4} electrode present the similar specific capacitances. Fig. 4.24 (a) and (b) present the modeling curves of the Nyquist plots of PPy_{ClO4} obtained in NaCl solution before and after long time cycling at OCP. From the modeling results, the specific capacitance of the PPy_{ClO4} is 0.004 Fcm^{-2} before long time cycling, which is far less than 0.023 Fcm^{-2}, the value that is obtained after 800 times CV cycling. This is because before long time cycling, the ClO_4^- ions were the active ions, however, the Cl^- ions replace the ClO_4^- to dope and undope during long time cycling.

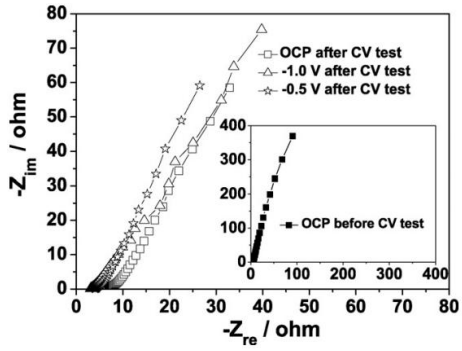

Fig. 4.23 Nyquists plots of PPy_{ClO4} at different potentials.

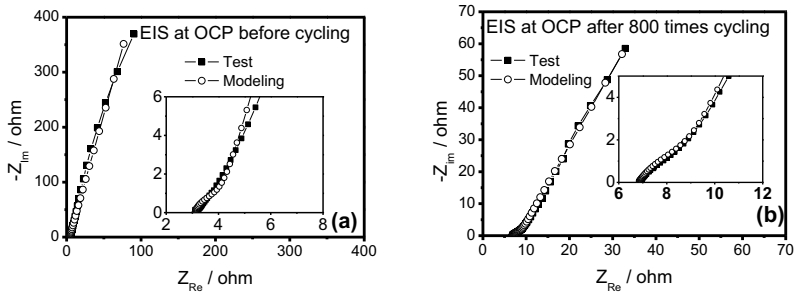

Fig. 4.24 Nyquist plots of PPy_{ClO4} at OCP, (a) before cycling, (b) after cycling.

4.2.2.3 GCD tests

GCD technique was used to characterize the supercapacitor performances of PPy_{Cl}, PPy_{ClO4}, PPy_{TOSAQ} and PPy_{TOSAC} electrodes. The data were obtained from -0.6 to 0.4 V for PPy_{TOSAC} electrode, from -0.6 to 0.3 V for PPy_{TOSAQ} electrode, from -1.0 to -0.5 V for PPy_{ClO4} electrode and from -0.7 to -0.2 V for PPy_{Cl} electrode. The charge/discharge curves are shown in Fig. 4.25. It is found the GCD curves of PPy_{ClO4} electrode are almost linear in the whole potential range at various current rates, which indicates that the electrode has good supercapacitor properties. The discharge specific capacitance C_d of PPy_{ClO4} can be calculated as 0.011, 0.027 and 0.070 Fcm^{-2} at 2, 1 and 0.5 $mAcm^{-2}$ discharge current densities, respectively. For the other electrodes, the GCD curves are some bending, especially charging with small current densities. This implied that it is difficult to keep the electrodes with very high doping state, i.e. unstable at charging state. At the same charge/discharge current density of 1 $mAcm^2$, PPy_{TOSAQ} has the longest charge/discharge

time, which means it can store more energy even it is not the one has the best supercapacitor properties.

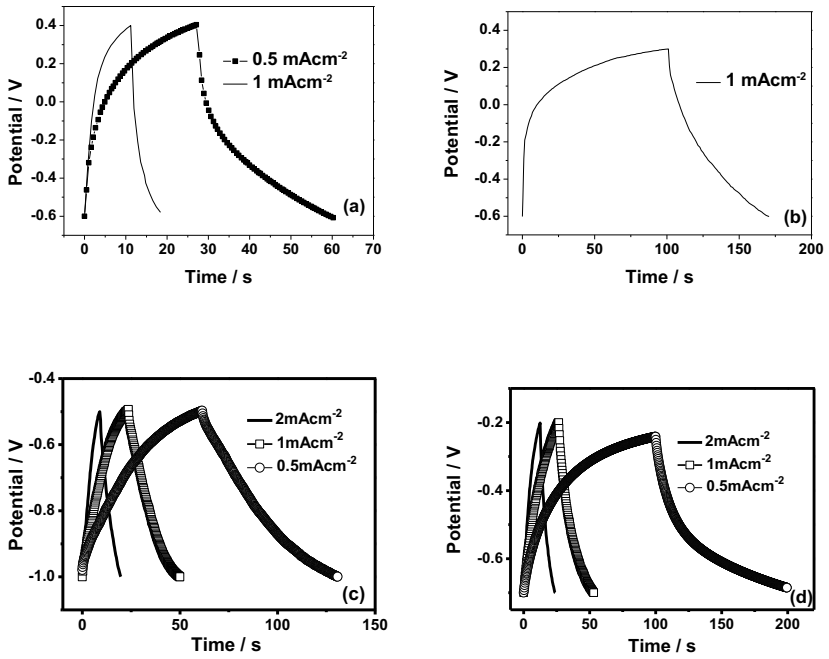

Fig. 4.25 GCD curves, (a) PPy_{TOSAC}, (b) PPy_{TOSAQ}, (c) PPy_{ClO4}, (d) PPy_{Cl}.

The electrodes of PPy_{Cl}, PPy_{ClO4}, PPy_{TOSAQ} and PPy_{TOSAC} for supercapacitors present different properties in NaCl solution. PPy_{TOSAC} is the worst one because the flat structure resulted from organic preparation solution. PPy_{ClO4} electrode performed almost ideal supercapacitor properties with the potential window from -1.0 to -0.5 V. PPy_{TOSAQ} has advantage of wide potential range from -0.6 to 0.4 V thus can store more energy and provide more power.

For the realistic application of supercapacitors, it is a big advantage to have high operating voltage. So, I adapt PPy_{TOSAQ}-in-NaCl system to fabricate 3D MEMS supercapacitors based on DRIE technology.

4.3 3D MEMS supercapacitors based on DRIE technology

Electroless nickel plating has been used for metallization of Si/SiO_2 3D structure. Polymerization on nickel current collector will be accompanied with subsidiary reaction, which has bad influence on the properties of Si/SiO_2/Ni/ PPy electrodes. To avoid the subsidiary reaction, another current collector sputtered Ti is used for PPy deposition.

In this part, a 3D symmetric MEMS supercapacitor by MEMS technologies is designed and fabricated. The key fabrication processes include DRIE for "through-structure" etching, thermal oxidation for SiO_2 growing, twp-step RF sputtering for Ti current collectors depositing and electrochemical polymerization for PPy synthesis. The supercapacitor behaviors of the PPy electrodes and the symmetric MEMS supercapacitor were investigated by electrochemical tests.

4.3.1 Design of fabrication process flow

As designed in chapter 2, the DRIE based 3D MEMS supercapacitor has 3D "through-structure", which include two disconnected periodic beams surrounding by PPy films served as anode and cathode. The process flow for fabricating the supercapacitor is designed in Fig. 4.26.

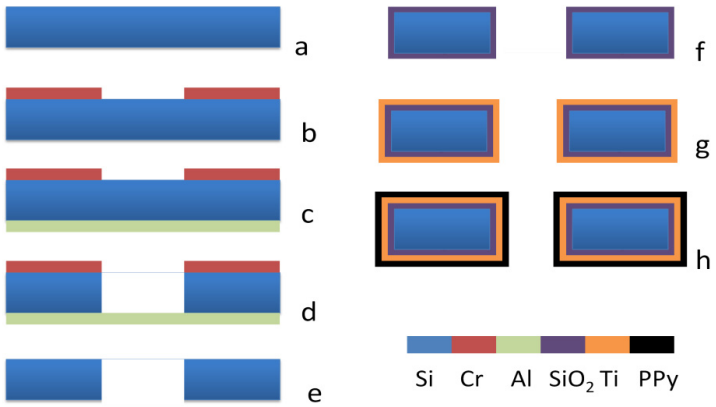

Fig. 4.26 Process flow for fabricating 3D MEMS supercapacitor. (a) Silicon wafer, (b) Cr mask deposition and patterning, (c) Al back-side deposition, (d) DRIE through the

whole thickness of Si wafer, (e) Metal layers removal, (f) Thermal oxidation, (g) Ti current collectors sputtering, (h) PPy electrodes eletropolymerization.

Fig. 4.27 shows the protection mask design for DRIE by L-edit. During the two-step RF sputtering, the sputtered Ti film will be deposit on both the top surface and the side surface of the 3D Si/SiO_2 structures. So, we design the single cell of the mask with two "ears" to separate anode and cathode after Ti sputtering.

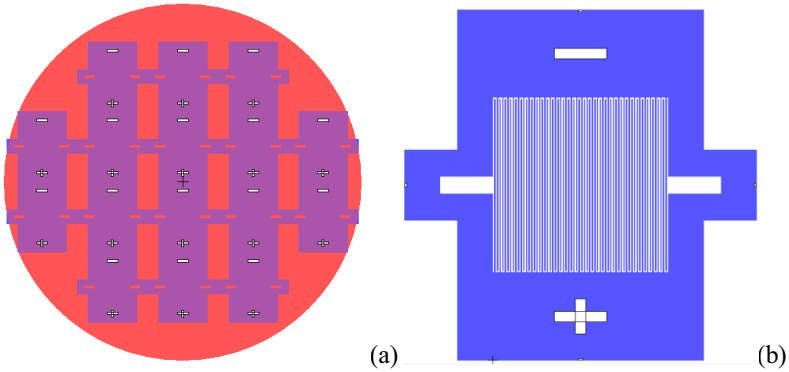

Fig. 4.27 Mask design, (a) 4 inch wafer mask, (b) single cell.

4.3.2 Fabrication of 3D MEMS supercapacitors based on DRIE technology

4.3.2.1 Structuring silicon substrate

Because etching through the whole 525 μm thickness of the silicon substrate is time consuming, patterned Cr layer was used as the DRIE protection mask. Al layer on the back side of the Si wafer serves as DRIE stop layer, as shown in Fig. 4.26. Fig. 4.28 presents the photo of the substrate after Cr protection layer patterning.

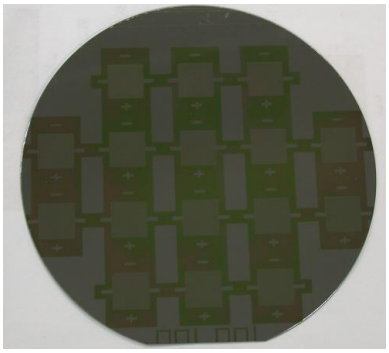
(a)
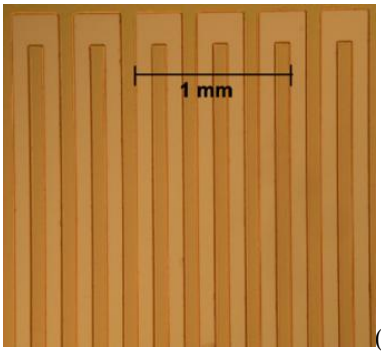

(b)

Fig. 4.28 Photos after Cr patterning (photoresist was not removed), (a) the whole wafer; (b) part of single cell

The key step DRIE was carried out on AMS200 (Alcatel, France) by using alternating SF_6 and C_4F_8 as etching gas and passivation gas respectively. I achieved an about 7 $\mu m min^{-1}$ etching speed in the first 30 minutes, then "black silicon" [95] with the grass-like structure occurred on the bottom of the being etched channel. Fig. 4.29 shows the morphology of the "black silicon", it can be seen that the length of the "grasses" is at the level of hundreds of micrometers. The "black silicon" is resulted from the different width of etching areas. In area with big width, the amount of heat produced and cannot dissipate immediately, and then temperature difference occurred on the substrate. In the area with small width, the organic passivation residue cannot be removed completely for next etching cycle. The "black silicon" can be eliminated by changing the composite of etching gas, but the etching speed became slower significantly, the total DRIE time is 210 minutes.

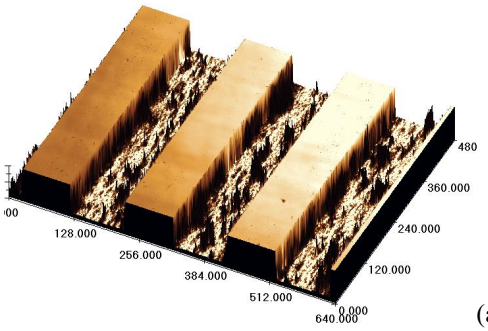

(a)
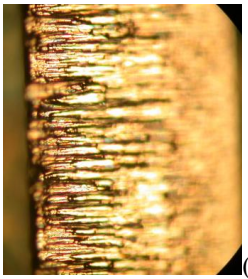
(b)

Fig. 4.29 Morphology of "black silicon", (a) top view, (b) side view.

It is well known that the lag effect always accompany with DRIE when the width difference of etching area exists [96]. In the experiment, when the area with big width is

etched through the whole substrate, there is still 68 μm thick silicon remaining at the area with small width. The lag effect is about 12.95% (as shown in Fig. 4.30).

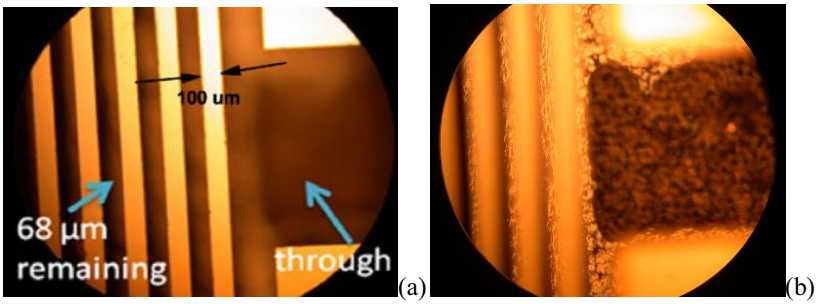

Fig. 4.30 Lag effect of DRIE, (a) focus on top, (b) focus on bottom.

To etch the remaining thickness of the substrate, an isotropic wet etching solution $HF/HNO_3/HAc$ was used after removing the metal layers of Cr and Al. The $HF/HNO_3/HAc$ solution can also reduce the stress at edges and coarsen the surface of all effective surfaces, as shown in Fig. 4.31. Fig. 4.32 gives the photo of micro fabricated 3D structure taken by Olympus OLS1200 laser scanning confocal microscope.

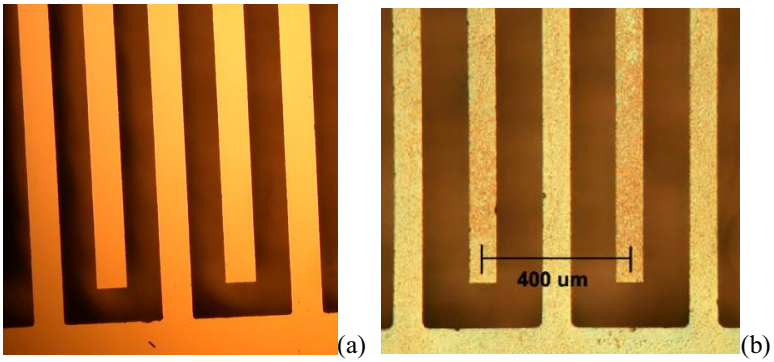

Fig. 4.31 Image of 3D Si structure, (a) before coarsening, (b) after coarsening.

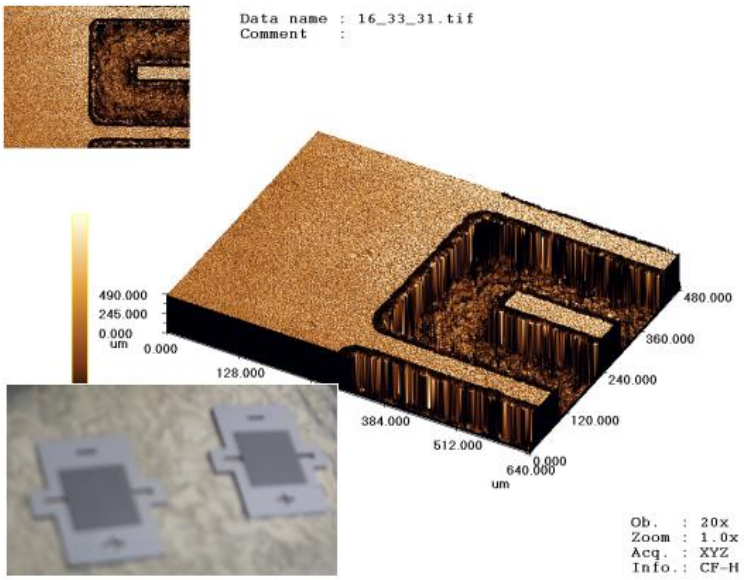

(e)

Fig. 4.32 Image of microfabricated 3D “through structure” by Olympus OLS1200 laser scanning confocal microscope.

To avoid “black silicon” and Lag effect, the protection mask for DRIE should have similar width of etching area. The optimized design of mask is shown in Fig. 4.33.

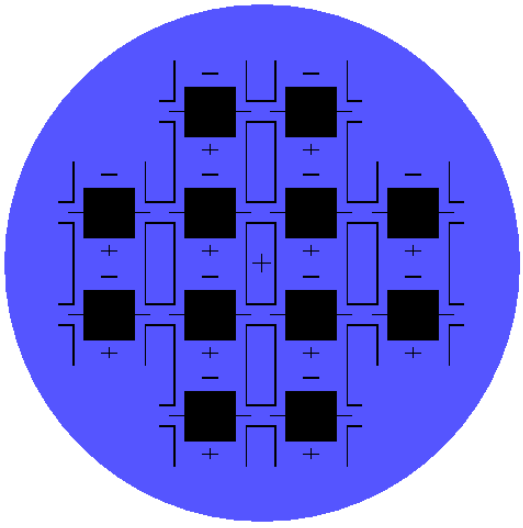

Fig. 4.33 Optimized design for DRIE mask.

4.3.2.2 Current collectors

After DRIE, a layer of thermal oxidized SiO_2 with the thickness of 1.5 μm formed on

all the effective surfaces of the 3D structure as insulator. Then continuous Ti layer on all the tops, bottoms and side walls of the substrate was deposited by two-step sputtering (front and back sides). The substrate was rotated at the rate of 20 rpm during the sputtering process. Finally, the Ti layer was divided into anodic and cathodic current collectors by etching the supporting frame.

4.3.2.3 Electroactive electrodes

Electroactive PPy films were electrochemical polymerized on current collectors as the electrodes of supercapacitor. The electrochemical polymerizations for single electrodes were carried out at 20 ℃ under constant 0.8 V voltage for 5~20 minutes in a electrolytic bath with stirring, which containing 0.5M Py monomer and 0.3 M TOSNa as surfactant and supporting salt, additional TOSH acid was used to adjust the pH of the solution as 4.00. Py were purified by vacuum distillation prior to use, analytical reagent TOSNa and TOSH were obtained from commercial sources and used as received.

4.3.3 Electrochemical testing

As discussed above, NaCl solution is suitable as electrolyte for supercapacitor with PPy electrodes. To make a clear comparison, TOSNa and NaCl electrolytes with pH 4.00 were used for investigating the electrochemical performance of the 3D symmetric redox MEMS supercapacitor. Electrochemical tests were carried for single PPy electrode and the 3D MEMS supercapacitors in three-electrode system and two-electrode system. In three-electrode system, each PPy electrode was used as working electrode, a platinum sheet as counter electrode, and SCE as reference electrode. In two-electrode system, the two PPy electrodes served as the working electrode and the counter electrode respectively.

For each PPy electrode and the supercapacitor, CV tests of were carried out with the scan rates ranged from 10 mVs^{-1} to 100 mVs^{-1}. The specific charge capacitance C_c and discharge capacitance C_d can be calculated by integrating the current of the CV curve in the half charge cycle and half discharge cycle, respectively. EIS tests were performed from100 kHz frequency to 0.01 Hz frequency with the potential amplitude of 10 mV, the specific capacitance can be obtained by fitting the EIS data with a suitable equivalent circuit on the software which is attached to electrochemical workstation. GCD curves were

obtained at the current density from 0.5 $mAcm^{-2}$ to $5mAcm^{-2}$, the discharge capacitance C_d can be calculated from the linear part of discharge curve. The specific power P of the PPy electrode or the supercapacitor can also be calculated from CV and galvanostatical discharge curves as mentioned above.

4.3.3.1 Effect of electrolytes

0.5 M NaCl solution and TOSNa solution both adjusted to pH 4.00 were used as test electrolytes for single PPy electrode (10 minutes polymerization) in three-electrode system. The electrochemical behaviors of PPy electrode are shown in Fig. 4.34.

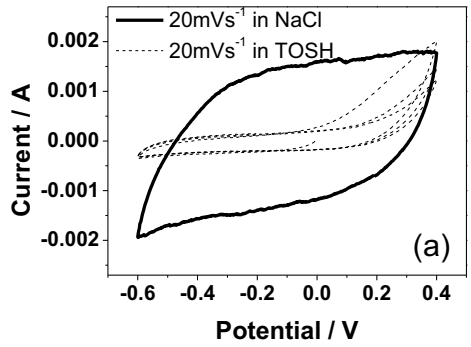

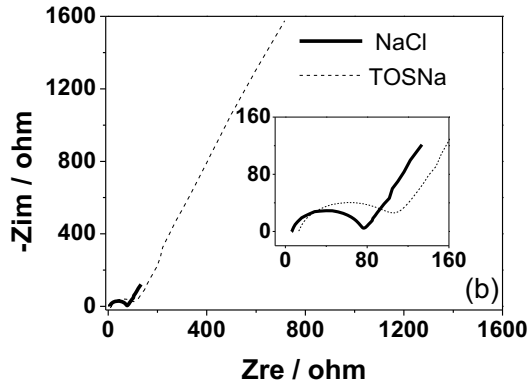

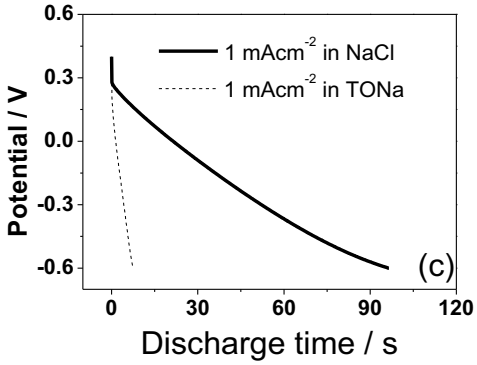

Fig. 4.34 Electrochemical behaviors of single PPy electrode in NaCl electrolyte and TOSNa electrolyte. (a) CV tests at scan rate of 20 mVs^{-1}, (b) EIS tests at open circuit potential, (c) Galvanostatical charge/discharge tests at discharge rate of 1 $mAcm^{-2}$.

CV tests of the single PPy electrode were carried out with potential ranged from -0.6 V to 0.4 V at scan rate of 20 mVs^{-1}, which are given in Fig. 4.34(a). In TOSNa electrolyte, the CV curve presents non-ideal capacitance character. In which the reactive current is small below 0.2 V, but increase dramatically at 0.2 V at charging in TOSNa electrolyte. This means the TOS^- can go into very deep area of the PPy film only at charging potential up to 0.2 V. While in NaCl electrolyte, the PPy electrode performed ideal capacitance property with rectangle-like shape and higher reactive current. This is because Cl^- has so smaller size and faster ionic mobility in comparison to TOS^- that can transfer into very deep area of the PPy film at the whole test potential range.

EIS curves of the single PPy electrodes were obtained at open circuit potential, as shown in Fig. 4.34(b). The EIS data can be fitted by the same equivalent circuit shown in Fig. 4.21, In high frequency area, depressed semi-circles are observed implying electrostatic absorption mechanisms at the interfaces between electrolytes and PPy electrodes (electric double layer capacitance), because of the roughness of the electrodes, there is some dispersion of the double layer capacitance and thus the depressed semi-circles can be better fitted by using CPE_1. While in low frequency area, decline lines were observed on impedances, the angles between the decline lines and the real axes are large than 45^o and lower than 90^o, corresponding the ion diffusion mechanism between Warburg diffusion

and ideal capacitive ion diffusion (pseudo capacitance), CPE_2 was used for presenting the ions transfer processes to get better fitting results because the thickness of the PPy electrodes is not homogenous in micro scale. The minus imaginary part ($-Z_{im}$) of the EIS curve for PPy electrode in NaCl electrolyte is much smaller than that in TOSNa electrolyte, and it is well known that the value of pseudo capacitance is in direct proportion to $(-Z_{im})^{-1}$, so the PPy electrode presented higher pseudo specific capacitance NaCl electrolyte compare to that in TOSNa electrolyte.

The galvanostatical discharge tests for the single PPy electrode are shown in Fig. 4.34(c), with the potential range from -0.6 to 0.4 V at the current density of $1 mAcm^{-2}$. It is observed that the discharge time in NaCl electrolyte is much larger than that in TOSNa electrolyte, which means the single PPy electrode can store much more energy with NaCl electrolyte than TOSNa electrolyte.

The specific capacitances and specific powers calculated from CV, EIS and galvanostatical discharge tests are given in Table 4.1. Obviously, PPy electrode in NaCl electrolyte presents much larger specific capacitance than in TOSNa electrolyte for the all three test methods. The capacitance of PPy actually comes from the reversible p-type doping and undoping of anions. The PPy electrode as prepared is doped with TOS^- and different reactions happened in NaCl electrolyte and TOSNa electrolyte by the following formulas.

$$PPy^+TOS^- + e \rightarrow PPy + TOS^- \tag{4.4}$$

$$PPy + TOS^- - e \rightarrow PPy^+TOS^- \tag{4.5}$$

$$PPy + Cl^- - e \rightarrow PPy^+Cl^- \tag{4.6}$$

$$PPy^+Cl^- + e \rightarrow PPy + Cl^- \tag{4.7}$$

In TOSNa electrolyte, Eq. 4.4 and Eq. 4.5 occurred during discharging and charging. In NaCl electrolyte, Eq.4.4 occurred at the first discharge half cycle, but the Cl^- took the place of the TOS^- in the next charge and discharge due to its larger concentration and smaller size, as shown in Eq 4.6 and 4.7. Due to the smaller size and faster ionic mobility of Cl^- in comparison to TOS^-, Cl^- can go into very deep area of the PPy film easily through the

"path" formed by TOS^- unpoding, thus the PPy electrode presents batter capacitance behaviors in NaCl electrolyte, with the specific capacitance values much larger than that in TOSNa electrolyte, as shown in table 4.1. The PPy electrode in NaCl electrolyte presented also much larger specific power than that in TOSNa electrolyte from the calculation of CV tests. But due to the discharge time in TOSNa electrolyte is only 7.55 s, the specific powers of PPy electrode calculated from galvanostatical discharge tests are the same in both electrolytes. The values in table 4.1 implied that NaCl electrolyte is suitable for the PPy as electrode of supercapacitor.

Table 4.1. Specific capacitance and power from CV (20 mVs^{-1}), EIS and galvanostatical discharge (1 $mAcm^{-2}$).

Electrolyte	NaCl			TOSNa		
Test method	CV	EIS	Galvanostatical discharge	CV	EIS	Galvanostatical discharge
Specific capacitance (Fcm^{-2})	0.079	0.060	0.096	0.011	0.006	0.008
Specific power ($mWcm^{-2}$)	0.79		0.50	0.11		0.50

4.3.3.2 Effect of polymerization time

Single PPy electrodes polymerized for 5, 10 and 20 minutes were electrochemical investigated by CV and galvanostatical discharge methods with three-electrode system in NaCl electrolyte. Fig. 4.35(a) and Fig. 4.35(b) present the CV and galvanostatical discharge curves of PPy electrodes at scan rate of 20 mVs^{-1} and current density of 1 $mAcm^{-2}$, respectively. With the increasing polymerization time, the reactive currents of CV curves and the discharge time of galvanostatical discharge curves increase almost proportionally, which correspond the linearly relationship between the calculated specific capacitance and polymerization time, as shown in Fig. 4.35(c).

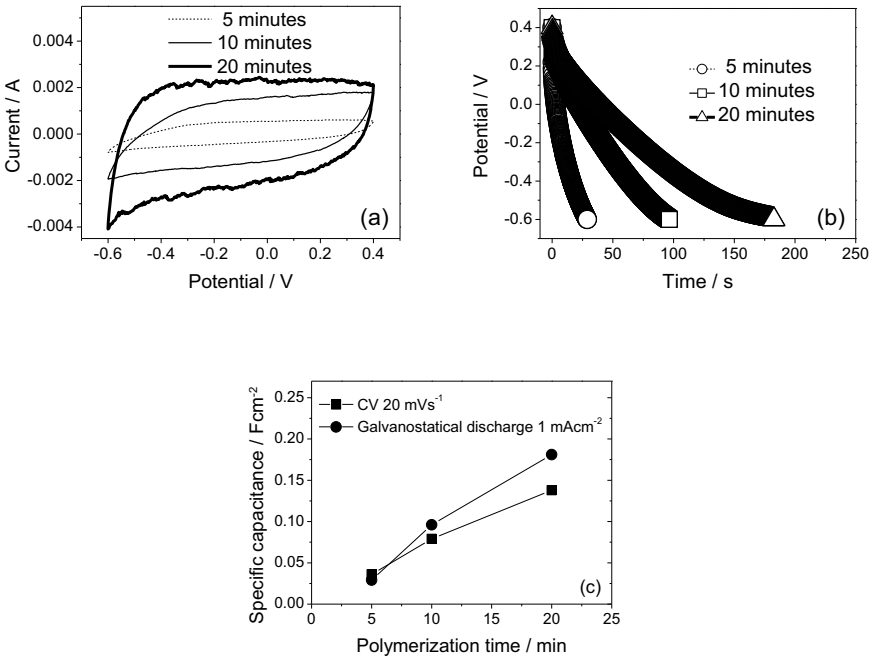

Fig. 4.35 Electrochemical behavior of single PPy electrodes with various polymerization time. (a) CV at scan rate of 20 mVs^{-1}, (b) Galvanostatical discharge curve at current density of 1 $mAcm^{-2}$, (c) Specific capacitances versus polymerization time.

The PPy electrodes polymerized for 5, 10 and 20 minutes were also tested with various scan rates from 5 to 100 mVs^{-1}. The specific capacitances at different scan rates are shown in Fig. 4.36(a). Besides the linear relationship between specific capacitance and polymerization time, it is found that the specific capacitance decreased rapidly with scan rate increasing from 5 to 20 mVs^{-1}, but slowly with scan rate increasing from 20 to 100 mVs^{-1} for each PPy electrode. This is because that at fast scan rate, the charge diffusion cannot follow the change of electric field, which gives rise to smaller specific capacitance, while at slow scan rate, ion doping/undoping is finished completely over long time, resulting in large capacitance. The specific powers at different scan rates are shown in Fig. 4.36(b). It is obviously that the specific power increase with both increasing polymerization time and scan rate. When the PPy electrode polymerized for 20 minutes is cycled with CV scan rate of 100 mVs^{-1}, the highest specific power value is 4.05 $mWcm^{-2}$,

meanwhile the specific capacitance value is 0.081 Fcm^{-2}.

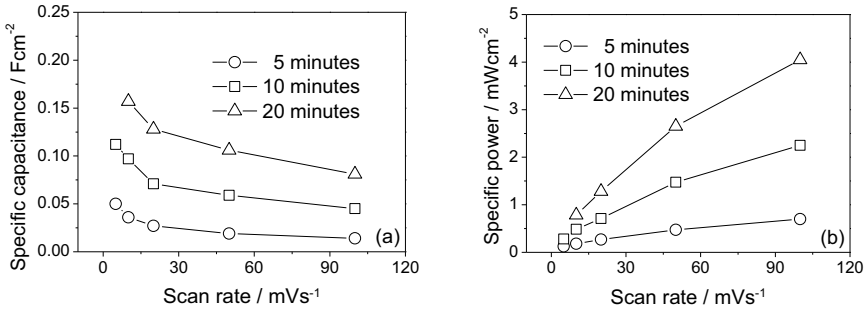

Fig. 4.36 (a) Specific capacitances and (b) specific powers of single PPy electrodes polymerized for 5, 10 and 20 minutes at various scan rate from 5 to 100 mVs^{-1}.

4.3.3.3 Performance of supercapacitor in one chip

The symmetric supercapacitor consisted of two PPy electrodes polymerized for 20 minutes was test with two-electrode system in NaCl electrolyte. One PPy electrode served as working electrode and the other electrode is counter electrode. Fig. 4.37 presents the CV curve of the supercapacitor with the potential range from -1.0 V to 1.0 V at the scan rate of 20 mVs^{-1}. The rectangle shape of the curve shows obviously ideal supercapacitor performance. In realized applications, the symmetric supercapacitor can be charged on both PPy electrodes without any difference. By the crossed lines of zero potential and zero current, the CV curve was divided into two charge parts and two discharge parts which are shown in Fig. 4.37. The charge or discharge capacitances can be calculated by integrating the current of the CV curve in one fourth of the cycle. The average specific charge and discharge capacitances of the symmetric supercapacitor are 0.085 Fcm^{-2} and 0.056 Fcm^{-2}. Theoretically, the capacitance of the symmetric supercapacitor should be equal to the capacitance of the two PPy electrodes connected in series, i.e. half of the capacitance of single PPy electrode. In here, the value of 0.056 Fcm^{-2} is lightly small than that half of the specific capacitance of one PPy electrode 0.064 Fcm^{-2} (0.5*0.128, in Fig. 4.36(a)). The specific discharge power of the supercapacitor is calculated as 0.56 $mWcm^{-2}$. GCD curve of the symmetric supercapacitor at current density of 5 $mAcm^{-2}$ with the potential ranged from -1.0 to 1.0 V is shown in Fig. 4.38. Both charge and discharge lines are almost linear,

which means good capacitance property of the symmetric supercapacitor. One charge/discharge cycle can also be divided into four parts, corresponding the charging and discharging of working electrode and counter electrode respectively, as shown in Fig. 4.38.

Compare to the LIGA-like based 3D MEMS supercapacitor, the DRIE based 3D MEMS supercapacitor is more ideal and provide higher specific capacitance and specific power. This is because solid state electrolyte used in LIGA-like based 3D MEMS supercapacitor limit the ions diffusion. The advantage of LIGA-like based 3D MEMS supercapacitor is that the supercapacitor is all-solid-state. Both the two types of 3D MEMS supercapacitors are provide more specific capacitance than earlier work in literatures [33, 35,38]. For instance, the specific capacitance of the DRIE based 3D MEMS supercapacitor (0.056 F cm^{-2}) is 28 times larger than that of PPy planar MEMS supercapacitor in literature [33], which presented specific capacitance of about 0.002 Fcm^{-2} (calculated from CV).

In addition, an asymmetric supercapacitor is configured with two PPy electrodes polymerized for 5 and 20 minutes, respectively. The CV curves at 20 mVs^{-1} scan rate in NaCl electrolyte are shown in Fig. 4.39.

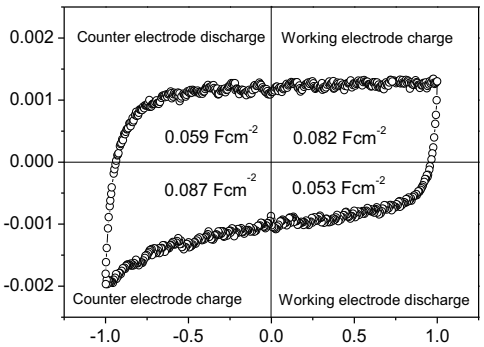

Fig. 4.37 CV of the symmetric supercapacitor with two PPy electrodes polymerized for 20 minutes.

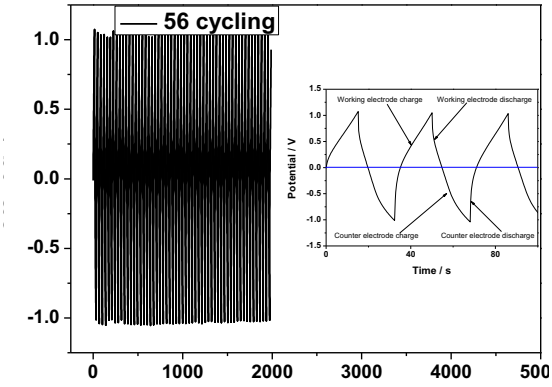

Fig. 4.38 Galvanostatical charge/discharge curve of the symmetric supercapacitor.

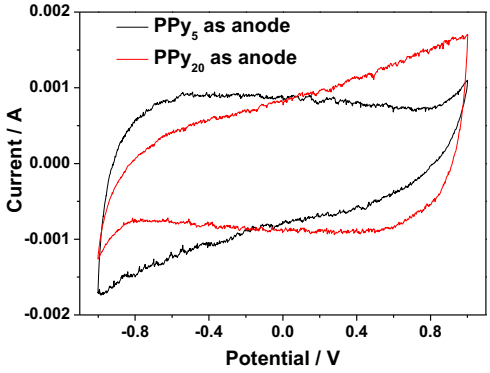

Fig. 4.39 CV of the asymmetric supercapacitor with two PPy electrodes polymerized for 5 and 20 minutes, respectively.

4.4 Chapter conclusions

In this chapter, DRIE technology had been used for fabricating 3D MEMS supercapacitors. At first, a Si/SiO_2/Ni/PPy electrode for MEMS supercapacitors with 3D structure was successfully fabricated. Compared to planar electrode, the 3D Si/SiO_2/Ni/PPy electrode presented almost the same normalized specific capacitance and power, which implied the continuous nickel and PPy layers were achieved. Then, to optimize the PPy polymerization, PPy_{Cl}, PPy_{ClO4}, PPy_{TOSAQ} and PPy_{TOSAC} as electrodes for supercapacitors were prepared. The electrochemical tests showed that PPy_{TOSAC} was the worst one because the flat structure resulted from organic preparation solution; PPy_{ClO4}

electrode performed almost ideal supercapacitor properties with the potential window from -1.0 to -0.5 V; PPy_{TOSAQ} had advantage of wide potential range from -0.6 to 0.4 V thus could store more energy and provide more power. Finally, PPy_{TOSAQ}-in-NaCl system was adapted to fabricate 3D MEMS supercapacitors based on DRIE tehnology, in which two-step sputtered Ti was used as the current collectors. In NaCl electrolyte, the single PPy electrodes of the 3D MEMS supercapacitor presented 0.128 Fcm^{-2} specific capacitance and 1.28 $mWcm^{-2}$ specific power at 20 mVs^{-1} scan rate. The symmetric supercapacitor with two same PPy electrodes polymerized for 20 minutes had 0.056 Fcm^{-2} specific capacitance and 0.56 $mWcm^{-2}$ specific power at 20 mVs^{-1} scan rate.

Chapter 5 New Designs of Supercapacitors

Two approaches for creating 3D MEMS supercapacitors were designed and successfully developed based on LIGA-like and DRIE technologies. The electrochemical test results showed the specific capacitances of the two supercapacitors were 0.029 Fcm^{-2} and 0.056 Fcm^{-2}. These results are higher compare to the works presented in other literatures [33,35], which means the two approaches are suitable for creating high performance MEMS supercapacitors thanks to effective magnification of surface area. However, the two types of 3D MEMS supercapacitors cannot satisfy special applications, such as high temperature electronics. In the following text, some newly emerging designs of supercapacitors are discussed in order to satisfy different applications.

5.1 MEMS electrostatic supercapacitors for high temperature electronics

The traditional EDLC and EPC are based on liquid, ionic liquid [97] or solid state electrolyte, which is impossible to expose to extreme operation temperatures. But sometimes, energy storage device in high temperature is required. In another words, the problem is that the traditional supercapacitor would not be able to work properly under a temperature over the range it can physically afforded. Electrostatic supercapacitor (capacitor with very thin dielectric layer) is a good choice for this situation. The capacitance C of electrostatic supercapacitor is determined by Eq. 5.1. It is obvious that large dielectric constant ε_r, large surface area A and thin thickness of the dielectric layer d, are required to achieve high performance electrostatic supercapacitors.

$$C = \frac{\varepsilon_r \varepsilon_0 A}{d} \tag{5.1}$$

“Black silicon” nanograss structure produced by DRIE, nanoholes created by silicon anodic oxidation and combination of DRIE and anodic oxidation were used for the design of MEMS electrostatic supercapacitors for high temperature electronics.

5.1.1 “Black silicon” based electrostatic supercapacitor

The detailed fabrication process flow is shown in Fig. 5.1. This is the first time to employ the “black silicon” process to achieve a significantly large surface area for the supercapacitor. The supercapacitor is based on silicon substrate, highly-doped silicon with “black silicon” structure as one electrode, very thin dielectric (several nm, comparable to electric double layer of electrolyte) layer such as Al_2O_3 deposited by ALD, and a metal layer as the other electrode. The challenges include how to etch the highly-doped Si with enough effective surface area, and how to control the very thin dielectric layer with high electric constant and to avoid leakage current.

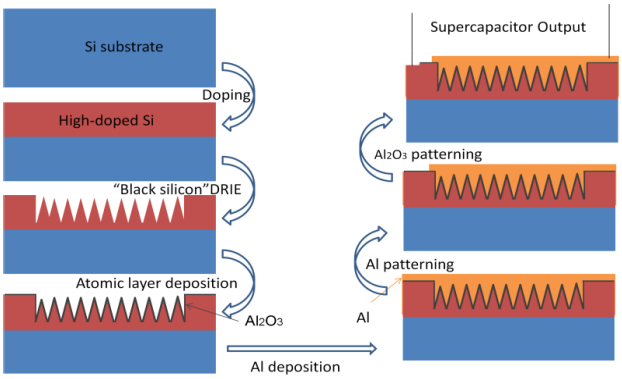

Fig. 5.1 “Black silicon” based electrostatic supercapacitor

5.1.2 Anodic oxidation based electrostatic supercapacitor

Fig. 5.2 shows the design of fabrication flow of anodic oxidation based electrostatic suercapacitor. Firstly, Si substrate will be anodic oxidized with high dense high-aspect-ratio nanoholes. Subsequently, ALD will be used to deposit very thin and conformal Al and Al_2O_3 layers, serving as the bottom electrode and the dielectric layer of the supercapacitor, respectively. Finally, another layer of Al will be deposited to function as the top electrode, the supercapacitor will be finished by two steps lithography and etching.

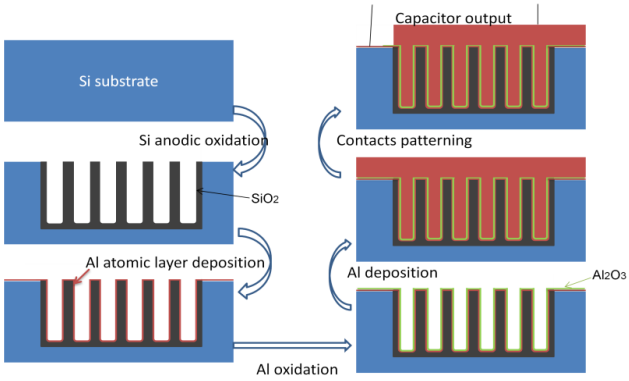

Fig.5.2 Anodic oxidation based electrostatic supercapacitor

5.1.3 DIRE and anodic oxidation based electrostatic supercapacitor

The MEMS supercapacitor design combining DRIE and anodic oxidation is shown in Fig. 5.3. The fabrication processes will be carried out to produce 3D microstructures and high dense nanoholes, which enable several thousand times magnification of the surface area in comparison to the original silicon wafer. Very thin conformal bottom electrode ALD and high dielectric constant material ALD enable high working temperature of the supercapacitor. In this supercapacitor, very thin conformal dielectric layer with high dielectric constant and high breakdown voltage is required. It is very promising for electrostatic supercapacitor in application of autonomous systems, especially in where the high operating temperature is required.

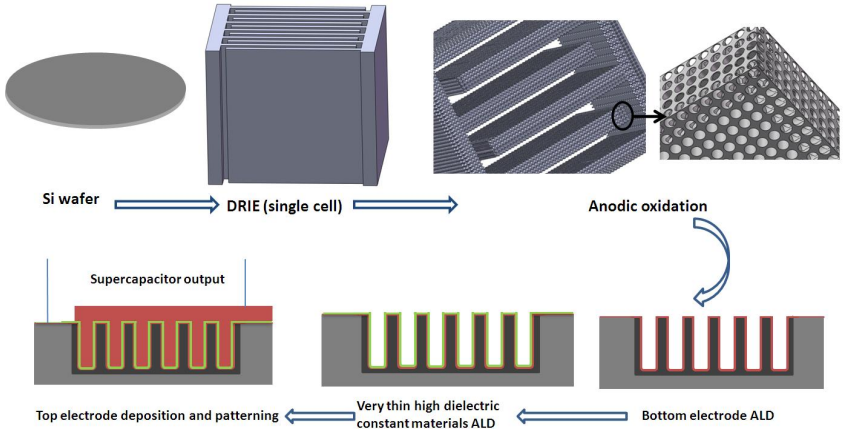

Fig. 5.3 DRIE and anodic oxidation based electrostatic supercapacitor.

5.2 MEMS supercapacitors for applications of high capacitance and power

5.2.1 "Black silicon" based double layer supercapacitor

As shown in Fig. 5.4, "black silicon" based double layer supercapacitor consists of two silicon wafers and two glass wafers. The two highly doped Si wafers will be micromachined with "black silicon" using specific DRIE process, and one glass wafer will be etched through the whole thickness. The three wafers then bond together to form the chamber for electrolyte filling-in. After several small holes are etched on the upper wafer and electrolyte is filled in, another glass wafer will be used to package the three Si/glass/Si structure.

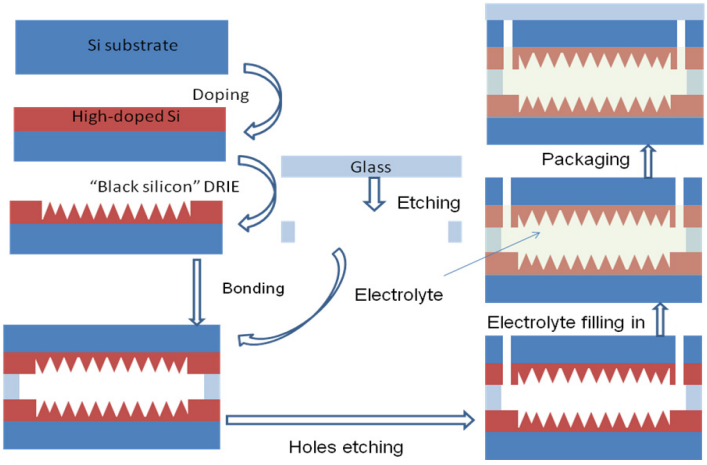

Fig.5.4. "Black silicon" based double layer supercapacitor

5.2.2 Polymer-carbon based double layer supercapacitor

The fabrication process flow is shown in Fig. 5.5. Firstly, on a glass wafer, a groove will be etched and SU-8 was filled in the groove. Secondly, the Tilted Multi-Exposure Lithography (TMEL) [98] or Multi Photon Laser Lithography (MPLL) [99] will be used to form nanoholes-in-nanocombs (Fig. 5.6a) or complicated nanostructures (Fig. 5.6b). Thirdly, pyrolysis will be performed to form 3D carbon structures. Finally, the electrolyte will be filled in and the device will be packaged.

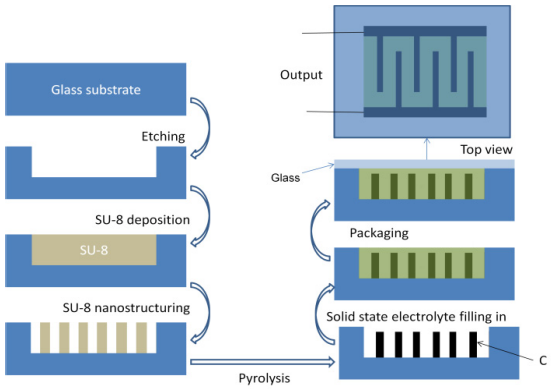

Fig . 5.5 Polymer-carbon based double layer supercapacitor

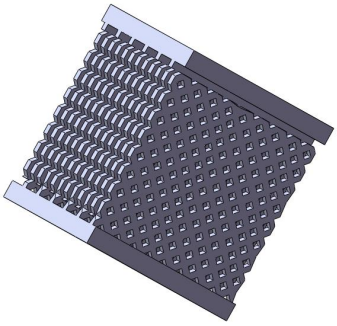

Fig. 5.6 Nanoholes-in-nanocomb structures.

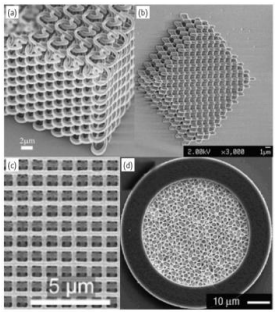

Fig. 5.7 SU-8 images by MPLL [99].

5.2.3 Ti anodic oxidation based electrochemical pseudo supercapacitor

Anodic oxidation for preparing TiO_2 nanotubes has been used for surface magnification of the electrodes of supercapacitors by Xie et al [36]. Based on the wafer level process, a MEMS supercapacitor is design as shown in Fig. 5.8. At first, thermal oxidation of silicon will be carried out to form the insulating layer. Secondly, the titanium layer will be sputtered and patterned with interdigitated structure. Then, anodic oxidation will be performed in HF solution to form highly ordered TiO_2 nanoholes. Finally, Ni/NiO electroactive layer will be conformal coated on the surface of Ti nanostructures by galvanostatic electrodeposition. In addition, DRIE can be used prior to Ti depostion to achieve a large surface area. Some experimental works on TiO_2 nanoholes anodic oxidation were done, which are presented in part 5.5.

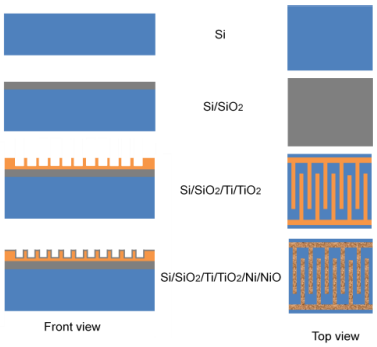

Fig. 5.8 Ti anodic oxidation based electrochemical pseudo supercapacitor

5.3 Supercapacitors for large scale applications

So far, no work has ever been done to create a large scale supercapacitor by using the wafer level process for applications such as electric vehicles. Combining carbon-MEMS with TMEL [98] is a promising approach to achieve highly ordered carbon nanofeatures. Fig. 5.9 presents the principle of TMEL, common UV exposure can result in nanofeatures with the size less than 400 nm. Nano Imprint Lithography (NIL) [100] can be introduced if even smaller nanofeatures are required.

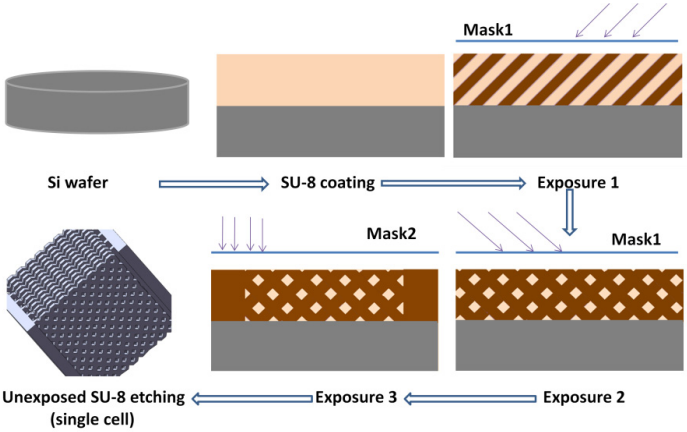

Fig.5.9 High dense micro- or nano- structure fabrication process flow by TMEL.

Fig. 5.10 is the fabrication flow of stacked wafer level polymer based double layer supercapacitor. The SU-8 nanostructure obtained from TMEL will be heated at about 1000 °C with N_2 protection for several hours. After activation of the split carbon layer in

strong alkaline solution, several layers of the highly ordered carbon nanostructures will be stacked and configured with proper electrolyte and high performance separator to form a double layer supercapacitor. This approach presents a cost-effective method to create the electrodes with highly ordered nanostructures for double layer supercapacitors, and the concepts should be attractive supercapacitors manufactures.

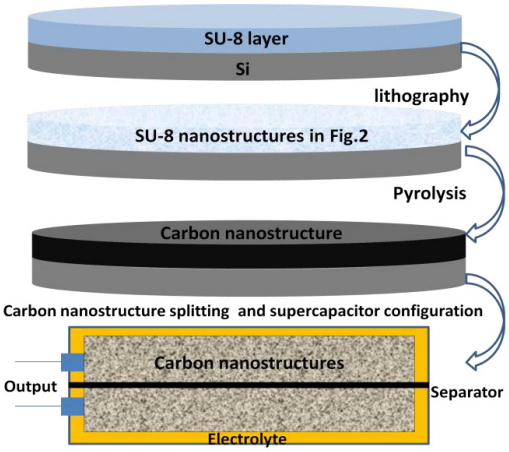

Fig.5.10 Stacked wafer level polymer based double layer supercapacitor.

5.4 Experimental work for TiO_2 nanoholes fabrication

5.4.1 Ti/SiO_2/Si thin film preparation

4 inch silicon wafer was used as the substrate which went through the standard processes to clean both organic and inorganic contaminations. The silicon wafer was cleaned in H_2SO_4/H_2O_2 solution, $NH_3/H_2O_2/H_2O$ solution and $HCl/H_2O_2/H_2O$ solution in sequence to remove grease, silicon dioxide and metallic impurity on the surface of silicon wafer, respectively. Hot de-ionized (DI) water was used to remove the residual cleaning solution after each cleaning step, and nitrogen gas and heat treatment were used to dry the wafer. Subsequently, the dry thermal oxidation/ wet thermal oxidation/dry thermal oxidation process was carried out to grow about 1.5 μm silicon oxide layer on the surface of silicon wafer as the insulation layer, the total oxidation time was about 10 hours. And then, about 400 nm titanium layer was deposited by RF sputtering on the surface of silicon

oxide. The RF sputtering was carried out in a chamber with wafer supporter rotation speed of 20 rpm at room temperature. The pressure inside the chamber is 0.76 Pa, the Ar gas flow speed was 70 sccm. The sputtering speed of about 5 nmmin^{-1} was obtained.

5.4.2 Titanium oxide anodic oxidation

The Ti/SiO_2/Si wafer was cut into small pieces with 1 cm *2 cm which were cleaned by acetone and DI water with the help of ultrasound. Then, anodic oxidation of titanium was carried out on 1 cm *1 cm area in a polytetrafluoroethene (PTFE) electrolytic bath containing HF aqueous solution with various concentrations. Hydrofluoric acid (48 wt % in water) was used as received. A platinum sheet was used as the cathode. Model 2602 dual-channel system source meter instrument from Keithley was used as the constant voltage source and current meter. Bias voltage and time dependences of the anodic oxidation of titanium were also investigated. The experimental setup is shown in Fig. 5.11.

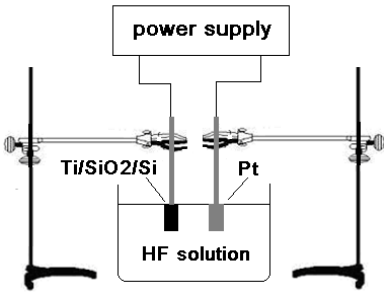

Fig. 5.11 Experimental setup for anodic oxidation.

5.4.3 Morphology testing

All achieved samples TiO_2/Ti/SiO_2/Si after anodic oxidation were characterized using a Philips XL30 scanning electron microscope (SEM). Energy dispersive spectrometer (EDS) was used to investigate the elements of the TiO_2/Ti/SiO_2/Si.

5.4.4 Results and discussions

5.4.4.1 Mechanism of titanium anodic oxidation

Mor et al. [101] suggested that Ti anodic oxidation occurred as a result of a competition between electrochemical oxide formation and chemical dissolution of oxide by fluoride ions. Firstly, a thin barrier metal oxide was formed on the metal surface as shown in Eq.

5.2,

$$Ti + 2H_2O \rightarrow TiO_2 + 4H^+ + 4e^- \quad (5.2)$$

The reaction could be enhanced by the application of an electric field which aided the ion transport of O^{2-} and Ti^{4+} through the growing oxide. However, the electric field across the film was reduced with the increasing thickness of oxide layer. Then, the chemical dissolution of TiO_2 dominated and reduced the thickness of oxide layer as shown in Eq. 5.3. Finally, the rate of titanium oxidization assisted by electric field equaled the rate of dissolution by fluoride, which resulted in the constant barrier layer thickness.

$$TiO_2 + 6F^- \rightarrow [TiF_6]^{2-} \quad (5.3)$$

5.4.4.2 Effect of polymerization conditions

0.5 wt% HF aqueous solution is the most commonly used electrolyte for foil titanium anodic oxidation in literatures [36]. It has been reported that a certain anodic oxidation potential is necessary to yield ordered titanium oxide nanotube arrays, and 10 V was suggested as the lowest required potential [102]. However, the thickness of titanium film in the experiments was about 400 nm, which was very easy to be etched off. So, weak anodic oxidation condition should be used for the $Ti/SiO_2/Si$ samples. HF aqueous solutions with various concentrations (0.5 wt%, 0.15 wt% and 0.05 wt%) and anodic oxidation voltages from 0.5 V to 30 V were used to investigate the effect of the thin film titanium anodic oxidation.

It was found that it was very difficult to achieve continuous TiO_2 nanotubes film at the whole etching area at voltage above 10 V or in the 0.5 wt% HF solution. Fig. 5.12 shows the SEM microphotographs and EDS spectrums of anodized samples at 20 V applied voltage in electrolyte containing 0.5 wt% HF for 8 min. It was found in Fig. 5.12a that there was almost no titanium element (0.04%) at the center of the anodic oxidation area after 8 minutes reaction, and therefore no holes could be found on the titanium etched-off SiO_2 surface (as shown in Fig. 5.12b). While around the anodic oxidation boundary area, the atomic ratio of titanium element was 33.26% (as shown in Fig. 5.12c), and some holes were found with an average diameter of about 150 nm, which could be observed in Fig. 5.12d.

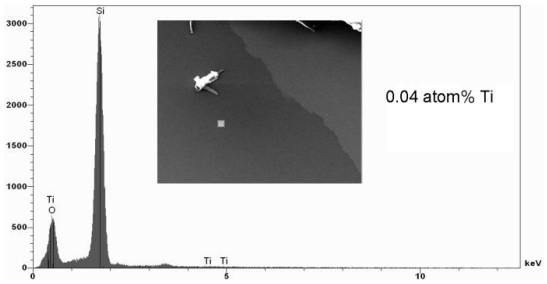

(a)

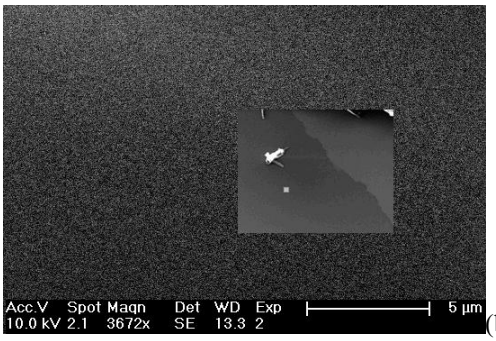

(b)

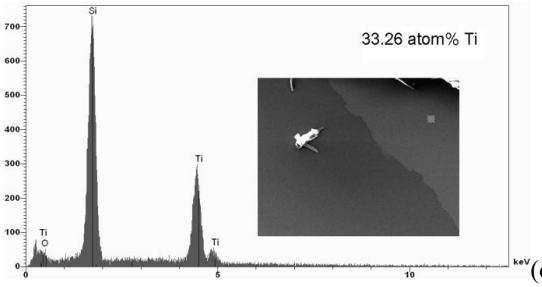

(c)

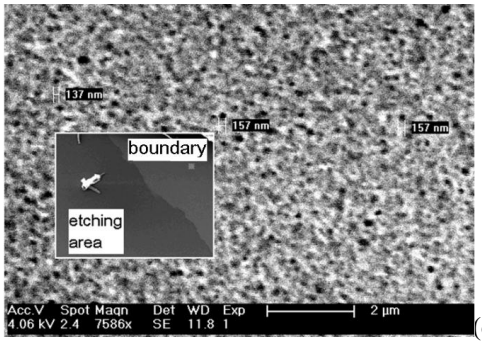

(d)

Fig. 5.12 Titanium anodic oxidation at 20 V in 0.5 wt% HF aqueous solution for 8 min, (a) EDS spectrum of center etching area, (b) SEM of center etching area, (c) EDS spectrum of boundary area, (d) SEM of titanium oxide nanotubes at boundary area.

Fig. 5.13 shows the current curve of the anodic oxidation obtained at 20 V in 0.5 wt% HF aqueous solution for 8 min. At the very beginning, the anodic current reached to 25 mA which resulted from the titanium fast dissolution in HF solution and produced ions of Ti^{4+}. The Ti^{4+} ions combined with O^{2-} to form a block layer of TiO_2. With the increasing thickness of block layer, the current dropped to about 0.92 mA, then kept a constant value for about 30 s, corresponding to an equilibrium state of titanium oxidation and titanium oxide dissolution. But afterwards the current suddenly dropped again to about 0.40 mA. It was suggested that the whole titanium/titanium oxide at the center anodic oxidation area was etched off, and SiO_2 layer was exposed in HF solution. Consequently, for the samples with 400 nm titanium layer, it may be very difficult to control the anodic oxidation time when "strong" conditions are applied.

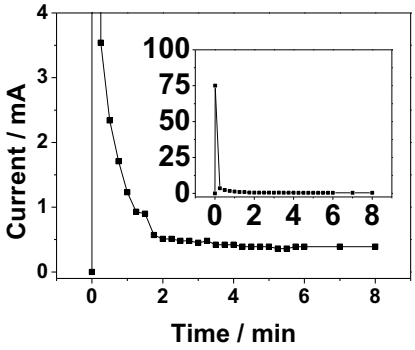

Fig. 5.13 Current curve of anodic oxidation at 20 V in 0.5 wt% HF aqueous solution for 8 min.

"Weaker" conditions were also applied to obtain good titanium nanotubes. It was found that controllable titanium nanotubes could be achieved at "ultra weak" anodic oxidation conditions of 0.5 V applied voltage in 0.05 wt% HF aqueous solution. Different durations of anodic oxidation were applied with "ultra weak" conditions. Fig. 5.14a and Fig. 5.14b present the SEM pictures of the prepared samples with anodic oxidation time of 8 min and 28 min. For 8 min anodic oxidation, there were no clear holes, but only rough nanostructures could be seen from Fig. 5.14a. While nanoholes with average diameter of 110 nm could be obtained in the sample anodic oxidized under "ultra weak" conditions for

by using 28 min. However, for a large energy density of supercapacitors, the density of nanoholes created so far is not large enough.

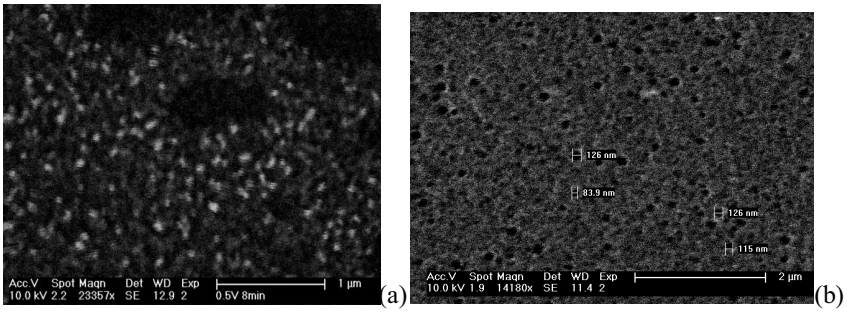

(a) (b)

Fig. 5.14 SEM of titanium oxide nanostructures obtained by "ultra weak" anodic oxidation of 0.5 V applied voltage in 0.05 wt% HF aqueous solution, (a) 8min (b) 28 min.

Further investigation on developing the effective anodic oxidation process for nano-thickness titanium film was carried out by changing the electrolyte. As an example, 0.05 wt% HF H_2O/Ethanol (50/50 vol%) solutions were used. Fig. 5.15a shows the anodic current curves at 0.5 V anodic voltages in different electrolytes with HF concentration of 0.05 wt%. It can be seen that the anodic current in aqueous electrolyte was about 3 times as that in H_2O/Ethanol electrolyte, which means that electrolyte formed an even weaker anodic oxidation condition than the defined "ultra weak" condition above. This is because the additional ethanol reduced the rates of ions diffusion. However, in such electrolyte of 0.05 wt% HF in H_2O/Ethanol (50/50 vol%), no nanostructure could be found at bias voltage of 0.5 V, even at bias voltage as high as up to 5 V. The anodic current curves at various voltages are shown in Fig. 5.15b.

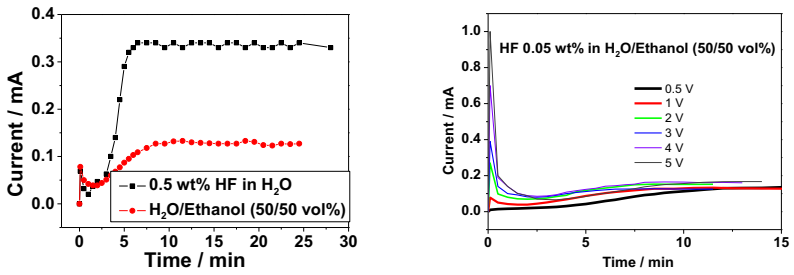

(a) (b)

Fig. 5.15 Current curves of titanium anodic oxidation with different conditions, (a) 0.5 V

applied voltage in 0.05 wt% HF aqueous and H_2O/Ethanol (50/50 vol%) solutions, (b) at various voltages from 0.5 V to 5 V in 0.05 wt% HF H_2O/Ethanol (50/50 vol%) solution.

5.4.4.3 Two step titanium anodic oxidation

As discussed above, the "ultra weak" condition of 0.5 V and 0.05 wt% HF aqueous solution is suitable for anodic oxidation of thin titanium film. However, it was found that, by analyzing the anodic current curves shown in Fig. 5.15a, no thick block layer growing process could be observed in the strong condition of anodic oxidation (such as in Fig. 5.13). The thick block layer would reduce the dissolution rate, which could effectively keep the thickness of the thin titanium layer. Therefore, two-step method (first step to form block layer, second step to form nanotubes) was used to anodize titanium. Fig. 5.16a shows the current curve of titanium anodic oxidation in 0.05 wt% HF aqueous solutions at applied voltage of 10 V for 1min and then 0.5 V for 10 min. At the end of anodic oxidation, the anodic current was about 0.08 mA and did not reach a constant value, i.e. an equilibrium state of oxidation and dissolution. Fig. 5.16b presents the corresponding SEM photograph, in which, sparse nanoholes with average diameter of 110 nm could be found.

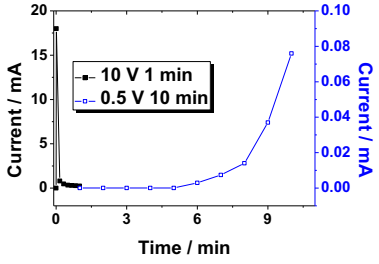

(a)

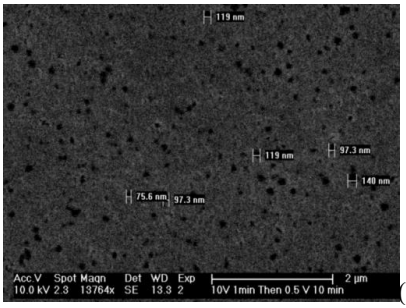

(b)

Fig. 5.16 Titanium anodic oxidation in 0.05 wt% HF aqueous solution at applied voltage of 10 V for 1min and then 0.5 V for 10 min, (a) current curve, (b) SEM view of top surface.

To reach equilibrium state of TiO_2 oxidation and dissolution, the time of the first anodic oxidation step was reduced to 20 s and the time of second step was increased to 25 min (2 min constant current value of about 0.33 mA as shown in Fig. 5.17a). The result is given in Fig. 5.17b, which is the SEM picture showing the top surface of the sample. It could be seen that the density of nanotubes was very high and the diameter of the nanotubes ranged from about 90 to270 nm with an average value of 150 nm. So structured

surface may be very suitable for the high energy density MEMS supercapacitor designed in Fig. 5.8. From the SEM observation of the cross-section, as shown in Fig. 5.17c, the thickness of TiO_2/Ti layer was still about 400 nm. And there was no slit at the interface of Ti layer and SiO_2 layer, which means the adhesive force at the interface was strong enough to avoid etching of "ultra week" HF solution. Fig. 5.17d presents the EDS spectrum of TiO_2/Ti layer, in which the atomic ratio of titanium element was 48.91%. By integrating the current curve in Fig. 8a, the titanium lose could be calculated as 8.6×10^{-7} mol, while the total titanium can be calculated as 3.8×10^{-6} mol.

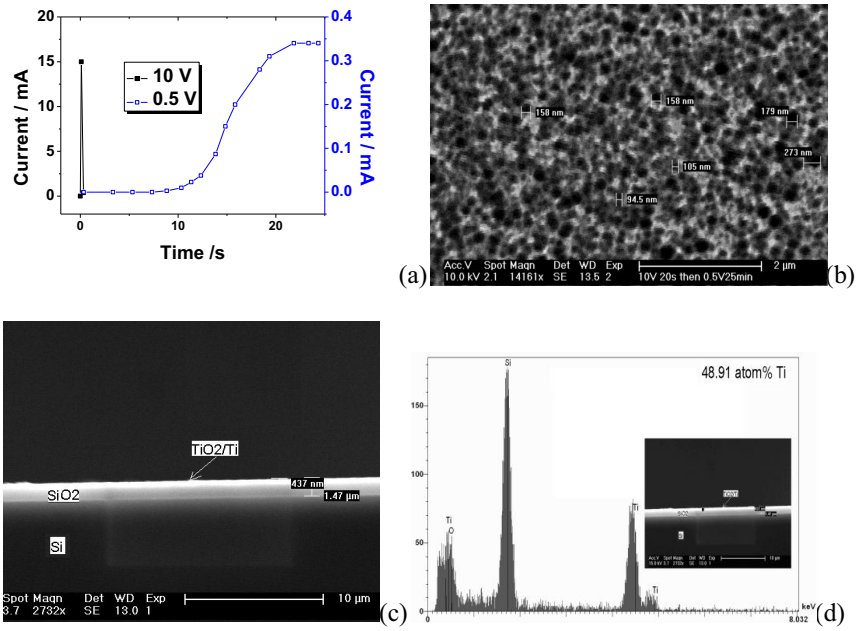

Fig. 5.17 Titanium anodic oxidation in 0.05 wt% HF aqueous solutions at applied voltage of 10 V for 20 s and then 0.5 V for 25 min, (a) current curve, (b) SEM view of top surface, (c) SEM of cross-section, (d) EDS of Ti/TiO_2 cross-section.

5.5 Chapter conclusions

In this chapter, several new types of supercapacitors for different applications were designed. "Black silicon" based electrostatic supercapacitor, anodic oxidation based electrostatic supercapacitor and DRIE and anodic oxidation based electrostatic supercapacitor were designed for the application of high temperature electronics. "Black

silicon" based double layer supercapacitor, polymer-carbon based double layer supercapacitor and titanium oxidation based electrochemical pseudo supercapacitor were designed for applications which high capacitance and power are required. A supercapacitor based on stacked wafer level microfabricated SU-8 phtoresist was designed for the large scale applications such as electric vehicles. Finally, some experimental work on titanium oxide anodic oxidation was done. It was the first time that "ultra weak" anodic oxidation was used to obtain TiO_2 nanotubes based on SiO_2/Si substrate. The two-step anodic oxidation method was developed to achieve enhanced results. It was found that high density of TiO_2 nanotubes with diameters ranged from about 90 to270 nm and with an average of 150 nm could be obtained in the 0.05 wt% HF aqueous solutions at applied voltage of 10 V for 20 s and then 0.5 V for 25 min. The nanostructured surface fabricated by the two-step method is promising for manufacturing the MEMS supercapacitors with high performances.

Chapter 6 Conclusions and outlook

6.1 Conclusions

In the current studies, two types of 3D MEMS supercapacitors were designed and successfully fabricated based on LIGA-like and DRIE technologies. The fabrication processes for creating the two types of 3D MEMS supercapacitors were successfully developed. By high aspect ratio LIGA-like and DRIE technologies, 3D microstructures with a much larger effective surface area were achieved. Ni current collectors were fabricated by the electroforming and the electroless plating, Ti current collectors were fabricated by the two-step RF sputtering. The electrochemical polymerization of PPy films on 3D structures as the electrodes for the supercapacitors were investigated and optimized. Electrochemical characterizations were used to characterize the properties of the two types of 3D MEMS supercapacitors.

The LIGA-like based 3D MEMS supercapacitor was designed with an interdigital structure which increased the surface area by about 20 times compared with the planar structure for the same footprint. It was successfully fabricated by SU-8 lithography, nickel electroforming, PPy polymerization and solid sate electrolyte coating. CV tests showed that the single electrode has 0.058 Fcm^{-2} specific capacitance and 0.58 $mWcm^{-2}$ specific power at 20mVs^{-1} CV scan rate. The EIS tests implied that the supercapacitor can be used in applications of broad frequency range up to 300Hz with good stability. GCD gave that the specific capacitance and the specific power of the 3D MEMS supercapacitor were 0.029 Fcm^{-2} and 2.2 $mWcm^{-2}$, respectively, at a relative large discharge rate of 5 $mAcm^{-2}$.

DRIE technology had also been used for fabricating another type of 3D MEMS supercapacitor. The fabrication processes contained thermal oxidation, RF sputtering, wet etching, DRIE, electroless plating and PPy polymerization. By optimizing the processes, it was found that the PPy electrode prepared in the TOSNa aqueous solution exhibited a very good capacitance properties in NaCl electrolyte. The single PPy electrode of the 3D

MEMS supercapacitor provided 0.128 Fcm^{-2} specific capacitance and 1.28 $mWcm^{-2}$ specific power at 20 mVs^{-1} scan rate. While the symmetric 3D MEMS supercapacitor presented 0.056 Fcm^{-2} specific capacitance and 0.56 $mWcm^{-2}$ specific power at 20 mVs^{-1} scan rate.

By comparing the two types of 3D MEMS supercapacitors, it can be seen that the DRIE based 3D MEMS supercapacitor is superior by providing higher specific capacitance and specific power. This is because solid state electrolyte used in fabricating the LIGA-like based 3D MEMS supercapacitor limited the ions diffusion. However, note worthily, the advantage of the LIGA-like based 3D MEMS supercapacitor is its safety due to the all-solid-state structure. Both the two types of 3D MEMS supercapacitors are provide more specific capacitance than earlier works reported in other literatures, such as PPy planar supercapacitor [33] 2 $mFcm^{-2}$, carbon nanotube forests supercapacitor [35] 428 μFcm^{-2}, electrostatic supercapacitor [38] 100 μFcm^{-2}.

Part of the work related to the two types of 3D MEMS supercapacitors have been published in four journal papers, which were cited more than 10 times [103,104,105,106,107,108,109,110,111,112,113,114].

In addition, several new types of supercapacitors were designed for different purposes. The concepts of “Black silicon”, anodic oxidation, DRIE, polymer-carbon, were employed in these designs for enhanced performances of supercapacitors.

Finally, some experimental work on titanium oxide anodic oxidation was carried out, which is integratable in MEMS supercapacitors. It was the first time that “ultra weak” anodic oxidation has been used to obtain TiO_2 nanotubes based on SiO_2/Si substrate. Dense TiO_2 nanotubes with diameters ranged from about 90 to270 nm were obtained in 0.05 wt% HF aqueous solutions by the two-step anodic oxidation method.

6.2 Outlook

In order to further improve the properties of the 3D MEMS supercapacitors, there are still some issues worth exploring.

Firstly, for the 3D MEMS supercapacitors, the effect of different sizes and structures of the electrodes should be investigated.

Secondly, other conducting polymers such as PAN, PEDOT or composites could be alternative to PPy as the electrodes materials for supercapacitors with improved performances.

Thirdly, solid state electrolytes and appropriate packaging methods should be developed to complete the supercapacitor systems for the DRIE based MEMS supercapacitor.

Fourthly, the newly designed supercapacitors need to be fabricated and evaluated.

Finally, a real example of the integration of a 3D MEMS supercapacitor into an autonomous device could be a good demonstrator.

References

1 http://www.mpoweruk.com/performance.htm.

2 R. Miller, A. F. Burke, The Electrochemical Society interface, spring 2008.

3 http://www.azonano.com/news.asp?newsID=12002.

4 T. Sakakibara et al, Multi-source power supply system using micro-photovoltaic devices combined with microwave antenna, Sensrs and Actuators A 95 (2002) 208-211.

5 http://www.edn.com/article/CA6399099.html?industryid=2816.

6 E. Cantatore, M. Ouwerkerk, Energy scavenging and power management in networks of autonomous microsensors, Microelectronics Journal 37(2006) 1584-1590.

7 Ayyaz M. Paracha, et al, A bulk silicon-based vibration-to-electric energy converter using an In-Plana Overlap Plate (IPOP) Mechanism, The sixth international workshop on micro and nanotechnology for power generation and energy converson applications, Nov. 29 – Dec. 1, 2006, Berkeley, U.S.A

8 http://www.howelljones.ca/tech/energyscavengefull.pdf.

9 http://www.cap-xx.com/news/photogallery.htm.

10 R. Kotz, M. Carlen, Electrochimica Acta 45 (2000) 2483-2498.

11 http://www.maxwell.com/ultracapacitors/products/index.asp.

12 http://www.nesscap.com/products_edlc.htm.

13 Mcdowall J. Lithium battery technology—Saft. Winter StatBatt Technical Sessions. StatBatt Techanical Sessions. http://www.ewh.iee.org/cmte/PES-SBC, 2004.

14 Ryan Wartena, Aimee E. Curtright, et al, Li-ion microbatteries generated by a laser direct-write method, Journal of Power Sources 126 (2004) 193–202.

15 J.B. Bates, N.J. Dudney*, B. Neudecker, A. Ueda, C.D. EvansC N Polo da Fonseca, J Davalos, M Kleinke et al. J. Power Sources, 1999,81-82: 575~580.

16 K. L. Lee, J. Y. Jung et al. , J. Power Sources, 2004, 130: 241~246.

17 P ing Liu, Ji-guang Zhang, et al. Lithium-Manganese-Oxide thin-film cathodes prepared by Plasma-Enhanced Chemical Vapor Deposition. J Electrochem Soc, 1999, 146: 2001～2005.

18 Youn-Su Kim, Hyo-Jin Ahn, et al., Electrochemical and structural properties of MoO_3–V_2O_5 nanocomposite thin film electrodes for lithium rechargeable batteries, Solid State Ionics 177 (2006) 1323–1326.

19 V. Yufit, M. Nathan, et al., Thin-film lithium and lithium-ion batteries with

electrochemically deposited molybdenum oxysulfide cathodes, Journal of Power Sources 122 (2003) 169–173.

20 S.R. Das, W.W. Jones, IEEE Spectrum 20 (2004 (Oct.)).

21 J.W. Long, B. Dunn, D.R. Rolison, H.S. White, Chem. Rev. 104 (2004) 4463.

22 A. Singh, J. Jarayan, M. Madou, S. Akhbar, J. Electrochem. Soc. 149 (2002) E78.

23 D. Golodnitsky, V. Yufit, M. Nathan, I. Shechtman, T. Ripenbein, E. Strauss, S. Menkin, and E. Peled, "Advanced materials for three-dimensional (3-D) thin-film microbatteries," J. Power Sources, 2005.

24 D. Golodnitsky , V. Yufit, et al., Advanced materials for the 3D microbattery, Journal of Power Sources 153 (2006) 281–287.

25 Menachem Nathan, Diana Golodnitsky, et al., Three-Dimensional Thin-Film Li-Ion Microbatteries for Autonomous MEMS, JOURNAL OF MICROELECTROMECHANICAL SYSTEMS, VOL. 14, NO. 5, OCTOBER 2005 879~885.

26 Liang Cheng, Huiqiao Li, Yongyao Xia, A hybrid nonaqueous electrochemical supercapacitor using nano-sized rion oxyhydroxide and activated carbon, J solid State Electrochem 10 (2006) 405-410.

27 Chunsheng Du and Ning Pan, High power density supercapacitor electrodes of carbon nanotube films by electrophoretic deposition, Nanotechnology 17 (2006) 5314–5318.

28 Elzbieta Frackowiak, Franc¸ois Be´guin ,Electrochemical storage of energy in carbon nanotubes and nanostructured carbons, Carbon 40 (2002) 1775–1787.

29 Dmitri A. Brevnov and Tim S. Olson, Double-layer capacitors composed of interconnected silver particles and with a high-frequency response, Electrochimica Acta 51 (2006) 1172–1177.

30 Han-Ki Kim, Sun-Hee Choi, et al., Characteristics of RuO_2–SnO_2 nanocrystalline-embedded amorphous electrode for thin film microsupercapacitors, Thin Solid Films 475 (2005) 54– 57.

31 Jong-Huy Kim, Ashok K. Sharma, Yong-Sung Lee, Synthesis of polypyrrole and carbon nano-fiber composite for the electrode of electrochemical capacitors, Materials Letters 60 (2006) 1697–1701.

32 E. Frackowiak, V. Khomenko, K. Jurewicz, et al., Supercapacitors based on conducting polymers/nanotubes composites, Journal of Power Sources 153 (2006) 413–418, Short

communication.

33 Joo-Hwan Sung, Se-Joon Kim, Kun-Hong Lee, Fabrication of all-solid-state electrochemical microcapacitors, Journal of Power Sources 133 (2004) 312–319.

34 Joo-Hwan Sung, Se-Joon Kim, Flexible micro-supercapacitors, Short communication , Journal of Power Sources 162 (2006) 1467–1470.

35 Y. Q. Jiang, Q. Zhou, L. Lin, Micro Electro Mechanical Systems, 2009. MEMS 2009. IEEE 22nd International Conference on, 25-29 Jan. 2009, Sorrento, Italy.

36 Y. Xie, C. Huang, L. Zhou, Y. Liu, H. Huang, Composites Science and Technology 69 (2009) 2108-2114

37 Y. L. Xu, J. Wang, W. Sun, S. H. Wang, Journal of Power Sources, 159 (2006) 370-373.

38 P. Banerjee, I. Perez, L. H. Lecordire, S. B. Lee, G. W. Rubloff, Nature nanotechnology, letters, DOI:10.1038/nnano.2009.37.

39 S. M. George, Chem. Rev. 110 (2010) 111-131.

40 Forman, M. A. (December 2006). "Low-loss LIGA-fabricated coplanar waveguide and filter". Apmc 2006 12: 905–1907.

41 H. S. Min, B. Y. Park, L. Taherabadi , C. Wang, Journal of Power Sources, 178 (2008) 795–800.

42 C. Wang, L. Taherabadi, G. Jia, M. Madou, Y. Yeh, and B. Dunn, Electrochemical and solid-State Letters, 7 (11) A435-A438 (2004).

43 F. Ayazi et al., in Proc. Solid-State Sens. Actuator Workshop, Hilton Head, SC, June 4-8, 2000, pp. 289-292.

44 http://en.wikipedia.org/wiki/Electroforming.

45 http://corrosion-doctors.org/MetalCoatings/Electroless.htm.

46 http://www.uccs.edu/~tchriste/courses/PHYS549/549lectures/sputtertech.html.

47 D. Schmeiber, A. Bartl, L. Dunsch, h. Naarmann, W. Gopel, Synth. Met. 93 (1998) 43.

48 G. Appel, O. Bohme, R. Mikalo, D. Schmeiber, Chemical Physics Letters 313 (1999) 411-415.

49 F．Beck， M．Oberst，R．Jansen, Electrochimica. Acta. 35 (1990) 1841.

50 P．Claude，Andrieux，P．Audebert，P．Hapiot， Journal of Physical Chemistry，95 (1991) 10158.

51 J. Wang, y. Xu, X. Chen, X. Du and X. Li, Acta Physico-chimica Sinica, 23 (2007) 299-304.

52 J. H. Sung, S. J. Kim, K. H. Lee, Journal of Power Sources 133 (2004) 312–319.

53 J. H. Sung, S. J. Kim, K, Short communication , Journal of Power Sources 162 (2006) 1467–1470

54 http://en.wikipedia.org/wiki/Cyclic_voltammetry.

55 http://www.novocontrol.de/html/intro_eis.htm.

56 Chen Ye, Zhang Mi Kin, and Shi Zhao Hui, J. Electrochem. Soc., 152 (2005) 1272-1278.

57 User's guide of Solartron 1260.

58 C. Du and N. Pan, Nanotechnology 17 (2006) 5314-5318.

59 C. N. Cao, J. Q. Zhang, Introduction to electrochemical impedance specturescopy, Beijing:Science Press, 2004.

60 G. T. Gomez, E. M. T. Rosales, and P. G. Romero, Chem. Mater. 13 (2001) 3693-3697.

61 Wei Sun and Xuyuan Chen, "Fabrication and tests of a novel three dimensional micro supercapacitor", Microelectronic engineering, Volume 86, Issues 4-6, April-June 2009, Pages 1307-1310, the 34th International Conference on Micro- and Nano-Engineering (MNE), 15 -18 September 2008, Athens.

62 http://mems.gatech.edu/msmawebsite/members/processes/processes_files/SU8/SU-8.htm.

63 http://www.microchem.com/products/pdf/SU-82000DataSheet2100and2150Ver5.pdf.

64 http://en.supermask.com/.

65 http://en.wikipedia.org/wiki/Electroforming.

66 http://www.pfonline.com/articles/pfd0015.html.

67 L.Mirkova, G. Maurin, M. Monev and C. Tsvetkova, Journal of Applied Electrocheistry, 33 (2003), 93-100.

68 http://www.nmfrc.org/subs/history/sep1954b.cfm.

69 http://www.microchem.com/resources/SU-8_Removal_with_RIE.pdf.

70 P. M. Dentinger, W.M. Clift and S. H. Goods, Microelectronic engineering , 61-62 (2002) 993-1000.

71 http://memscyclopedia.org/su8.html.

72 S. Suematsu, Y. Oura, H. Tsujimoto, H. Kanno and K. Naoi, Electrochimca Acta 45 (2000) 3813-3821.

73 S. H. Song, D. S. Han, H. J. Lee, H. S. Cho, S. M. Chang, J. M. Kim and H. Muramastu, Synthetic Metals, 117 (2001) 137-139.

74 M. D. Ingram, H. Staesche and K. S. Ryder, Journal of Power Sources 129 (2004)

107-112.

75 C. C. Hu, X. X. Lin, Journal of the Electrchemical Society, 149 (2002) A1049-A1057.

76 C. Arbizzani, M. Mastragostino, and L. Meneghello, Electrochinica Acta, 40 (1995) 2223.

77 S. Panero, A. Clemente and E. Spila, Solid State Inomics 86-88 (1996) 1285.

78 J. Bates, N.J. Dudney, G.R. Gruzalski, R.A. Zuhr, A. Choudhury, C.F. Luck and J.D. Robertson. Solid State Ionics 53 (1992) 647.

79 E.J. Jeon, Y.S. Yoon, S.C. Nam, W.I. Cho and Y.W. Shin. J. Korean Electrochem. Soc. 3 (2000), p. 115.

80 Y. S. Yoon, W. L. Cho, J. H. Lim and D. J. Choi, Journal of Power Sources, 101-1 (2001) 126-129.

81 K. W. Park, H. J. Ahn and Y. E. Sung, Journal of Power Sources, 109-2 (2002) 500-506.

82 Y. G. Wang and X. G. Zhang, Solid State Ionics, 166 (2004) 61-67.

83 C. Weidlich, K. M. Mangold, K. Juttner, Electrochimica Acta 50 (2005) 1547-1552.

84 D. A. Brevnoc, T. S. Olson, Electrochimica Acta 51 (2006), 1172-1177.

85 Y. Xu, J. Wang, W. Sun, S. Wang, Journal of Power Sources 159 (2006) 370-373.

86 Wei Sun, Haisheng San, yingxian Duo and Xuyuan Chen, "Preparation and Characterization of Micro Polypyrrole Electrodes for Supercapacitor", Advanced Materials Research, 60-61(2009) 375-379, 1st International Conference of the Chinese Society of Micro/Nano Technology, 20 - 22 November 2008, Beijing

87 Wei Sun and Xuyuan Chen, "Preparation and characterization of polypyrrole films for three-dimensional MEMS supercapacitor", Journal of Power Sources, 193 (2009) 924–929.

88 Wei Sun and Xuyuan Chen, "Symmetric Redox Supercapacitor Based on microfabrication with Three Dimensional Polypyrrole Electrodes", Journal of Power Sources, 195 (2010) 7120-7125

89 http://en.wikipedia.org/wiki/Deep_reactive-ion_etching.

90 http://en.wikipedia.org/wiki/Plating.

91 K. G. Keong, W. Sha and S. Malinov, Journal of Alloys and Compounds 334 (2002) 192-199.

92 http://www.eriehardchrome.com/electroless-nickel-plating.html#highphosphorous.

93 J. Ouyang and Y. Li, Polymer, 38 (1997) 1971-1976.

94 F. Lufrano and P. Staiti, Electrochimica Acta, 49 (2004) 2683-2689.

95 Y. Fintschenko, A. van den Berg, Journal of Chromatography A 819 (1998) 3-12.

96 Y. Y. T, R. C. Zhou, H. X. Zhang, G. Z. Lu, Z. H. Li, Journal of Micromechanics and Microengineering, 16 (2006) 2570-257.

97 http://en.wikipedia.org/wiki/Ionic_liquid.

98 H. Sato, D. Yagyu, S. Ito and S. Shoji, Sensors and Actuators A: Physical, 128 (2006) 183-190.

99 K. K. Seet et al., Applied Physics Letter 88 (2006), 221101.

100 S. Y. Chou et al., Applied Physics Letters, 67 (1995) 3114-3116.

101 G. K. Mor, O. K. Varghese, M. Paulose, N. Mukherjee, C. A. Grimes, Journal of Materials Research, 18 (2003) 2588-2593.

102 D. Gong, C. A. grimes, O. K. Varghese, W. Hu, R. S. Singh, Z. Chen, E. C. Dickey, Journal of Materials Research, 16 (2001) 3331-3334.

103 Byon, H.R., Lee, S.W., Chen, S., Hammond, P.T., Shao-Horn, Y., Thin films of carbon nanotubes and chemically reduced graphenes for electrochemical micro-capacitors, (2011) Carbon 49 (2), pp. 457-467.

104 Liu, C.-C., Tsai, D.-S., Susanti, D., Yeh, W.-C., Huang, Y.-S., Liu, F.-J., Planar ultracapacitors of miniature interdigital electrode loaded with hydrous RuO2 and RuO2 nanorods, (2010) Electrochimica Acta 55 (20), pp. 5768-5774.

105 Chmiola, J., Celine Largeot, P.-L.T., Simon, P., Gogotsi, Y., Monolithic carbide-derived carbon films for micro-supercapacitors, (2010) Science 328 (5977), pp. 480-483.

106 Pech, D., Brunet, M., Taberna, P.-L., Simon, P., Fabre, N., Mesnilgrente, F., Conédéra, V., Durou, H., Elaboration of a microstructured inkjet-printed carbon electrochemical capacitor,(2010) Journal of Power Sources 195 (4), pp. 1266-1269.

107 Li, L.-M., Liu, E.-H., Li, J., Yang, Y.-J., Shen, H.-J., Huang, Z.-Z., Xiang, X.-X., Polyaniline-based carbon for a supercapacitor electrode, (2010) Wuli Huaxue Xuebao/ Acta Physico - Chimica Sinica 26 (6), pp. 1521-1526.

108 Zhang, Y., Wang, Y., Xu, S., Wang, J., Wang, Z., Wang, S., Polypyrrole nanowire modified graphite (PPy/G) electrode used in capacitive deionization,(2010) Synthetic Metals 160 (13-14), pp. 1392-1396.

109 Agboola, B.O., Ozoemena, K.I., Synergistic enhancement of supercapacitance upon integration of nickel (II) octa [(3,5-biscarboxylate)-phenoxy] phthalocyanine with SWCNT-phenylamine,(2010) Journal of Power Sources 195 (12), pp. 3841-3848.

110 Chen, L., Sun, L.-J., Luan, F., Liang, Y., Li, Y., Liu, X.-X., Synthesis and pseudocapacitive studies of composite films of polyaniline and manganese oxide nanoparticles, (2010) Journal of Power Sources 195 (11), pp. 3742-3747.

111 Chidembo, A.T., Ozoemena, K.I., Agboola, B.O., Gupta, V., Wildgoose, G.G., Compton, R.G. Nickel(ii) tetra-aminophthalocyanine modified MWCNTs as potential nanocomposite materials for the development of supercapacitors,(2010) Energy and Environmental Science 3 (2), pp. 228-236

112 Qin,C,-L., Lu, X., Yin, G.-P., Bai, X. –D., Jin, Z. activated nitrogen-enriched carbon/carbon aerogel nanocomposites for supercapacitors applications, 2009 Transactions of Nonferrous Matals Society of China, 19 (SUPPL.3), pp. s728-s742.

113 Beidaghi, M., Chen, W., Wang, C., Electrochemically activated carbon micro-electrode arrays for electrochemical micro-capacitors, 2011, Journal of power sources 196 (4), pp. 2403-2409.

114 Liangliang, T., Chunyang, J. Conducting polymers as electrode materials for supercapacitors, 2010, Progress in Chemistry 22(8), pp. 1610-1618.

Acknowledgement

At first, I would like to thank the financial support of KD project.

Many thanks give to my supervisors, Prof. Xuyuan Chen and Prof. Per Øhlckers for their great support and guidance during my studies. Prof. Xuyuan Chen walked me through all the stages of the writing of this thesis. Without his consistent and illuminating instruction, this thesis could not have reached its present form.

I would like to thank the teachers, master and PhD students, and also engineers in Pen Tung Sah MEMS research center at Xiamen University, China, for helping me do experimental work of MEMS fabrication. I also thank the State Key laboratory for Physical chemistry of solid surface at Xiamen university, China, for allowing me to use their instruments to do electrochemical testing.

I would like to thank Prof. Kaiying Wang, engineers Zekiya Ramic and Ragnar Johansen for helping me to do chemical experiments in the clean room at Vestfold University College. I also thank the colleagues at Vestfold University College who gave me their help and brought me a lot of fun.

Last my thanks would go to my beloved parents, my brother and my girlfriend for their loving considerations, great confidence in me and strong supports all through these years. Otherwise, the thesis would not be completed.

Appendixes

The appendixes contain four publications related to this thesis.

Appendix 1"Fabrication and tests of a novel three dimensional micro supercapacitor" presented the design, fabrication and tests of the 3D MEMS supercapacitor based on LIGA-like technology. It is the main part of chapter 3.

Appendix 2 “Preparation and Characterization of Micro Polypyrrole Electrodes for Supercapacitor” presented the comparison of 3D and planar $Si/SiO_2/Ni/PPy$ electrodes. The result is that DRIE is an effective approach to enlarge the surface area for the deposition of Ni current collector and PPy film. The microfabricated 3D electrode is promising in MEMS supercapcitors.

Appendix 3 “Preparation and characterization of polypyrrole films for three-dimensional MEMS supercapacitor” presented that the properties of the 3D electrode based on DRIE technology depended on the PPy polymerization conditions and the electrolyte. PPy doping with ClO_4^- performed better capacitance properties than PPy doping with Cl^- in NaCl electrolyte.

Appendix 4 “Symmetric Redox Supercapacitor Based on microfabrication with Three Dimensional Polypyrrole Electrodes” presented the design, fabrication and characterization of the 3D MEMS supercapcitors based on DRIE technology. The PPy_{TOS}-in-NaCl system performed very good supercapcitors properties, with 0.056 Fcm^{-2} specific capacitance and 0.56 $mWcm^{-2}$ specific power at 20 mVs^{-1} scan rate.

The chapter 4 of this thesis “3D MEMS supercapcitors based on DRIE technology” was mainly made up of appendix 2, appendix3, and appendix4.

I

II

III

IV